Doctoral Dissertation

Spatial Chemical Potential Engineering for Quantum Dot Formation in Graphene Nanoribbon via Controllable Doping

Zhongwang Wang

Supervisor: Prof. Hiroshi Mizuta

Graduate School of Advanced Science and Technology
Japan Advanced Institute of Science and Technology
Materials Science
March 2020

Abstract

Graphene nanoribbons (GNRs) with widths of tens-of-nanometer have been demonstrated as an effective way to realize the transport gap opening by quantum confinement. However, it is known that carriers in graphene are inevitably subjected to the disordered potential caused by the localized charge states originated from the surrounding environments, e.g. the substrate defects, surface adsorptions, organic residues from fabrication, and the edge roughness. The origin and properties of such localized charge states have been exhaustively investigated. Charge puddles with the size of ~ 10 nm have been directly measured in graphene placed on SiO_2 substrate using scanning tunneling microscopy. Quantum dots-like transport features have been observed in the monolayer GNRs in their tranport measurment, as the carriers can tunnel through the isolated charge puddles. Moreover, it has been demonstrated that geometries of the charge puddles and the correlated transport properties are able to be tuned electrically by applying external electric filed. At some certain conditions, single quantum dot (QD)-like transport behaviour can be observed as long as the disordered transport gap satisfy the conditions, *e. g.*, double tunnel barriers assembling on the sides of a quantized conductive charge island. So far, controllable QD-like transport in GNRs had only been realized by electrostatic confinement technique *i. e.*, fabricating a local gate on the designed position. Other doping approaches have been not demonstrated.

In our work, we considered a new strategy to realize single QD-like band landscape via controllable doping. We developed two approach to generate doping from hydrogen silsesquioxane (HSQ capping layer. First is current annealing, which could be used to tune the universal doping level in graphene. Second is controllable e-beam exposure, which can be used to realize doping control with nano-meter precise spatial control. Finally, we successfully achieved single QD-like transport in GNR at low temperature.

Keywords: graphene nanoribbon, doping, single quantum dot-like behaviour

Contents

List of Figures

Chapter 1

Introduction

In solid state physics, low dimensional electron transport is important in terms of both fundamental physics investigation and electronic applications. Before the discovery of graphene, electron transport in real three-dimensional and one-dimensional materials, *e.g.,* silicon and carbon nanotube, had been studied theoretically and experimentally. In comparison, study of two-dimensional electrons is mainly achieved by using electrostatic confinement technique as pure two dimensional is presumed not to exist due to the thermal instability of its crystalline lattice. Under such circumstances the discovery of graphene by Sir Andre Geim and Sir Kostya Novoselov in Manchester University is extremely important because graphene is the first two-dimensional material that can be obtained experimentally.[1]

In this chapter, we will briefly review the studies and the findings on graphene and its nanodevices, the fabrication technologies, the future challenges, and the possible solution for application aspect.

1.1 General Properties of Graphene

Graphene is a single layer of carbon atoms assembling in a form of two-dimensional hexagon structure. These carbon atoms connect to each other through a sp^2 hybrid C-C bonding with π-electron clouds. One unit cell of graphene consists of two carbon atoms. These two atoms (A and B) have great symmetric that can be revealed by calculating its band structure. The many interesting physical properties

are stemmed from its unique "Dirac cone" band structure, its conduction band and valence band connects at K and K' points (so called Dirac point) with a linear E-k distribution. So the carriers in graphene is regarded as "massless" Dirac fermion $m^* = \hbar(\partial E^2/k^2)^{-1}$. This massless property and associated high Fermi velocity endue graphene an extraordinarily high mobility up to 140,000 $\mathrm{cm}^2/(\mathrm{Vs})$ at room temperature.[3] Apart from this, new physics such as the angular dependent Klein tunneling,[4, 5] half integer spin Hall effect,[6] the valley-spin states in bilayer graphene[7–9] and the recent exciting superconductivity in twisted bilayer graphene,[10] ignite scientific interests during the past 15 years. The discoveries and studies of these phenomena encourage the development of novel electronic devices with a new operation principle. Besides, graphene also has outstanding mechanical properties. The Young's modulus of graphene is $\sim$ 1000 Pa,[11] 10 times higher than that of silicon. On one hand, such a stiff material is suitable for high frequency mechanical resonator and oscillator.[12, 13] On the other hand, it can be used as a template for other materials or substrates to enhance their optical properties, such as photo absorption.[14]

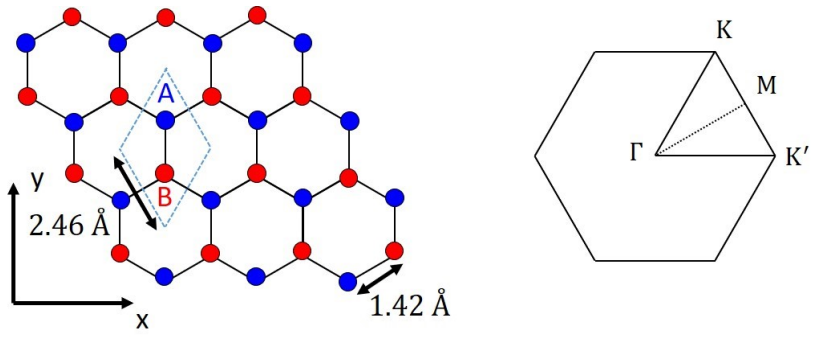

FIGURE 1.1: Lattice structure and the Brillouin zone of monolayer graphene.

To obtain graphene, several efficient methods have been demonstrated. First is the mechanical exfoliation method. By using a scotch tape, one could mechanically isolate layered graphene flakes from a bulk high oriented pyrolytic graphite (HOPG). These flakes can be then transferred to the prepared substrate. The mechanical exfoliation fabricated graphene has single crystalline lattice, which is

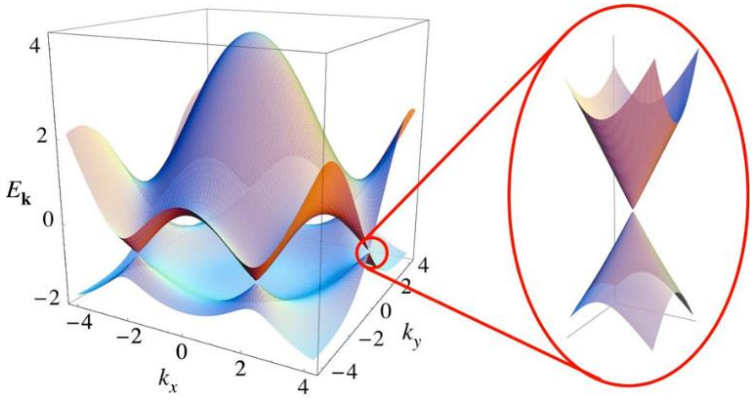

FIGURE 1.2: Band structure and the zoom up of the "K" point of monolayer graphene. The figure is cited from Ref [2]

necessary for fundamental physics studies. However, it is hard to control the size, or identify the layers of exfoliated grpahene flakes compared to other techniques such as chemical vapor deposition (CVD).

Chemical vapor deposition (CVD) is also a common method to obtain large scale graphene (1×1 cm^2).[15] CVD is a form of epitaxy grow process. Using CVD, graphene can be synthesized on the surface of Cu, Ni, In, Re, etc. Synthesized grpahene sheet can be transferred to another substrate through a wet transfer process. In the beginning, the inevitable grain boundary in CVD grown graphene limits its properties and the applications. During the past ten years, many efforts on CVD process have been paid to improve the quality of CVD grown graphene. Besides, there are also many methods such as heating silicon carbide (SiC) a temperature higher than 1100° C at a low pressures of $\sim 10^{-6}$torr.[16]

1.2 Ambipolar Transport in Graphene Field Effect Transistor

Through a general top-down nano-fabrication process, graphene sheet can be fabricated into field effect transistor (FET). Owning to the Dirac cone band structure, a graphene FET shows ambipolar as illustrated in fig 1.3. At a fixed source-drain bias voltage ($V_{\mathrm{d}} = 0.001\,\mathrm{V}$), current is measured with back gate voltage V_{g} sweeping from -40 V to 40,V. At region $-40\,\mathrm{V} < V_{\mathrm{g}} < 7\,\mathrm{V}$, where the Fermi energy is within the graphene valence band, source-drain current decreased with positively

increasing back gate voltage. At $V_g = 7\,V$, where the carrier density and I_d reach their minimum. In such I_d-V_g plotting, this point is known as "charge neutrality point (CNP)", which is corresponding to the "Dirac point". With further increasing back gate voltage, source-drain current increased again as the Fermi energy is tunned up and enters the conduction band. In this FET, the position of CNP is at the right side of zero back gate voltage, means without gate bias induced promote doping, the main carrier in graphene is hole (p-doped). A number of disorder sources such as substrate dangling bonds, oxygen adsorbents, fabrication residue, *etc.*, will cause this initial doping in graphene.[12–14]

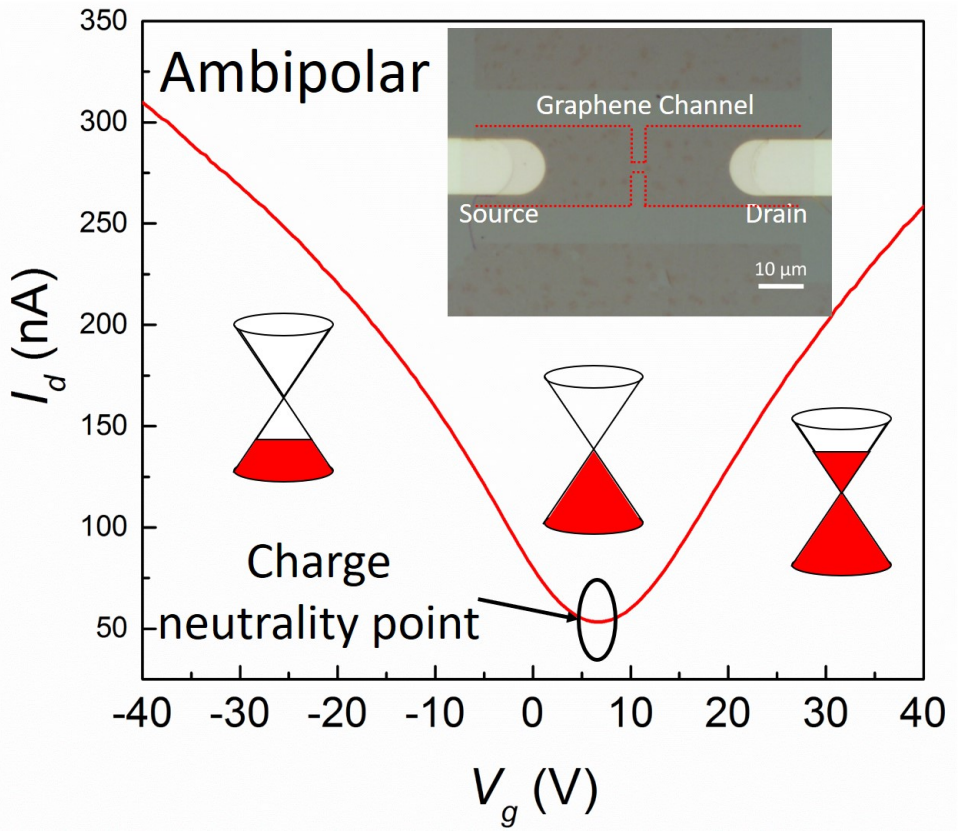

FIGURE 1.3: The source-drain current (I_d) as a function of back gate voltage (V_g) transfer curve of a graphene FET obtained at room temperature. Top insert is the optical photo of the FET. Scale bar is 10 μm. Three schematic illustrate the position of Fermi energy (red color filled) at different gate voltage.

From the data, the field effect mobility μ_{eff} can be extracted according to the equation[20]

$$\mu_{eff} = g_m l / w C_g V_d \tag{1.1}$$

where l and w are the length and width of graphene FET, $g_{\mathrm{m}} = dI_{\mathrm{d}}/dV_{\mathrm{g}}$ is the differential transconductance,V_{d} is the source-drain bias voltage, and $C_{\mathrm{g}} = wl\varepsilon\varepsilon_0/t$ is the gate capacitance with ε_0 being the vacuum permittivity, $\varepsilon = (1+4)/2$ being the relative permittivity (here we considering the silicon/silicon dioxide substrate screening)and $t = 285\,\mathrm{nm}$ being the thickness of silicon dioxide layer. Besides, from the shift of the CNP, one can estimate how much the graphene is doped by its environment through equation:

$$n = C_{\mathrm{g}}(V_{\mathrm{CNP}} - V_{\mathrm{g}})/e \tag{1.2}$$

where n is the gate dependent carrier density, V_{CNP} is the position of CNP in $I_{\mathrm{d}} - V_{\mathrm{g}}$ transfer curve, e is the electron charge.

In addition, the mobility and carrier density can be also extract by fitting the ambipolar curve to equation [21]

$$R_{\mathrm{total}} = R_{\mathrm{c}} + \frac{l}{w}\frac{1}{\mu_{\mathrm{eff}} n(V_{\mathrm{g}} - V_{\mathrm{CNP}})} \tag{1.3}$$

where n is the gate dependent carrier density, R_{c} is the contact resistance, $R_{\mathrm{total}} = \frac{V_{\mathrm{d}}}{I_{\mathrm{d}}}$ is the total resistance.

In graphene, such initial doping will decrease the carrier mobility. Many considerable doping sources such as fabrication residues, substrate roughness, dangling bonds, gas molecule adsorption, *etc.* These doping sources will induce charge transfer phenomena at different locations of graphene. As a result, the Fermi energy of the whole graphene is twisted and charge puddles are formed, which is also the reason why the carrier density does not vanish at V_{CNP}. This has been investigated by using STM, customized AFM mapping.[12–14]

To improve the device properties, several efficient approaches such as current annealing, thermal annealing, suspension of graphene channel and the most popular encapsulation with hexagon boron nitride (h-BN) have been demonstrated. Even though, the doping are difficult to remove completely.[13]

1.3 Energy Gap Opening and Carrier Confinement in Graphene Nanoribbon

Although there are great great scientific motivations to graphene application, it is still limited by several problems. One, also the biggest problem was the lacking of band gap. But, soon after we found an energy gap can be opened by patterning graphene into a graphene nanoribbon (GNR).[22] Importantly, the scale of the energy gap in GNR strongly depends on their widths. So this simple GNR is regarded as a building block for other complex devices (*i.e.,* quantum dot,[1–7, 10] resonant diode [31, 32] and tunneling FET)[33]. Although, the definition of this energy gap differs from the "band gap" in other semiconductor materials. It comes from the lateral confinement when the width of GNR approaches the scale of a few tens of nanometer. In additional, in experiment the line edge roughness and uncontrollable initial doping make the energy gap disordered. Because of that, we usually call this energy gap *"transport gap"*.[16–18]

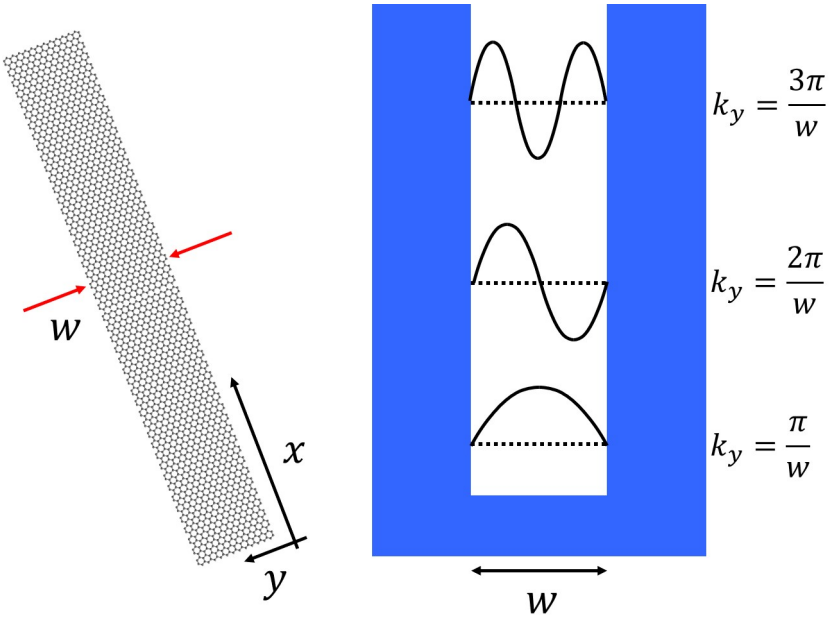

FIGURE 1.4: Illustration of Dirac particle confinement in graphene nanoribbon.

Now we discuss the size confinement induced energy gap in GNR. Assuming we have a GNR with a width w and a length l. From the basic of quantum mechanics, we know when the w is approaching to very small scale, *i.e.*, less than 50 nm, the wave function of electrons are strongly confined in this direction resulting in quantized electronic states spectrum as illustrated in Fig1.4. The band gap of GNR can be briefly expressed as[22]

$$E = \pm\hbar\nu_{\mathrm{F}}\sqrt{k_{\mathrm{x}}^2 + (\pi/nw)^2} \tag{1.4}$$

where $\hbar$ is the Plank constant, ν_{F} is the Fermi velocity, k_{x} and $k_{\mathrm{y}} = \pi/nw$ are the momentum vectors along "x" and "y" directions respectively. So we obtain an energy gap arises between the valence band maximum and conduction band bottom as illustrated in Fig 1.5. Accordingly, the relationship between energy gap E_{gap} and GNR width can be simplified as:

$$E_{\mathrm{gap}} \sim \hbar\nu_{\mathrm{F}}\Delta k \sim \hbar\nu_{\mathrm{F}}/w \tag{1.5}$$

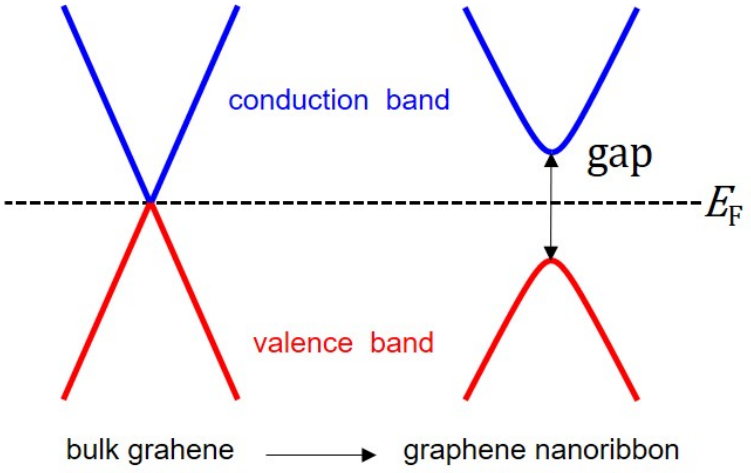

FIGURE 1.5: Illustration of energy gap opening in graphene nanoribbon.

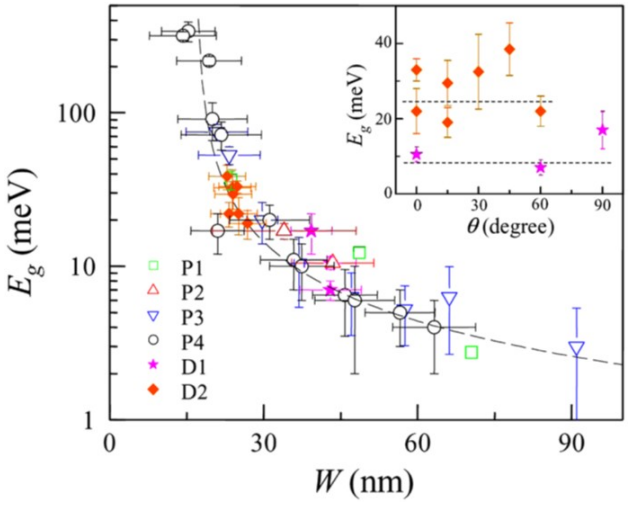

FIGURE 1.6: The width dependent energy gap in graphene nanoribbon. The figure is cited from Ref [22]

Such width dependent energy gap behaviour has been observed by Han *et al.* in 2007.[22] Using e-beam lithography patterning technique they successfully patterned GNRs with a serious dimensions varied from 100 nm to 14 nm (see figure1.6).[22] Later this dependence has been confirmed by other reports.[18, 39] In principle, such size dependent energy gap opening behaviour enables nanodevice band structure engineering, *e.g.*, a graphene quantum dot (QD) or single electron transistor (SET). But the e-beam lithography patterning technique has a limitation on the line edge roughness in a scale of a few nanometer, which results in a disordered band structure. This is another disorder source apart from the initial doping sources, which will significantly change the properties of GNR's edge states, leading to weak localization and Coulomb blockade effects.[16–18, 39] For the sake of a better discussion, we will first explain the Coulomb blockade in QD and SET systems and then come back to that in a GNR.

1.4 Coulomb Blockade in Single Electron Transistors

Single electron transistor (SET) is a device that allows small amount of electrons transport through the semiconductor channel.[30, 41] It has a similar structure to FET. The main difference is the charge and electronic states of carriers in the SET are quantized. Figure1.7 illustrates the energy diagram of a SET. It consists of a quantized conductive island in the center (when this island is small enough, the electronic states of one charge become discrete. At the moment, it is called a quantum dot), two relatively smaller tunnel junctions and two metallic leads sitting at each sides of the center island. The island is known as charging island. The quantized charge states can be occupied by one electron (if we consider the spin degeneracy, then two electrons with up and down spins).

When we apply a voltage V_{sd} at the metallic leads, a bias window $V_{\mathrm{L}} - V_{\mathrm{R}} = -|e|V_{\mathrm{sd}}$ is created. Phenomenologyly, assuming one electron currently sits at the deeper state and it does not have enough energy to access the bias window to tunnel out through the barrier, this electron is confined in the charging island. This electron will repel the other incoming electrons because of the Coulomb force. As a result, the next charge states is lifted by a separation of ΔE_{c}, known as charging energy. To make the current flow, one can either increase the bias voltage so

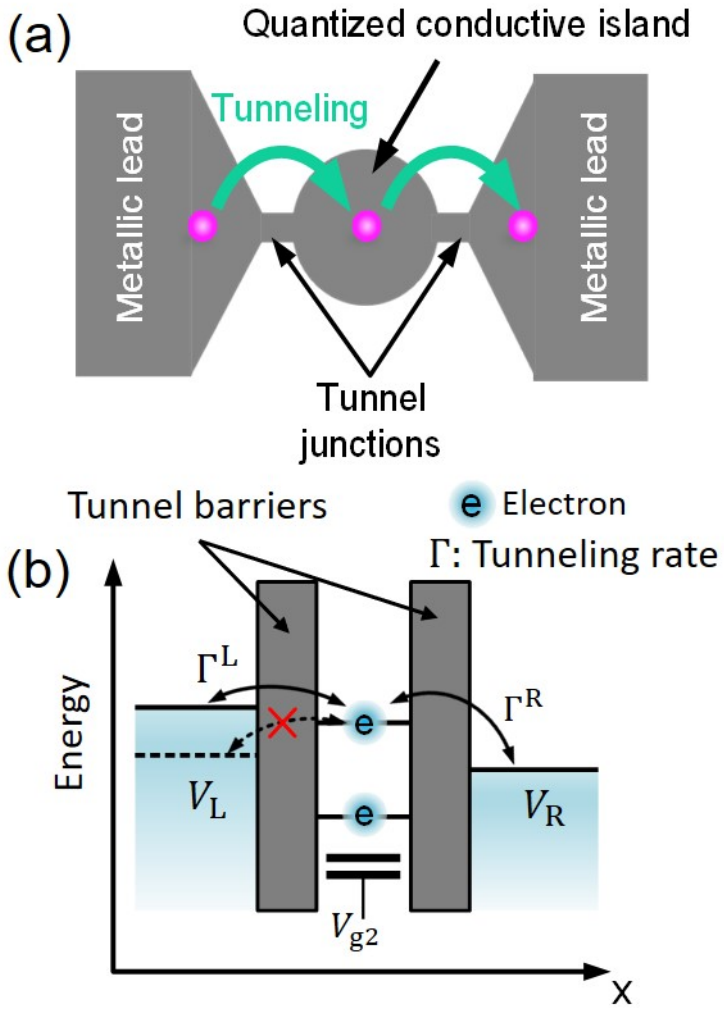

FIGURE 1.7: Schematic of single electron transistor. (a) The structure can be used to geometrically define single electron transistor. (b) the energy diagram of a single electron transistor

the incoming electrons have enough energy to access the higher charge states, or tune the charge states through a gate electrode. When a solo state is tunned to the center of the bias window, the electron can elastically tunnel through the tunnel barrier and the tunneling rate of this electron Γ reaches its maximum. This phenomena is called Coulomb blockade.[41]

The equivalent circuit of an SET is illustrated in Fig1.8. The total capacitance C_Σ of the SET is the sum of the gate capacitance C_g and the tunnel junctions capacitance C_L and C_R:

$$C_\Sigma = C_g + C_L + C_R \tag{1.6}$$

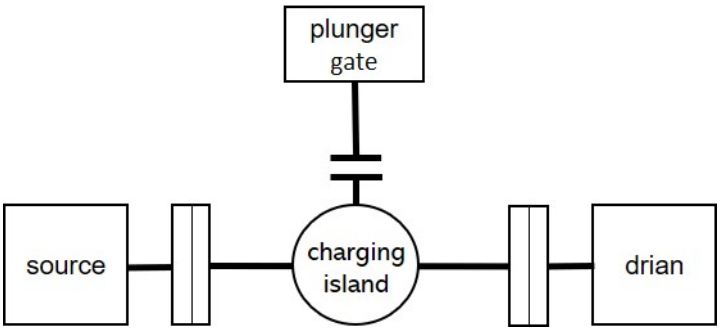

FIGURE 1.8: The equivalent circuit of SET

If the Coulomb interaction energy between electrons on the island dominates the energy scales, the charging energy is the dominate energy scale. For the sake of the description, we assume the disc like charging island is carrying N electrons. The electrostatic energy of the charging island is then:

$$E_{\text{elstat}}(N) = \frac{e^2 N^2}{2C_\Sigma} \tag{1.7}$$

When we want to add another more electron to the island, the necessary charging energy becomes:

$$E_c(N+1) = E_{\text{elstat}}(N+1) - E_{\text{elstat}}(N) = \frac{e^2}{C_\Sigma}(N+1/2) \approx \frac{e^2}{C_\Sigma}N \tag{1.8}$$

The difference of the charging energy is then:

$$\Delta E_{\text{c}} = E_{\text{c}}(N+1) - E_{\text{c}}(N) = \frac{e^2}{C_\Sigma} \tag{1.9}$$

Now we move to the transport characteristic of SET. A schematic representation of a SET system is shown in Fig1.9 for a better discussion. At low temperature, the electronic levels in the source and drain contacts are filled from the conduction band bottom to the chemical potential μ_{S} and μ_{D}. The positions of charge states μ_{N} can be shifted by applying a plunger gate voltage. When $\mu_{\text{S}} > \mu_{\text{N}}(V_{\text{pg}}) > \mu_{\text{D}}$, a finite source-drain current can flow. Increasing the plunger gate voltage, the current keeps flowing until $\mu_{\text{D}} = \mu_{\text{N}}(V_{\text{pg}} + \Delta V_{\text{pg}}) = \mu_{\text{N}}(V_{\text{pg}}) - |e|\alpha_{\text{pg}}\Delta V_{\text{pg}}$, where it drops to zero because the Nth electron level is lifted outside of the bias window $-|e|V_{\text{sd}}$. From the above equation, we obtain $e|\Delta V_{\text{pg}}| = \frac{e|V_{\text{sd}}|}{\alpha_{\text{pg}}}$, implies the plunger

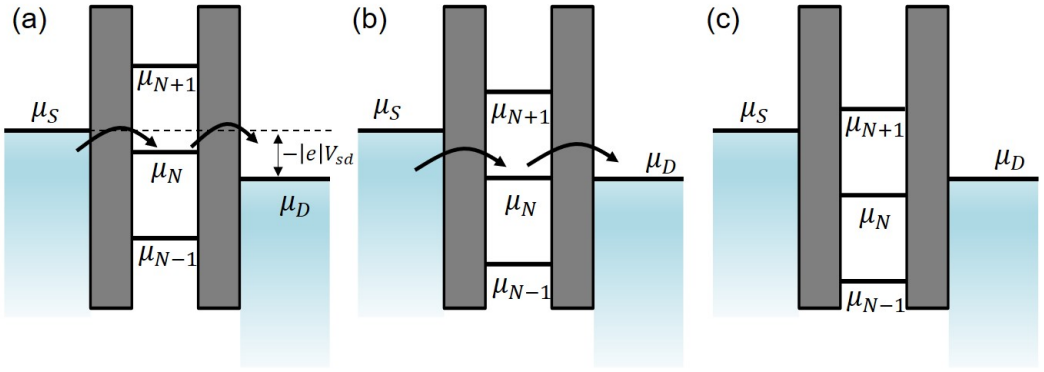

FIGURE 1.9: Schematic of electron transport in SET with a finite bias applied at its source drain electrode. (a) Current flow region that $\mu_S > \mu_N(V_{pg}) > \mu_D$. (b) The situation $\mu_D = \mu_N(V_{pg} + \Delta V_{pg})$ for current onset. (c) The situation $\mu_D > \mu_N(V_{pg} + \Delta V_{pg})$, $\mu_S < \mu_{N+1}(V_{pg} + \Delta V_{pg})$, the blockade region.

gate contribution on the chemical potential tunning, where α_{pg} is the plunger gate lever arm. This can be reflected in the current measurement as shown in Fig 1.10.

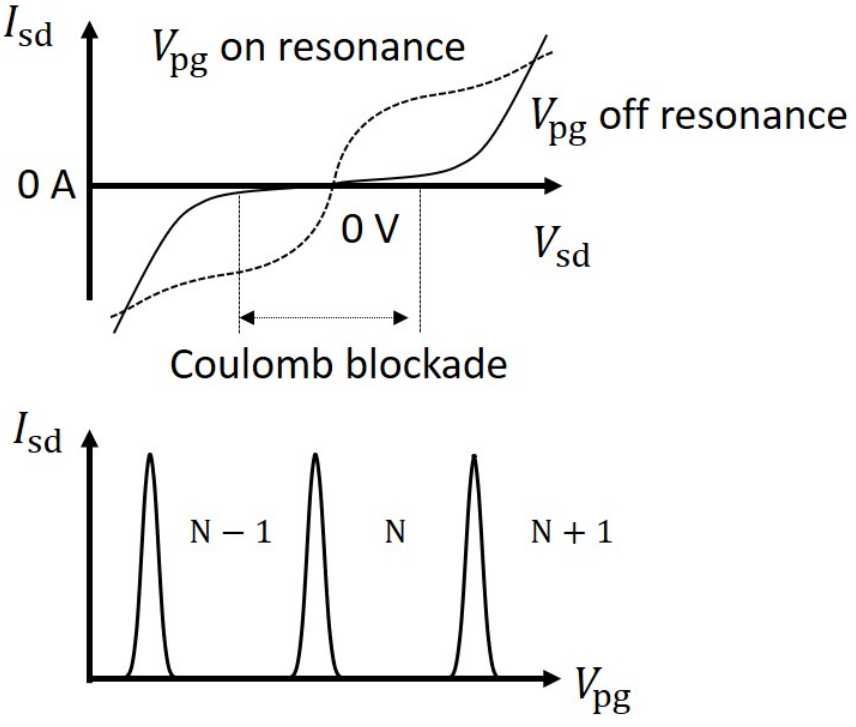

FIGURE 1.10: Transport characteristic in a SET. (a) Source-drain current I_{sd} as a function of bias voltage V_{sd} with a V_{pg} set at current peak position (on resonance, dashed line) and current valley (off resonance, solid line). (b) I_{sd} as a function of plunger gate voltage V_{pg} at a finite bias voltage $|eV\text{sd}| < e^2/C_\Sigma$

To observe the Coulomb blockade, there are several considerations need to be satisfied. First, the tunneling resistance R_t of the SET should be significantly larger than the resistance quantum h/e_2, means that the tunneling coupling of

the SET is weak so the charge states are quantized. Second consideration is the temperature. It should be smaller than the charging energy, *i.e.*, $k_{\mathrm{B}}T \ll \frac{e^2}{C_\Sigma}$. The third consideration is the electric measurement. In the measurement, the scale of bias window $-|V_{\mathrm{sd}}|$ should be smaller than the charging energy $|\Delta E_{\mathrm{c}}|$. Figure 1.10 (a) plots the SET source-drain current as a function of V_{sd}. The edges of non-linear $I_{\mathrm{sd}} - V_{\mathrm{sd}}$ Coulomb blockade gap corresponding to the charging energy $\Delta E_{\mathrm{c}} = \frac{e^2}{C_\Sigma} = -eV_{\mathrm{sd}}$. Sweeping the plunger gate voltage at a fixed bias voltage $|eV_{sd}| < e^2/C_\Sigma$, one can observe resonant peak features as shown in Fig 1.10 (b), corresponding to Fig 1.9. The at the current peaks, electrons from source contact elastically tunnel through the barriers when one charge state is sitting in the center of bias window. Sweeping the gate voltage will shift this state, therefore current drops. When the initial state is moved outside from the bias widow, the conductance is forbidden. The number of electrons confined on the island is fixed. Current can not flow until a new charge state access the bias window. This oscillation peak feature is called Coulomb oscillation, which implies the single electron transport behaviour in the SET.

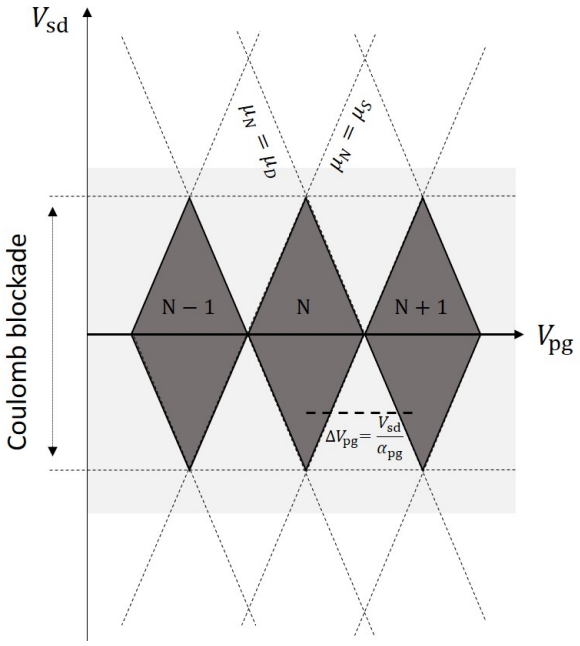

FIGURE 1.11: Stability diagram and Coulomb diamonds in SET

When we plot the source-drain current as a function of both bias voltage and plunger gate voltage, so called stability diagram, we will observe diamond patterns that represent the Coulomb blockade gap and Coulomb oscillation (Fig 1.11). Inside the diamond, current flow is forbidden. From the geometry of the diamond, we can obtain the maximum Coulomb gap and the plunger gate voltage gap. The

scale of two gaps can be used to calculate the charging energy, and the total capacitance of the charging island. The diamond edges denote the situation $\mu_N = \mu_D$ and $\mu_N = \mu_S$, from the space of the diamond, we can obtain the plunger gate lever arm α_{pg}. This diamond patterns are called Coulomb diamonds, which are the finger prints of single electron transport through SET.

1.5 Disorder Induced Coulomb Blockade in Graphene Nanoribbons

After the description of Coulomb blockade in SET, now we move back to the electric transport in graphene nanoribbons. As we introduced briefly, energy gap opening is observed and characterized experimentally by Han *et al* in 2007 first.[22] Apart from the energy gap, they also measured resonant current peaks in the GNRs at low temperature. In the stability diagram plotting some GNRs shows SET and quantum dot behaviours, *i.e.*, Coulomb diamond characteristic. Soon after that, Ponomarenko *et al* observed stochastic Coulomb blockade, *i.e.*, overlapped, not uniform diamond patterns, in a graphene SET quantum dot, suggesting the existence of a number of smaller dots in the device, possibly caused by the roughness at their quantum dot strips edges. This concept has been confirmed by theoretically calculating the carrier density of states in a GNR with rough edges (Fig 1.12).[40]

Stampfer *et al* reported an experimental study focusing on the Coulomb diamond behaviour in geometrically defined SET and nanoribbon, which confirmed even a nanoribbon can exhibit SET-like behaviour in 2009.[16] According to their observation, they proposed a concept of a high order disorder in the nanoribbon energy gap that stemmed from both edge roughness and GNR surrounding environment doping.[12–14] This strongly disordered energy gap is defined as the *transportgap*.

In our experiments, similar behaviour was observed. Here we introduce the transfer curve of a GNR measured at a temperature of 5 K (Fig1.13). The width of GNR is 20 nm and the length is 100 nm. Compared to the ambipolar transfer curve shown in Fig 1.3, we observe a low conductance region from $0\,\mathrm{V} < V_{\mathrm{g}} < 23\,\mathrm{V}$, where close to the CNP position. This region is the *transportgap*. Within the transport gap, resonant peaks are read.

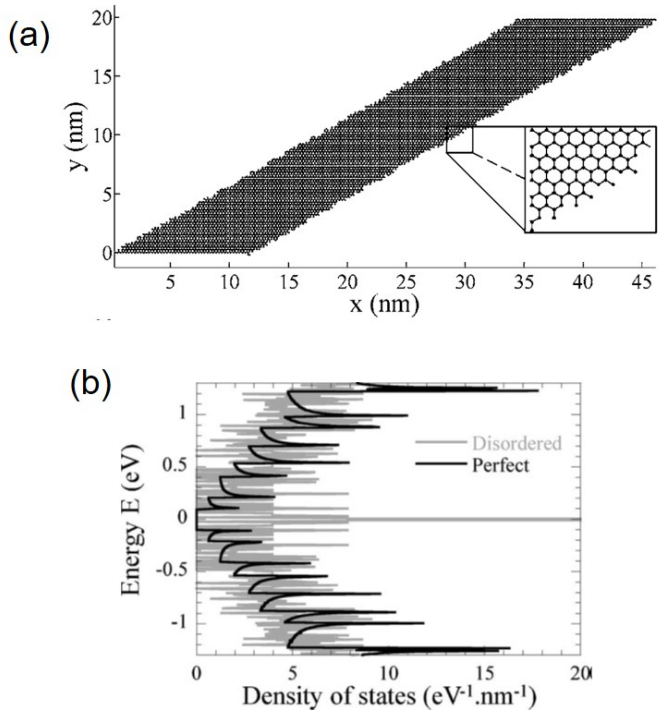

FIGURE 1.12: Theoretical calculation of the density of states (DOS) in a GNR with rough edge. (a) Representation of the disordered graphene nanoribbon used for DOS calculation. (b) Calculated DOS in a GNR with and without (perfect armchair edge) edge roughness. The ribbon width is 6 nm, length is 40 nm. These figures are cited from Ref [40]

Focus on the transport gap region, we observed strongly disordered Coulomb diamond-like patterns, which is the signature of multiple islands SET. Moreover, the size of diamonds varies, indicating the size and the number of charging islands varies since the charging energy ΔE_c inversely proportional to the size of the charging island r.

To provide a visible view for the transport gap, a simple illustration of the disordered transport gap is presented in Fig 1.15. Due to the line edge roughness, the energy gap stemmed from GNR widths varies. Apart from that, the local doping sources caused potential inhomogeneity GNR surrounding doping makes the disorder even stronger. Under this circumstance, electrons can be localized in GNR as long as the Fermi energy E_F lies in two tunable energy gaps (Fig 1.15 (a)). If the "potential valley" is small enough to form quantized charge states, single dot-like behaviour can be expected. Sweeping the universal back gate voltage, the Fermi energy may access another "potential valley" leading to multiple localization states formation, until the Fermi energy completely fill this two valleys, these localized states, or dots start to overlap, merge and finally become a larger dot.

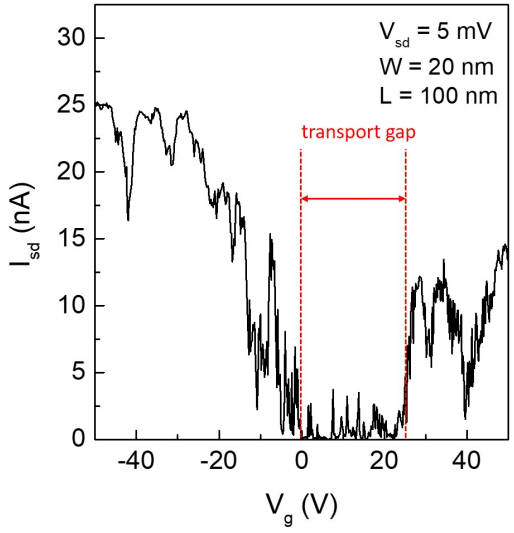

FIGURE 1.13: Transfer curve of a graphene nanoribbon obtained at low temperature (5 K). The red dashed lines are eye guides of the transport gap edges. The ribbon width is 20 nm, length is 100 nm.

1.6 Overview of This Work

A single quantum dot (QD) graphene SET enables the observation and studies of single Dirac fermions transport. It is of interest in the field of foundamental physics studies such as Coulomb blockade, excieted states, electron-phonon interaction,

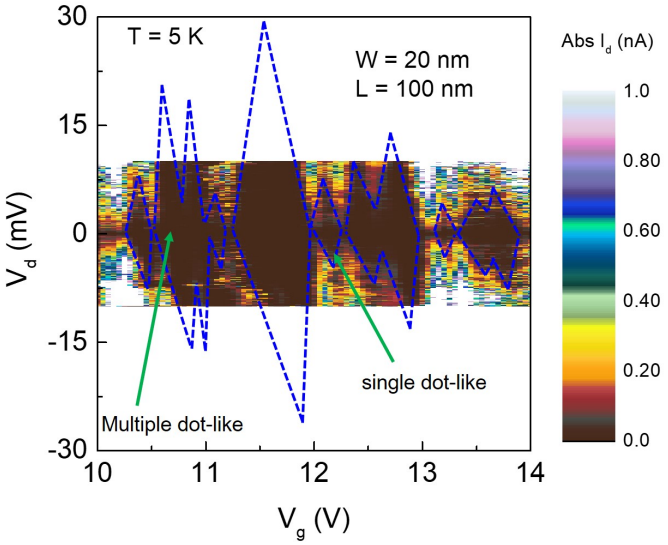

FIGURE 1.14: Stability diagram of the GNR shown in Fig 1.13. Heavily merged Coulomb diamonds with unclear edges are observed, indicating the existence of a number of small islands/quantum dots

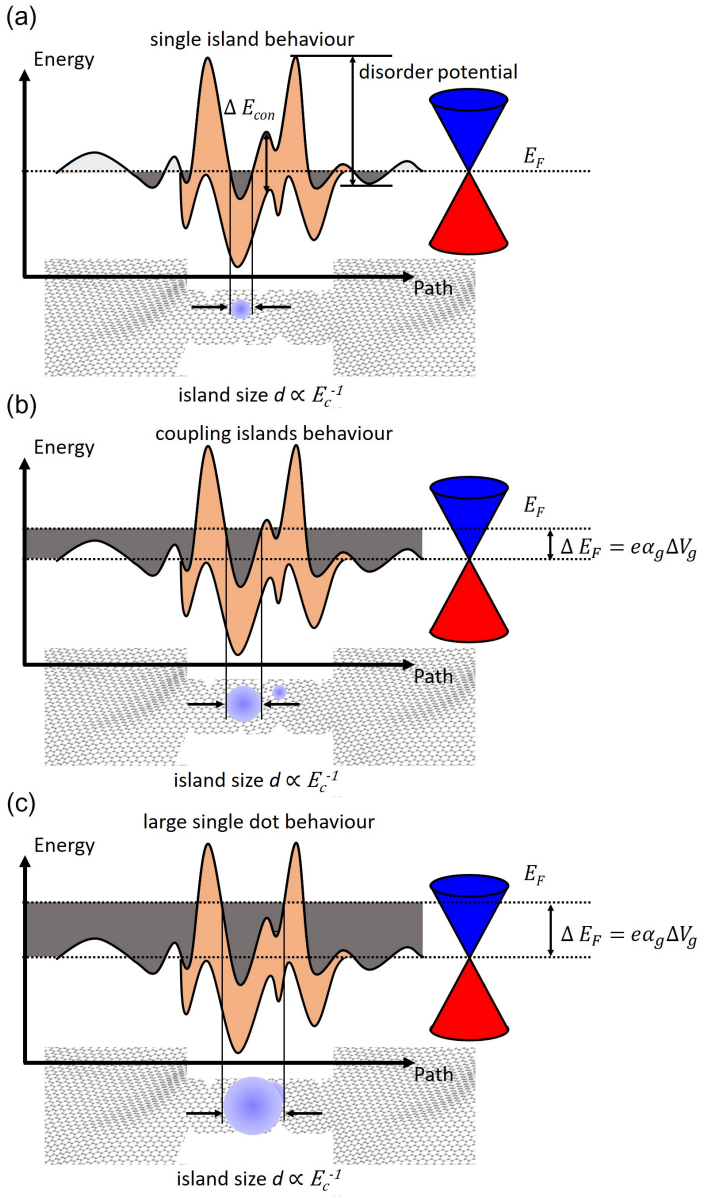

FIGURE 1.15: Schematic illustration of small localization states formation and evolution in a transport gap opened GNR.

etc. In the appliction aspect, it can be used as ultra-high sensitive electron meter and sensor. Recently, the discovery of "valley-spin" states in bilayer grapehne SET encourages the applications in the valley degeneracy based electronics.[9]

Since a GNR can exhibit single dot-like SET behaviour, a concept of developing GNR to SET emerges. For these purpose, efforts have been paid to investigate i) carrier transport in GNR, ii) the dominate localization mechanism (week localization or Coulomb blockade effect), iii) size dependent of the single dot-like SET properties. Oostinga *et al* arguid the dominate localization mechanism is

the Coulomb blockade gap rather than the weak localization by comparing the Coulomb diamond patterns with and without a perpendicular magnet field.[36] Terrés *et al* compared the SET-like behaviour in GNRs with different widths and lengths.[18] In the experiments, it is found that Coulomb blockade gap depends on the GNR widths rather than GNR lengths, but it doesn't mean that length is not important for SET behaviour. This is not only because of the doping inhomogeneity effects gain with length, but also the electron transport length in such GNR is limited by its Coulomb gap and its width.[31, 43]

In general, it is difficult to control all the parameters at the same time, especial the roughness at GNR edges due to the limitation of current nanopatterning technology. On the other hand, the controlling over the potential inhomogeneity seems to be easier. The common concept is first to obtain a clean graphene bulk sheet, then use a local side/top gate to tune the tunnel coupling, *i.e.* the position of the transport gap of the GNR to construct SET band structure, the so called electrostatic or gate defined GNR SET. This method is an efficient approach to realize quantum dot and SET in graphene. But, we need room to place these plunger gates, that makes the whole SET system larger.

Here we reconsidered the concept of electrostatic defined SET. One plunger gate is necessary to tune the chemical potential of charge states. We only need to see a few clear states for single carrier tunneling operation, but the number of the carriers on the island should be small, *i. e.*, $N = 0, 1, 2$. If the band structure of the SET satisfy this situation, we then don't need extra gates to change the tunnel barriers, so the whole device could be more compact.

The electrostatic gating is initially a local promote doping approach that can shift the Fermi energy of the local semiconductor channel. In another word, it brings inhomogeneity to the device in a *controllable* manner. If we can induce initial doping to GNR in a controllable mater, single dot SET band structure can be expected. However, this concept has not been reported before us.

In my study, I focused on *dopingcontrolingraphenenanoribbon* in terms of i) doping level control, ii) spatial doping control through different approach. In chapter two, I will introduce the device fabrication process and characterization set up including the materials, instruments we used. In chapter three, four and five, individual doping control technique are presented. Lastly, a summary and future prospect of my work are presented in chapter six.

Bibliography

[1] Novoselov, K. S.; Geim,A. K.; Morozov, S. V.; Jiang, D.; Zhang, Y.; Dubonos, S. V.; Grigorieva, I. V.; Firsov, A. A. Electric Field Effect in Atomically Thin Carbon Films. *Science* **2004**, *306* 5696, 666-669.

[2] Neto, A.C.; Guinea, F.; Peres, N.M.; Novoselov, K.S.; Geim, A.K. The Electronic Properties of Graphene. *Rev. Mod. Phys.* **2009** *81*, 109.

[3] Wang, L.; Meric, I.; Huang, P.Y.; Gao, Q.; Gao, Y.; Tran, H.; Taniguchi, T.; Watanabe, K.; Campos, L.M.; Muller, D.A.; Guo, J. One-Dimensional Electrical Contact to a Two-Dimensional Material. *Science* **2013** *342*, 614-617.

[4] Katsnelson, M. I.; Novoselov1, K. S.; Geim1,A. K. Chiral Tunnelling and the Klein Paradox in Graphene. *Nature Physics* **2006**, *2* 620-625.

[5] Stander, N.; Huard, B.; Goldhaber-Gordon D. Evidence for Klein Tunneling in Graphene *p-n* Junctions. *Phys. Rev. lett. 102* 026807.

[6] Novoselov, K. S.; Geim,A. K.; Morozov, S. V.; Jiang, D.; Katsnelson, M.I.; Grigorieva, I.V.; Dubonos, S.V.; Firsov, A.A. Two-Dimensional Gas of Massless Dirac Fermions in Graphene. *Nature* **2005** *438*, 197.

[7] Xiao, D.; Yao, W.; Niu, Q. Valley-Contrasting Physics in Graphene: Magnetic Moment and Topological Transport. *Phys. Rev. Lett.* **2007** *99*, 236809.

[8] Martin, I.; Blanter, Ya. M.; Morpurgo, A. F. Topological Confinement in Bilayer Graphene. *Phys. Rev. Lett.* **2008** *100* 036804.

[9] Qiao, Z.; Tse, W.; Jiang, H.; Yao, Y.; Niu, Q. Two-Dimensional Topological Insulator State and Topological Phase Transition in Bilayer Graphene. *Phys. Rev. Lett.* **2011**, *107*, 256801.

[10] Cao, Y.; Fatemi, V.; Fang, S.; Watanabe, K.; Taniguchi, T.; Kaxiras, E.; Jarillo-Herrero, P. Unconventional Superconductivity in Magic-Angle Graphene Superlattices. *Nature* **2018** *556*, 43–50.

[11] Lee, C.; Wei, X.; Kysar, J. W.; Hone, J. Measurement of the Elastic Properties and Intrinsic Strength of Monolayer Graphene. *Science* **2008** *321* 385-388.

[12] Bunch, J.S.; Van Der Zande, A.M.; Verbridge, S.S.; Frank, I.W.; Tanenbaum, D.M.; Parpia, J.M.; Craighead, H.G.; McEuen, P.L. Electromechanical Resonators from Graphene Sheets. *Science* **2007** *315*, 490-493.

[13] Chen, C.; Lee, S.; Deshpande, V.V.; Lee, G.H.; Lekas, M.; Shepard, K.; Hone, J. Graphene Mechanical Oscillators with Tunable Frequency. *Nature Nanotech.* **2013** *8*, 923.

[14] Matthaiakakis, N.; Yan, X.; Mizuta, H.; Charlton, M.D.B. Tuneable Strong Optical Absorption in a Graphene-Insulator-Metal Hybrid Plasmonic Device. *Sci. Rep* **2017** *1*, 7303.

[15] Munoz, R.; Gómez-Aleixandre, C. Review of CVD Synthesis of Graphene. *Chem. Vap. Deposition* **2013** *19* 297-322.

[16] Mishra, N.; Boeckl, J.; Motta, N.; Iacopi, F. Graphene Growth on Silicon Carbide: A Review. 'textitPhys. Status Solidi A **2016** *213*, 2277-2289.

[17] Xue, J.; Sanchez-Yamagishi, J.; Bulmash, D., Jacquod, P.; Deshpande, A.; Watanabe, K.; Taniguchi, T.; Jarillo-Herrero, P.; LeRoy, B. J. Scanning Tunnelling Microscopy and Spectroscopy of Ultra-Flat Graphene on Hexagonal Boron Nitride *Nat. Mater.* **2011**, *10* 282–285.

[18] Zhang, Y.; Brar, V. W.; Girit, C.; Zettl, A.; Crommie, M. F. Origin of Spatial Charge Inhomogeneity in Graphene. *Nat. Phys.* **2009**, *5* 722-726.

[19] Samaddar, S.; Yudhistira, I.; Adam, S.; Courtois, H.; Winkelmann, C.B. Charge Puddles in Graphene Near the Dirac Point. *Phys. Rev. Lett.* **2016,** *116,* 126804.

[20] Schwierz, F. Graphene Transistors. *Nat. Nanotech* **2010** *5*, 487.

[21] Kim, S.; Nah, J.; Jo, I.; Shahrjerdi, D.; Colombo, L.; Yao, Z.; Tutuc, E.; Banerjee, S.K. Realization of a High Mobility Dual-Gated Graphene Field-Effect Transistor with Al_2O_3 Dielectric. *Appl. Phys. Lett.* **2009** *94* 062107.

[22] Han, M. Y.; Özyilmaz, B.; Zhang, Y.; Kim, P. Energy Band Engineering in Graphene Nanoribbon. Energy Band Engineering in Graphene Nanoribbon. *Phys. Rev. Lett.* **2007**, *98* 206805.

[23] Ponomarenko, L. A.; Schedin, F.; Katsnelson, M. I.; Yang, R.; Hill, E. W.; Novoselov, K. S.; Geim, A. K. Chaotic Dirac Billiard in Graphene Quantum Dots. *Science* **2008,** *320*, 356-358.

[24] Roulleau, P.; Baer, S.; Choi, T.; Molitor, F.; Güttinger, J.; Müller, T.; Dröscher, S.; Ensslin, K.; Ihn, T. Coherent Electron-Phonon Coupling in Tailored Quantum Systems. *Nat. Commun.* **2011,** *2,* 239.

[25] Liu, X.L.; Hug, D.; Vandersypen, L.M. Gate-Defined Graphene Double Quantum Dot and Excited State Spectroscopy. *Nano Lett.*, **2010,** *10,* 1623-1627.

[26] Volk, C.; Fringes, S.; Terrés, B.; Dauber, J.; Engels, S.; Trellenkamp, S.; Stampfer, C.; Electronic Excited States in Bilayer Graphene Double Quantum Dots. *Nano Lett.* **2011,** *11,* 3581-3586.

[27] Güttinger, J.; Stampfer, C.; Hellmüller, S.; Molitor, F.; Ihn, T.; Ensslin, K. Charge Detection in Graphene Quantum Dots. *Appl. Phys. Lett.* **2008,** *93,* 212102.

[28] Wang, L.J.; Cao, G.; Tu, T.; Li, H.O.; Zhou, C.; Hao, X.J.; Su, Z.; Guo, G.C.; Jiang, H.W.; Guo, G.P. A Graphene Quantum Dot with a Single Electron Transistor as an Integrated Charge Sensor. *Appl. Phys. Lett.* **2010,** *97,* 262113.

[29] Barreiro, A.; van der Zant, H.S.; Vandersypen, L.M. Quantum Dots at Room Temperature Carved Out from Few-Layer Graphene. *Nano Lett.* **2012,** *12,* 6096-6100.

[30] Stampfer, C.; Schurtenberger, E.; Molitor, F.; Guttinger, J.; Ihn, T.; Ensslin, K.; Tunable Graphene Single Electron Transistor. *Nano Lett.* **2008,** *8,* 2378-2383.

[31] Britnell, L.; Gorbachev, R.V.; Geim, A.K.; Ponomarenko, L.A.; Mishchenko, A.; Greenaway, M.T.; Fromhold, T.M.; Novoselov, K.S.; Eaves, L. Resonant Tunnelling and Negative Differential Conductance in Graphene Transistors. *Nat. Comm.*, **2013** *4*, 1794.

[32] Song, Y.; Wu, H.C.; Guo, Y. Negative Differential Resistances in Graphene Double Barrier Resonant Tunneling Diodes. *Appl. Phys. Lett.* **2013** *102* 093118.

[33] Hamam, A.M.; Schmidt, M.E.; Muruganathan, M.; Suzuki, S.; Mizuta, H. Sub-10 nm Graphene Nano-Ribbon Tunnel Field-Effect Transistor. *Carbon* **2018** *126* 588-593.

[34] Stampfer, C.; Güttinger, J.; Hellüller, S.; Molitor, F.; Ensslin, K.; Ihn, T. Energy Gaps in Etched Graphene Nanoribbons. *Phys. Rev. Lett.* **2009,** *102,* 056403.

[35] Gallagher, P.; Todd, K.; Goldhaber-Gordon, D. Disorder-Induced Gap Behavior in Graphene Nanoribbons. *Phys. Rev. B* **2010,** *81,* 115409.

[36] Oostinga, J. B.; Sacé pé , B.; Craciun, M. F.; Morpurgo1, A. F. D. Magnetotransport Through Graphene Nanoribbons. *Phys. Rev. B* **2010,** *81,* 193408.

[37] Todd, K.; Chou, H.T.; Amasha, S.; Goldhaber-Gordon, D. Quantum Dot Behavior in Graphene Nanoconstrictions. *Nano Lett.* **2009,** *9,* 416-421.

[38] Terrés, B.; Dauber, J.; Volk, C.; Trellenkamp, S.; Wichmann, U.; Stampfer, C. Disorder Induced Coulomb Gaps in Graphene Constrictions with Different Aspect Ratios. *Appl. Phys. Lett.* **2010,** *98,* 032109.

[39] Molitor, F.; Stampfer, C.; Güttinger, J.; Jacobsen, A.; Ihn, T.; Ensslin, K. Energy and Transport Gaps in Etched Graphene Nanoribbons. *Semiconductor Science and Technology* **2010** *25*, 034002.

[40] Querlioz, D.; Apertet, Y.; Valentin, A.; Huet, K.; Bournel, A.; Galdin-Retailleau, S.; Dollfus, P. Suppression of the Orientation Effects on Bandgap in Graphene Nanoribbons in the Presence of Edge Disorder. *Appl. Phys. Lett.* **2008** *92*, 042108.

[41] Averin, D.V.; Likharev, K.K. Coulomb Blockade of Single-Electron Tunneling, and Coherent Oscillations in Small Tunnel Junctions. *Journal of low temperature physics* **1986** *62* 345-373.

[42] Ihn, T. *Semiconductor Nanostructures Quantum States and Electronic Transport*, (Oxford University Press, Oxford, 2009).

[43] Lherbier, A.; Biel, B.; Niquet, Y.M.; Roche, S. Transport Length Scales in Disordered Graphene-Based Materials: Strong Localization Regimes and Dimensionality Effects. *Phys. Rev. Lett.* **2008** *100*, 036803.

[44] Han, M. Y.; Brant, J. C.; Kim, P. Electron Transport in Disordered Graphene Nanoribbons. *Phys. Rev. Lett.* **2010** *104*, 056801.

Chapter 2

Device Fabrication and Characterization

As we briefly introduced, graphene nanoribbon has been demonstrated as a efficient way for transport gap opening due to the lateral confinement. The scale of this transport gap strongly depend on the nanoribbon width rather than its length. So far, graphene nanoribbons have been fabricated through both bottom-up and top-down approaches. They have their merits and their demerits, *i.e.,* bottom-up grown GNRs have perfect zigzag edge with atomic scale geometries. However, these GNRs suffers from the low yelting rate and the Schottky barrier at graphene-contact interface. In comparison, the contact properties in top-down fabricated GNRs are much better and can be improved further using a edge contact technique. However, the edge structure of top-down patterned GNRs are hard to control because of the line edge roughness of a few nanometer along the etching mask. It is clear that both approaches need more efforts to reduce their demerits. In our work, we only focus on top-down fabricated GNRs and their transport properties.

In this chapter, we will first introduce the fabrication process of top-down graphene nanodevices and then the keys to obtain *i.e.*, nanoribbon patterning.

2.1 Conventional Fabrication Process of Graphene Field Effect Transistor

To provide an overall view of the device fabrication of graphene FET, we first introduce a simple fabrication process. Our device fabrication start with the exfoliation of graphene from kish graphite and highly oriented pyrolytic graphite (HOPG) using a popular scotch tape. After roughly ten times of exfoliation, we past the scotch tape on a highly doped silicon substrate with ∼290nm-thick thermally grown silicon dioxide to transfer graphene. After the transfer, the sample is then put into acetone to clean the glue. The number of layers of graphen is characterized by the identifying their optical contrast on SiO_2/Si substrate and by fitting the 2-D peak of graphene Raman spectra.[1]

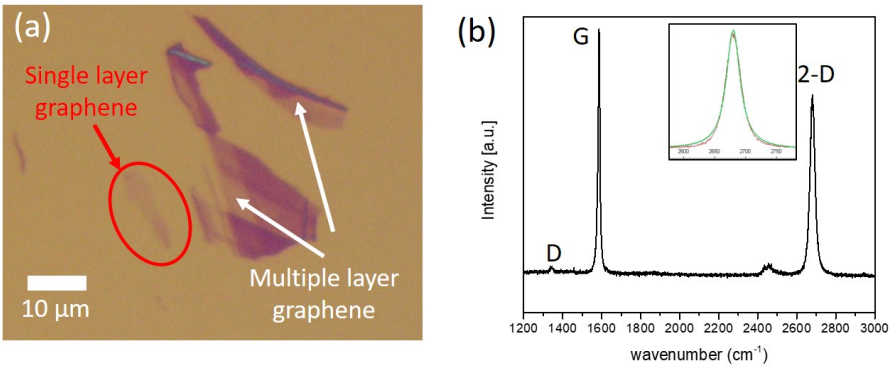

FIGURE 2.1: Graphene flakes on silicon dioxide substrate obtained by using mechanical exfoliation technique (a) and Raman spectra in the monolayer graphene shown in (a). The insert is zoom up of the 2-D band fitting

After the identification of monolayer or bilayer graphene, we then start to attach metallic contact on them. PMMA(A4)/MMA bilayer resist is spun on the substrate with a speed of 4000/2000 rmp. The designed pattern is wrote using a e-beam lithography technique. The used e-beam lithography system is ELS-7500 model of Elionix Inc, which has an acceleration voltage up to 50 kV. The standard e-beam dose for PMMA/MMA resist exposure varies from 210 µC/cm^2 After the development in 1:1 MIBK:IPA for 51 seconds and rinsing in IPA for another 30s, the exposed resist is removed so the designed pattern becomes clearly visible. The sample then is transferred to a e-beam evaporator for metal deposition. At a pressure of 10^{-5} Pa, 5 nm Cr with 75 nm Au on top were deposited on the substrate. After a lift-off procedure in acetone, the metal attached to graphene forms metallic contact while the other parts on the top of PMMA/MMA resist are removed.

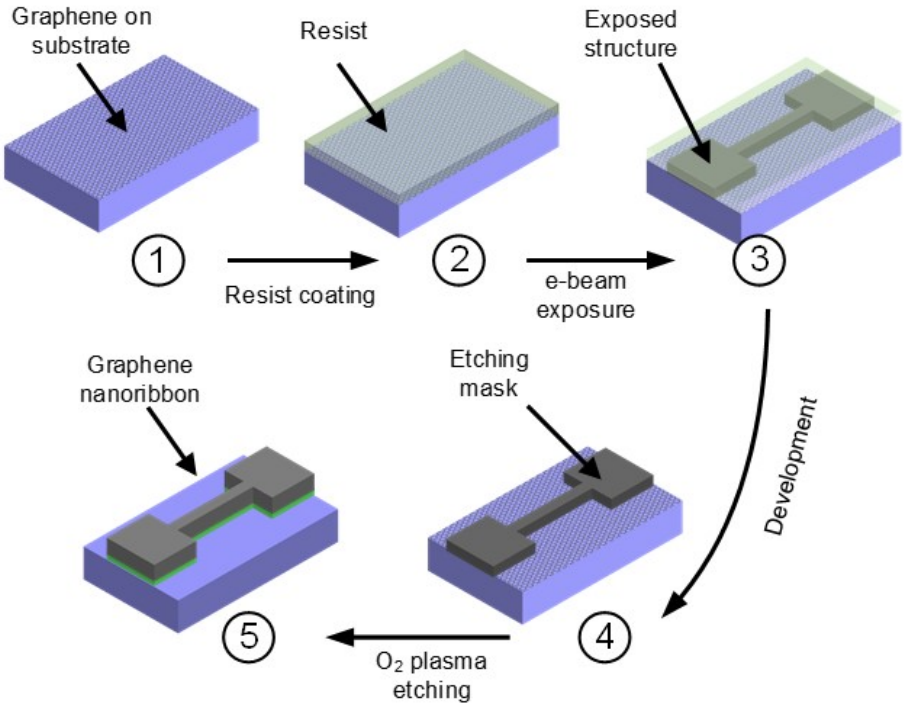

FIGURE 2.2: Schematic representation of the fabrication process of a graphene field effect transistor.

Lastly, graphene is patterned via another EBL procedure. Thereafter, a gentle oxgen plasma etching is preformed to etch out graphene, so the shape of the mask is transferred to graphene. In addition, patterning is strongly recommended after the deposition of contact metal to reduce the possibility of the Schottky barrier formation.

2.2 Optimizing Fabrication Process for Graphene Nanodevices

Importantly, the resist resolution directly limits the patterned GNR width. Normally, A4 PMMA has a reasonable resolution with our 50 kV acceleration EBL system down to 80nm. Smaller than 80 nm design, PMMA no longer works as a good resist and the device mostly die during the etching process. The reason is the proximity effect as illustrated in Fig 2.3, *i.e.*, the phenomenon that the exposure dose distribution, and hence the developed pattern, is wider than the scanned pattern, due to the interactions of the primary beam electrons with the resist and substrate. These cause the resist outside the scanned pattern to receive

a non-zero dose. So, the two edges of the small exposed pattern is not as resistive to plasma etching as bigger ones. The following plasma etching will etches away both the patterned resist mask as well as the graphene underneath.

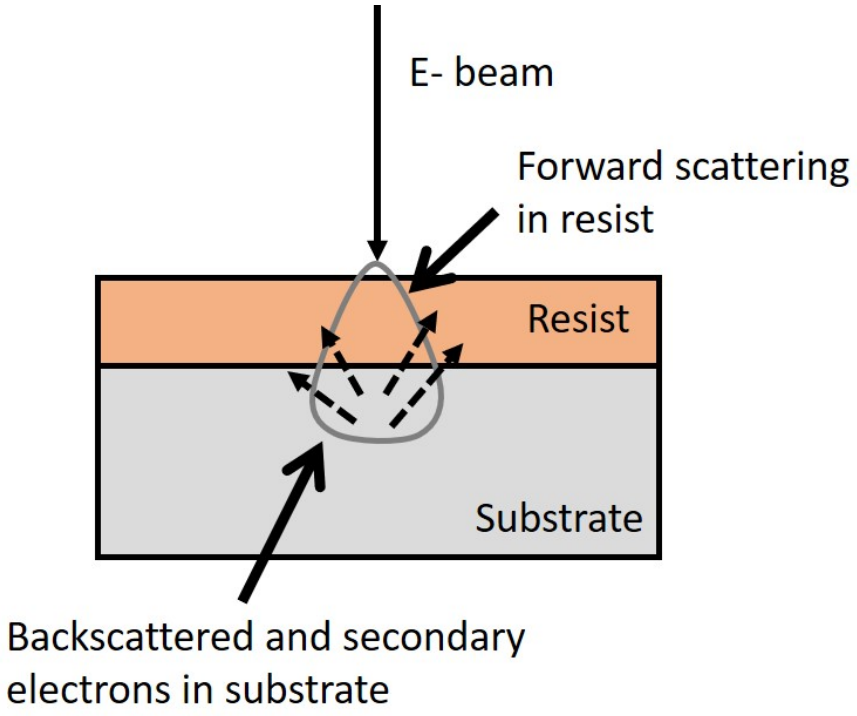

FIGURE 2.3: Schematic illustration of the e-beam proximity effect

To open a sufficient transport gap, the nanoribbon width has to be narrower than 40 nm. Such a high resolution could be achieved by 1) increasing the e-beam acceleration voltage which reduces the proximity effect, or 2) using other higher resolution resist. As the highest acceleration voltage in our system is 50 kV, I focused on the second approach. I have tested several kinds of resists to pattern small GNRs. Going through all these experience, here I would like to introduce three good resist for patterning small patterns, they are ARP 6200 positive resist, AR-N 7520 new negative resist, and hydrogen silsesquioxane (HSQ) resist.

2.2.1 Dose Tests for Hydrogen Silsesquioxane

We first introduce the negative e-beam resist hydrogen silsesquioxane (HSQ, XR-1541-002, Dow Corning), which has a fine resolution down to ∼20 nm. Its molecular structure is shown in Fig 2.4. When we apply e-beam to HSQ, its molecules crosslink, leading to the formation of amophaous silicon dioxide. Usually, the

companies will offer a very detailed recipe for users, which is generally good as reference. However, even small changes in instruments, *e.g.*, EBL work space, the acceleration voltage, *etc.*, can cause huge effects on the finally results. Therefore, when we start to use a new resist, it is necessary to do a serious process test on the fabrication parameters such as patterning mode (spot, line or area), beam spot pitch, e-beam dose and development time.

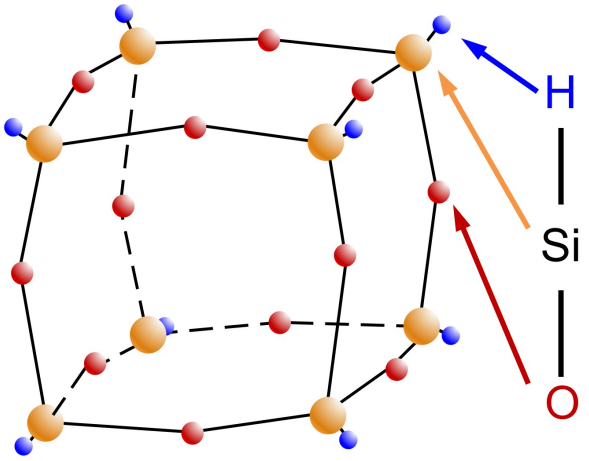

FIGURE 2.4: Molecular structure of hydrogen silsesquioxane

Electron beam dose has a definition of the total electrons that applied to the area, which can be described by equation:

$$Dose = \frac{I \times T}{A} \tag{2.1}$$

where I is the e-beam current, T is the writing time, A is the area. For example, when we use parameters as $I = 1000\,\text{pA}$, $T = 0.21\,\mu\text{S}$, to write patterns with a pitch of $10 \times 10\text{nm}^2$, the applied dose is $210\,\mu\text{C/cm}^2$. To change the e-beam dose, one can either change the e-beam emission current, or the exposure time of each spot. In general, $400 \sim 900\,\mu\text{C/cm}^2$ can be used to pattern $> 100\,\text{nm}$ structures. However, the suitable dose for $20\,\text{nm} \sim 40\,\text{nm}$ differs from the value that can be used for $> 100\,\text{nm}$ structures. So, we have to finer the area dose for each resist in our 50 kV EBL system. We tried to use different doses to pattern similar rectangles with widths varied from 5 to 50 nm with step of 2.5 nm, a same value to the spot pitch of the EBL system. We used two types of writing procedure, as represented in Fig2.5 Figure 2.6 displays the final results of the HSQ dose test that characterised by SEM imaging.

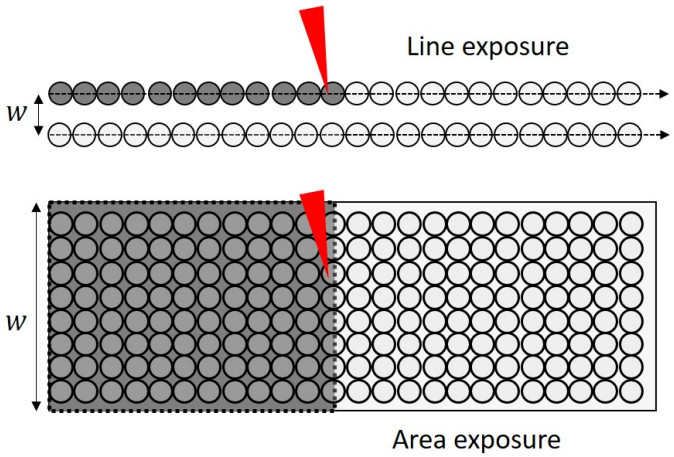

FIGURE 2.5: Illustration of line (up) and area (bottom) exposure schemes. The dots represent the spots that e-beam actually irradiates.

The line exposure is a e-beam writing scheme that only expose the two edges of the structure. Thanks to the proximity effect, the area between the edges will be also exposed. Using the line exposure scheme (group (a)), we could not obtain a proper line mask until we increased dose to 1800 µC/cm^2. The best resolution of $w =\sim 12$ nm is finally obtained. It might be larger than the designed structure $w = 5$ nm, but we are satisfy with it for our GNR devices. In addition, further increasing the dose simply over exposes the structure, leading to a much wider ribbon.

In comparison, area exposure is a scheme that letting the e-beam expose the entire structure. Using this scheme, we can only obtain a resolution of ~ 30 nm at a dose of 1200 µC/cm^2. Smaller structures can not be obtained using this scheme.

2.2.2 Dose Tests for AR-N 7520 new

AR-N 7520 new resist is a new negative resist of Allresist GmbH. This product is sensitive to e-beam and UV. A resolution compared to HSQ is expected. Unfortunately, The molecular structure of this resist is not open to public, we only know it is a kind of novolac, organic corsslinking agent.

Similarly, the dose test of AR-N 7520 new is performed through area exposure and line exposure schemes, and finally characterized via SEM and AFM imaging. For the area dose test, dose varied from 30 µC/cm^2 to 250 µC/cm^2 were used. In our system, we found the suitable dose is in a range from 60 µC/cm^2 to 120 µC/cm^2.

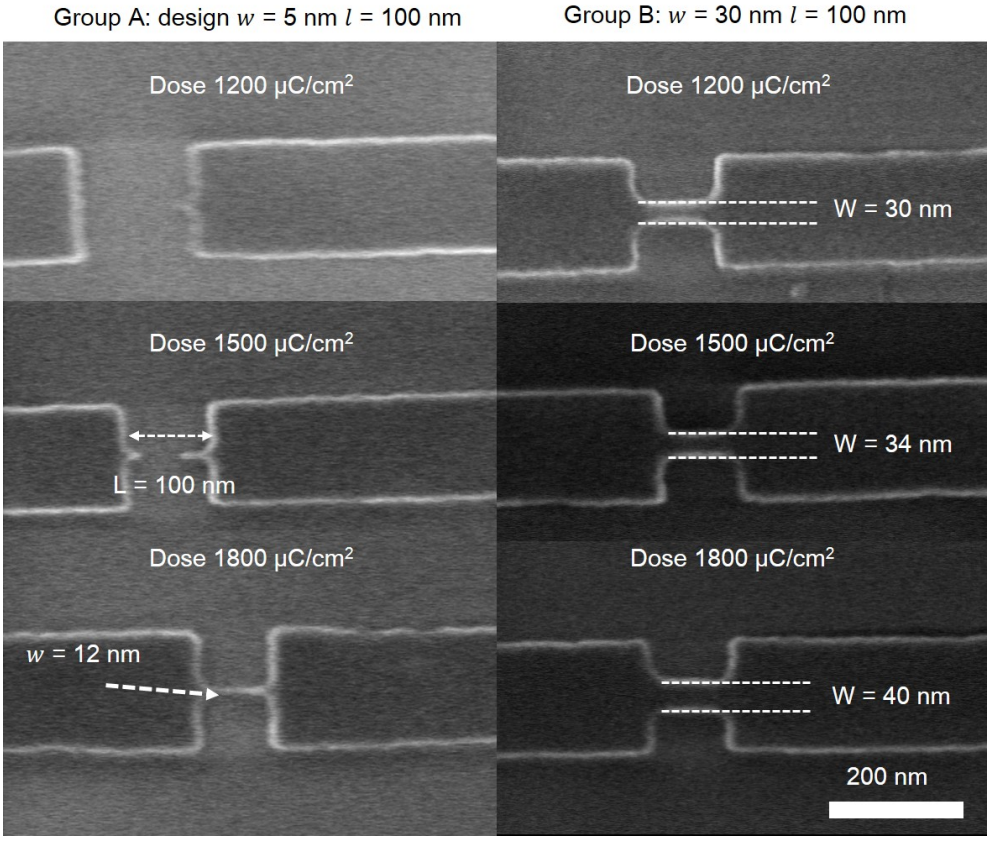

FIGURE 2.6: SEM images of two HSQ patterns exposed with different doses. (a) The design of the patterns is 5 nm-wide, 100 nm-long. (b) The design of the patterns is 30 nm-wide, 100 nm-long. The dot pitch setting is 2.5 nm

The best resolution using area exposure is 100 nm, far away from the expected resolution.

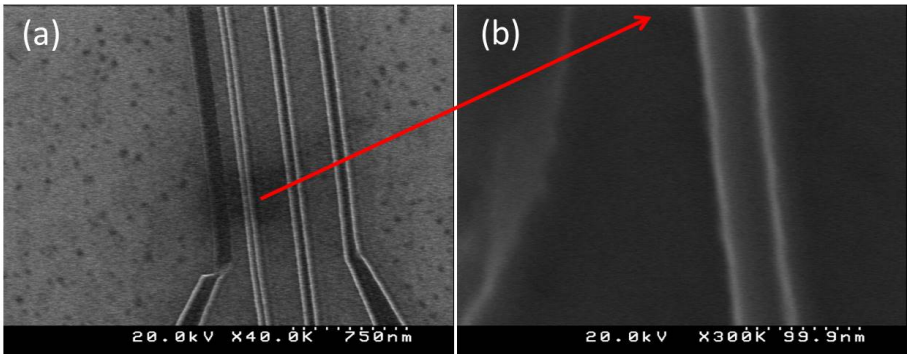

FIGURE 2.7: SEM images of AR-N 7520 new resist patterned structures. The red arrow highlights the best resolution ~45 nm ribbon structure.

For line exposure, the dose is varied from 120 μC/cm² to 1500 μC/cm² under a 1.25 nm dot pitch. The space between each lines are varied from 5 nm to 100 nm. After several dose test, we finally confirmed the best resolution is 45 nm under

a line exposure condition of 1000 µC/cm^2 with a line pitch of 10 nm. The SEM image is shown in Fig 2.7. it is reasonably good, but still not comparable to HSQ.

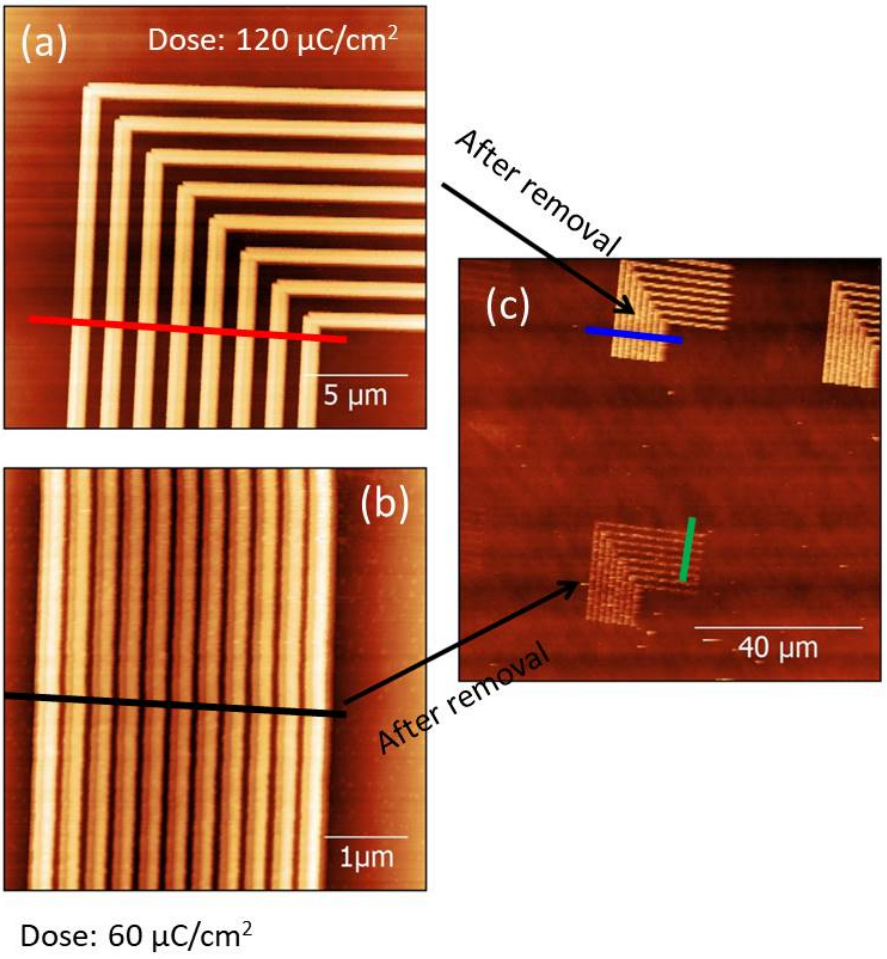

FIGURE 2.8: AFM characterization of the impacts of AR 300-76 remover on AR-N 7520 new structures. (a) AFM image of AR-N 7520 new resist pattern exposed with a dose of 120 µC/cm^2 and (b), exposed with 60 µC/cm^2. (c) AFM images of (a) and (b) after keeping the substrate in AR 300-76 remover for 90 mins.

To finer the resolution, I considered the utilization of the AR-300-76 Remover. As we know, the level of negative resist molecule cross-link depends on the e-beam dose. Line exposed structures usually have a very higher level of cross-link in their centre compared to edges because of the extremely large dose. While the removal can only removes the low dose exposed patterns as we see in Fig 2.8 and 2.9. In addition, since the AR-N 7520 new resist is a kind of organic crosslinking agent, plasma etching and H_2/Ar thermal annealing should be able to the low-level crosslinked parts, *i.e.* pattern edges, as well. Indeed, after a oxygen plasma etching at a pressure of 2.6 pa, 30 W RF power, we see the drastic change

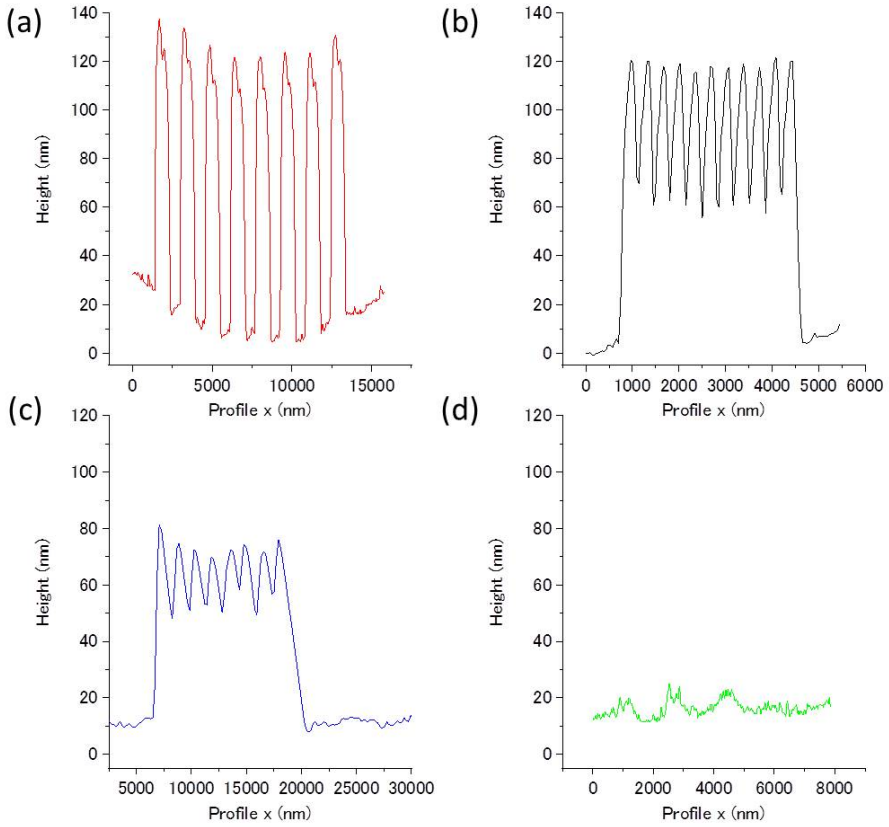

FIGURE 2.9: Height distribution of the line profiles in 2.8. (a) 120 µC/cm^2 and (b) 60 µC/cm^{2}e-beam dose exposed patterns before removal. (c) and (d) are the height distribution line profile of (a) and (b) after removal

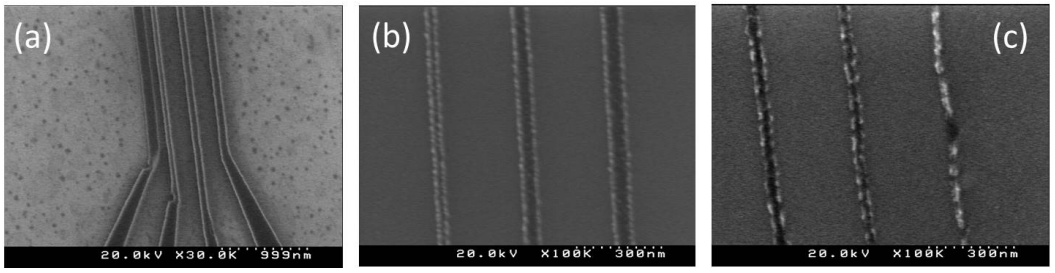

FIGURE 2.10: SEM image of line exposure patterned AR-N structures (1500 µC/cm^2) after (a) chemical removal, then (b) after gental oxygen plasma etching, and (c) after thermal annealing at 300°C in 1:9 H_2/Ar three hours.

at the patterned structures edge as shown in Fig 2.10 (a) to (b). The widths of each pattern reduced by $\sim$ 7 nm at both sides after plasma etching. After thermal annealing, the patterns become even smaller minimum down to $\sim$ 20 nm. However, after above etching and annealing, we see the pattern edges becomes rougher than before. This is because the exposure lines are not perfectively align during the writing procedure, which is regarded as a system disorder in a scale of a few nanometer. With the improvement of system engineering, this limitation

can be overcame in the near future.

2.2.3 Dose Test for AR-P 6200

Unlike the previous two resist, the AR-P 6200 resist is a high resolution positive resist. In my work, this resist is mainly used for the fabrication of side gate electrodes (see chapter 5). I did a serious does test on i) pattern width ($\sim 60\,\text{nm}$) and ii) adjacent patterns space ($\sim$ 50nm) using AR-P 6200.09 resist. After the patterning, I evaporated 50 nm Au with 5 nm Cr underneath to the sample followed by a lift-off so we can directly characterize the patterned "electrodes".

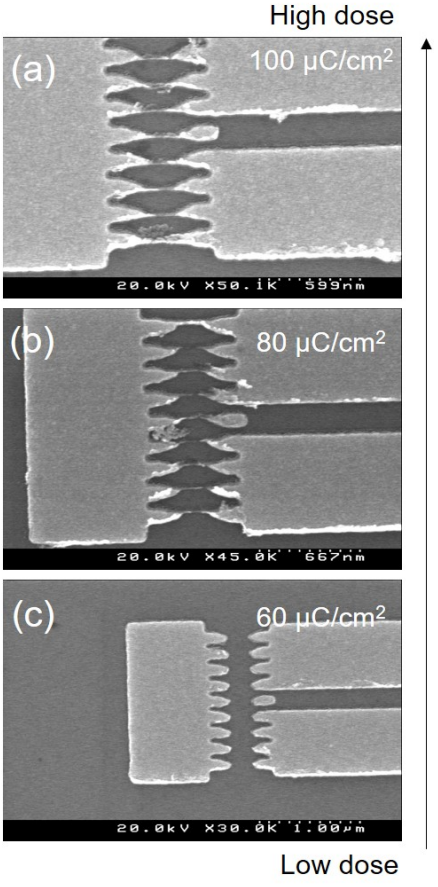

FIGURE 2.11: SEM images of a serious of metal fingers fabricated using AR-P 6200.06 resist with different e-beam exposure dose, (a) $120\,\mu\text{C/cm}^2$, (b) $190\,\mu\text{C/cm}^2$ and (c) $30\,\mu\text{C/cm}^2$

For this resist, I only checked the area dose. The recommended dose is $65\,\mu\text{C/cm}^2$ using a Raith Pioneer 30 kV EBL system with a e-beam spot pitch of 1.27 nm. In our system, we have an accelerate voltage of 50 kV and a spot pith of 1.25 nm. However, the suitable dose in our system is found to be $90\,\mu\text{C/cm}^2$ to $110\,\mu\text{C/cm}^2$.

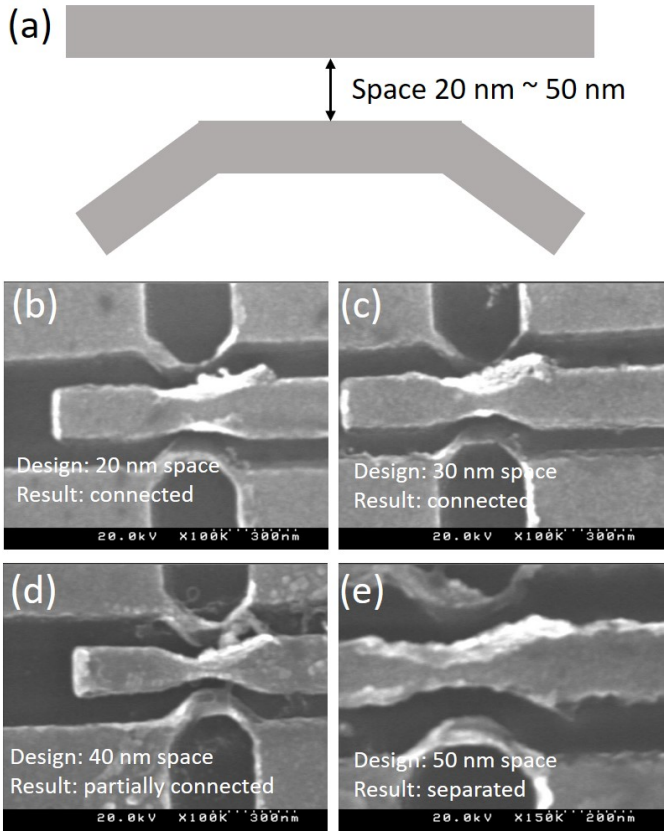

FIGURE 2.12: SEM images of metal structures with different spaces between each other. (a) and (b)

The recommended dose seems to be too low for 50 nm metal finger structures. Figure 2.11 is the SEM image of metal fingers fabricated using AR-P 6200.09 resist. Initially, we varied the dose from 40 $\mu C/cm^2$ to 250 $\mu C/cm^2$. For the sake of discussion, I only show three of them. Using a dose of 100 $\mu C/cm^2$, centre nanofingers are properly fabricated, Reducing the dose to 80 $\mu C/cm^2$, centre nanofingers can be fabricated, but they are thinner than the designed geometry, also the edges become rougher, suggesting the applied dose is not efficient to properly expose the structures. Further reduces the dose to 60 $\mu C/cm^2$, we can not see any structures after metal evaporation and lift-off.

After the dose determination, we move to investigate the minimum space in between the metal structures. If the designed two structures are too close, or the dose is too high, the real structure may connect due to the proximity effect. For this, we fabricated another serious of metal patterns with varied spaces between two adjacent patterns using the determined exposure dose. The spaces between two metal structures are from 20 *nm* to 50 nm. The results are shown in Fig 2.12. We see the fabricated structures will connect to each other until we increased the

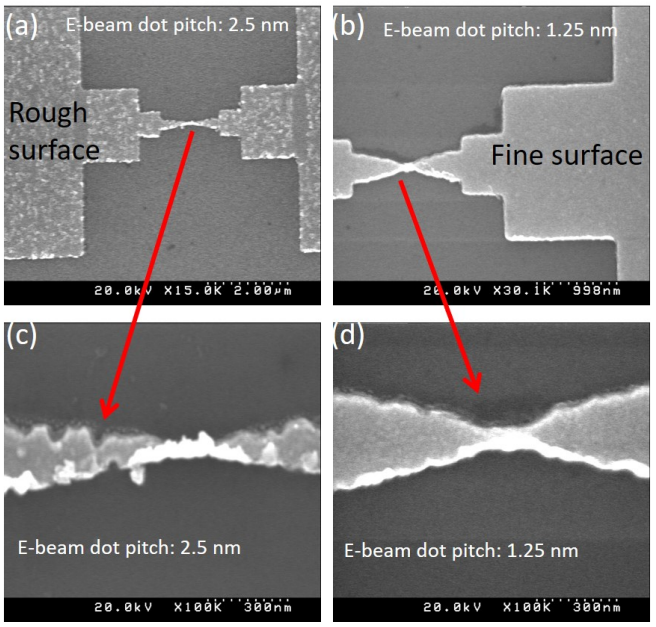

FIGURE 2.13: Comparison of metal surface fabricated using (a) 2.5 nm and (b) 1.25/,nm dot pitch. (c) and (d) are the zoom up of (a) and (b).

space between adjacent between structures to > 40/,nm in design, which fits our requirement well.

In addition, we also found the e-beam dot pitch also has an impact on the structures. We present a comparison of metal fingers wrote with the same dose but different e-beam dot pitches, *i.e.*, 2.5 nm and 1.27 nm, respectively in Fig 2.13 We noted is a bigger e-beam dot pitch leads to a rougher metal surface even the same dose.

2.3 Measurement Setup

Electrical characterization is carried out in a customized high vacuum prober station. This chamber has in total six arms, four arms for conventional voltage/current source and another two for RF probes. A Agilent B 1500 semiconductor analyser is used to sweep the voltages and current measurement. The sample stage is placed on the top of a dry helium cooling line. A heater is embedded under the sample state and connected to a Cryo-con model 22C temperature controller. With this set up, we can control the stage temperature from 5 K to 300 K. The whole measurement system is shown in Fig 2.14.

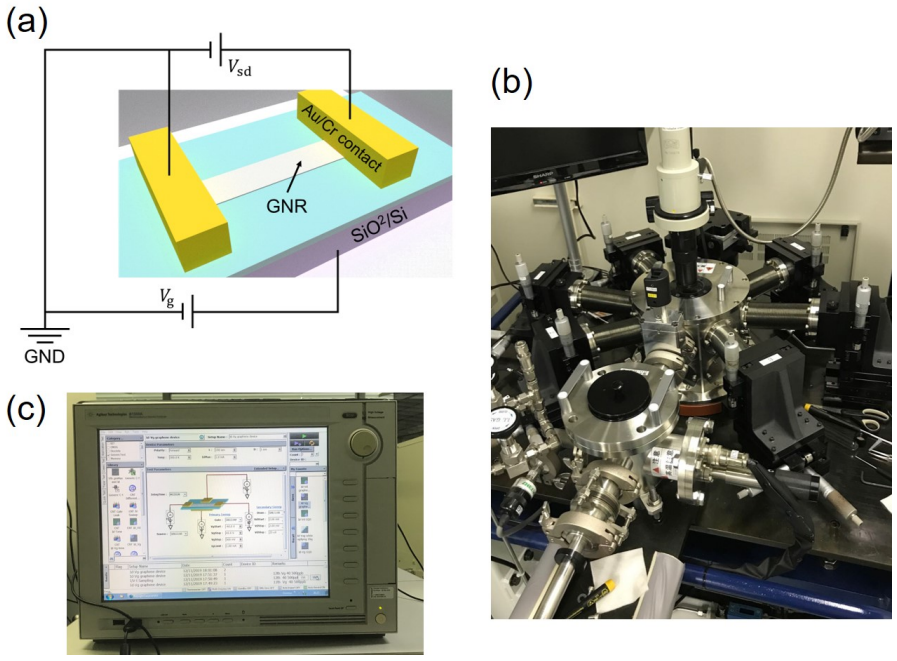

FIGURE 2.14: (a) Illustration of the measurement set up. (b) Customized high vacuum prober station and (c) Agilent B 1500 semiconductor analyser used for electrical characterization.

2.4 Summary

In this chapter, we introduced dose test experiments of three different high resolution e-beam resist. We see even the e-beam dose only can cause a huge difference on the final structures. These results are significant for the later fine GNR fabrication. Moreover, the experience on e-beam lithography patterning also contributes to the main topic, doping control as e-beam can be used to generate doping atoms from HSQ to graphene, which will be introduced in detail in chapter four.

Bibliography

[1] Ferrari, A.C.; Meyer, J.C.; Scardaci, V.; Casiraghi, C.; Lazzeri, M.; Mauri, F.; Piscanec, S.; Jiang, D.; Novoselov, K.S.; Roth, S.; Geim, A.K. Raman Spectrum of Graphene and Graphene Layers. *Phys. Rev. Lett.* **2006** *97* 187401.

Chapter 3

Doping Control in HSQ capped Graphene Nanoribbon

In chapter one, we briefly introduced the impacts of inhomogeneity doping and edge roughness induced *transportgap* in graphene nanoribbons. To realize energy band structure control in GNRs, we proposed a doping control strategy. First parts of this work is the experiments on the **doping level control**.

In this chapter, we will discuss the doping in graphene phenomenologically. First is the mechanism of different types of doping. Then we demonstrate a new method to dope GNR after device fabrication with visible controllability, *i.e.*, current annealing. The method allow us to aggressively tune the Fermi energy to high carrier density region, *e.g.*, the sub-band of bilayer GNR. In addition, the observation of localization states and the electrical tuning is included in the last.

3.1 Impact of Doping on Graphene FET Ambipolar Characteristics

Doping is a efficient approach in terms of band structure engineering from material aspects. Doping in graphene can be achieved by direct synthesis or a number of post treatments such as dip coating dopant containing solutions,[1] thermal annealing in a dopant ions irradiation fluence,[2] plasma treatment with special gases,[3] and electrostatic doping.

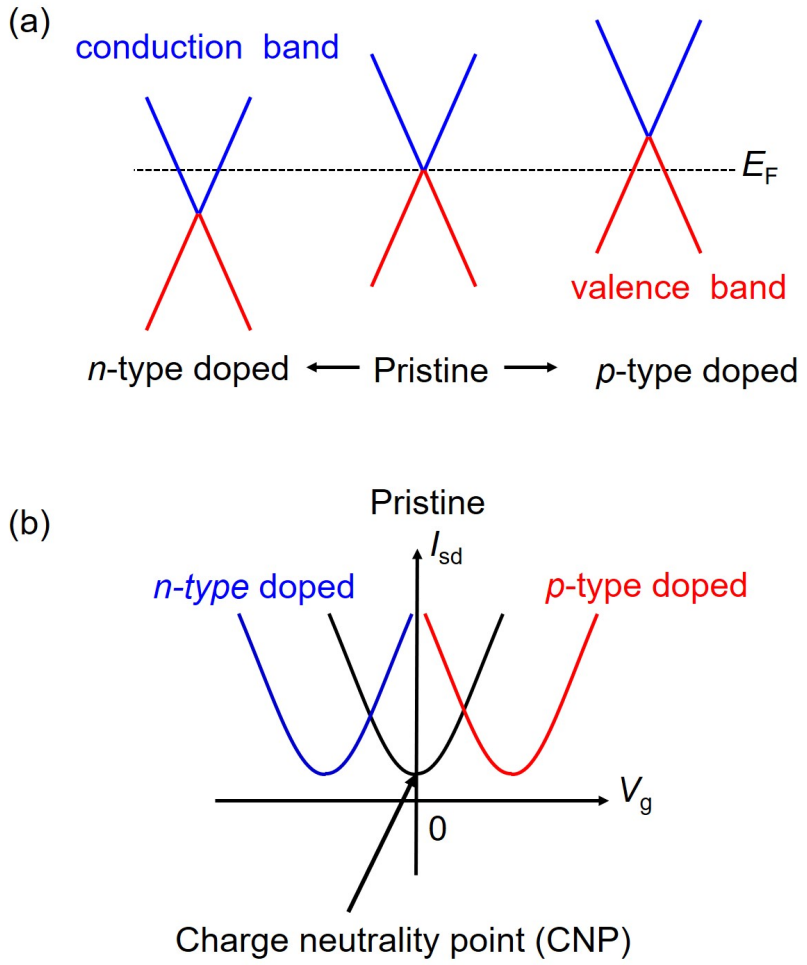

FIGURE 3.1: Impact of doping on (a) Fermi energy shift and (b) I_{sd}-V_g ambipolar characteristic

In general, the dip coating method is surface charge transfer doping method, *i. e.*, electron from graphene to dopant (p-type doping), or oppositely from dopant to graphene (n-type doping).[4] The chemical composite of graphene will not changed by this method. The doping effect on graphene is illustrated in Fig 3.1. When the device is n-type doped, the Fermi energy is shifted towards the conduction band thus the CNP in I_{sd}-V_g transfer curve measurement shifts negative V_g compared to pristine graphene. In the case of p-type doped, the Fermi energy is pushed to the valence band, resulting in a positive shift of CNP.

Apart from the electrical signature, charge transfer doping also causes a blue shift of the G band in its Raman spectra. Compared to that, plasma treatment induced doping usually cause a spliting of G band apart from the bule shift. This is becuase charge trasfer doping method won't introduce point defect, while the plasma treatment does, resulting strong defect D-peak in Raman spectra.[5] This

technique provides an experimental approaches to identify the charge transfer doping from other doping mechanism. Because the charge transfer doping doesn't change the lattice structure of graphene, the atomic bonds remains sp^2 after doping.

3.2 Control of Doping form HSQ to Graphene

3.2.1 Mechanism of Doping from HSQ to graphene

Initially, the e-beam resists will cause a certain type charge transfer doping to graphene. For example, PMMA usually cause *p*-type doping. This is determined by the chemical composite of the resist. In comparison, HSQ may cause both *n* and *p*-types. According to Brenner *etal*, this is because of the mismatch of Si-O and Si-H bond strength (8.95 eV for Si-O and 4.08 eV for Si-H).[8, 29] The cross-linking of HSQ molecule occurs when it is exposed to *e.g.*, high temperature annealing, e-beam irradiation, plasma, *etc.* When these energies relatively weak, the cross-link of HSQ molecule is in a low order, *i.e.*, Si-H bonds are readily break providing hydrogen to graphene while Si-O bonds maintains, unless we increased the energy power, or wait sufficiently long. Importantly, it has been demonstrated that hydrogen adsorption leads to *n*-type doing in graphene while water (H_2O) and oxygen lead to *p*-type doping. In another word, doping types and level control can be expected using HSQ by cleaving its molecule bonds.

3.2.2 Generating Doping from HSQ via Current Annealing

Now we introuduce our new strategy to dope graphene, *i.e.*. current annealing. By applying a massive current to graphene, Joule heat will be generated.[6] To roughly estimate the current annealing effect in intrinsic graphene, we alspo proformed finite simulation using COMSOL Mupliphysics. Figure 3.2 is the finite element simulation results of current annealing induced Joule heat in suspended graphene nanoribbon. When a current density of 1×10^8 A/cm^2 is applied, the temperature of the centre part of the suspended GNR is as high as$>$ 1000°C. Experimentally, Moser *etal* reported that the generated Joule heat in graphene on silicon dioxide substrated is $>$ 600 °C.[6] According to another experimental on the chemical

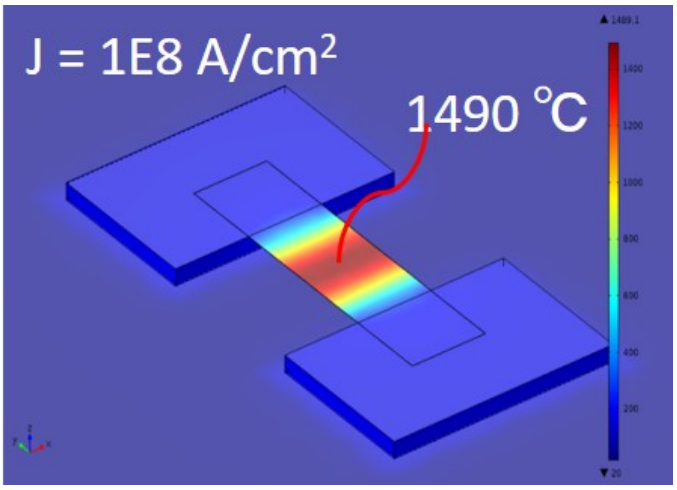

FIGURE 3.2: Finite simulation result of current annealing. The applied current density is 1×10^8 A/cm^2

component change in HSQ, Si-O bonds will be readily broken at such a high temperature.[29].

After the simulation, we then confirmed this hyposisy experimentally. A graphene FET device is fabricated as introduced in chapter 1 without patterning. Then HSQ is span on the graphene and patterned into a rectangle using e-beam exposure lithography as the optical image shown in Fig 3.2. In addition, the dose used in HSQ patterning is 1200 µC/cm^2 which normally results in week p-type doping in graphene (in chapter 4 we will discuss the e-beam dose dependent doping control in detail). Thereafter, current annealing is carried out in the high vacuum probe station. A bias voltage is applied to the electrode pads and slowly ramped up to 8 V without any back side voltage gating. This source-drain current was recorded and plotted in Fig 3.4 (a). Current barely changed at the beginning. After one hour, we see current drops with time to a certain value at $T = 2$ hours. In the next two hours, the current fluctuates without significant changes. Until $T > 4$ hours, current increased again. The overall current change is only 5%, but it has a significant effect on graphene doping as the ambipolar characteristic shown in Fig 3.4 (b).

At the beginning, the ambipolar is observed and a CNP was found at $V_g = 10$ V (black line), the initial doping is p-type. After roughly one hour, CNP start to shift from positive gate voltage region to negative region, indicating the doping in graphene transformed from p-type to n-type. Further annealing didn't shift the CNP more negatively, instead, it shifts the CNP backward to the positive V_g region. Finally, the CNP is found at $V_g = 13$ V.

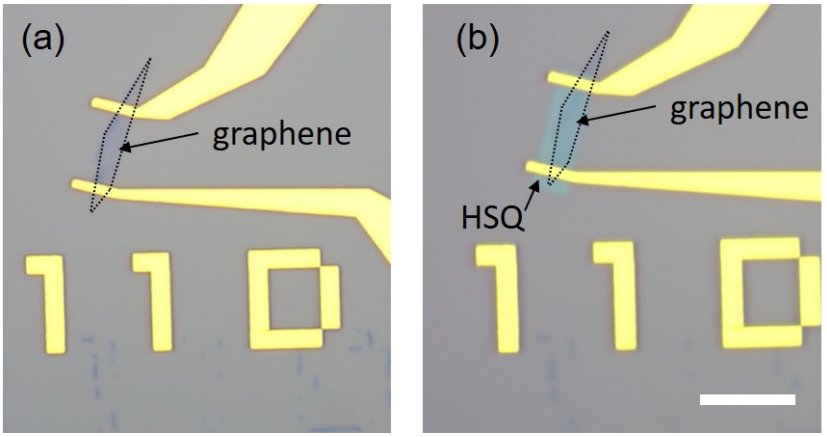

FIGURE 3.3: The graphene FET used for current annealing experiment (a) before and (b) after HSQ coating. The scale bar is 10 *mu*m

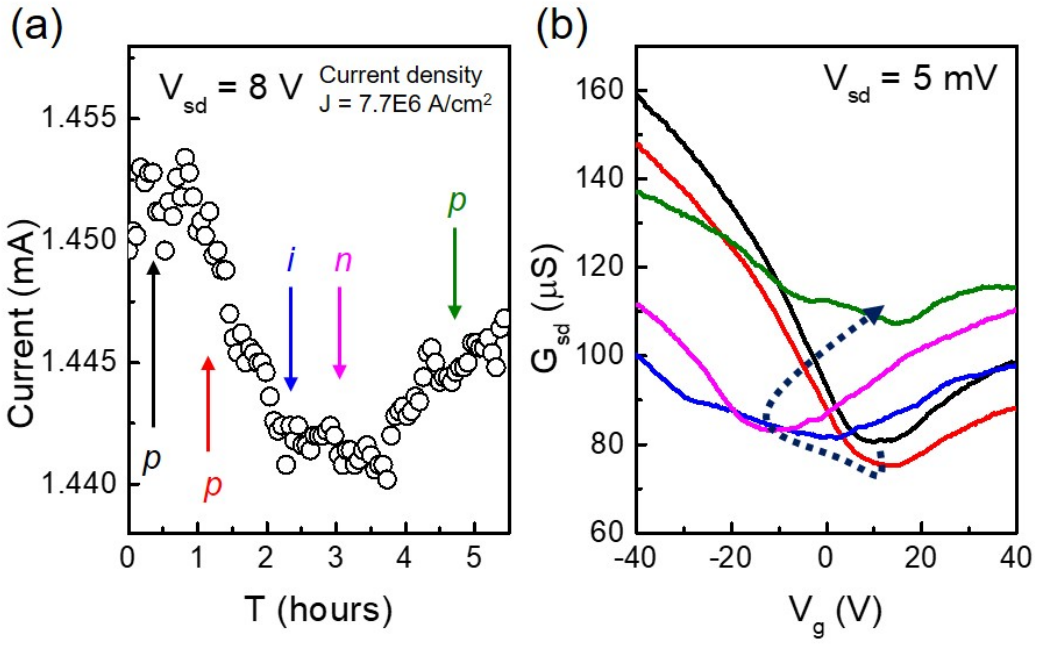

FIGURE 3.4: Current annealing results of the HSQ capped graphene FET shown in 3.3. (a) Recorded current change at a fixed bias voltage. During the process, ambipolar characteristic is measured as the color lines denoted. (b) The evolution of ambipolar during current annealing process. Dashed line highlights the pattern of CNP shift.

Going through above experiment observation, we clearly see the doping in graphene changed from p to n, and then reversely from n to p. This behaviour can be explained as following. When the current annealing started, the Joule heat readily cleaves the Si-H bonds. Generated hydrogen atoms leads to reduced p-type doping and increased n-type doping nature. After a certain time, Si-H bonds are almost completely cleaved, then Si-O start to break, generates oxygen to graphene leading to the increase of p-type doping.[8, 29]

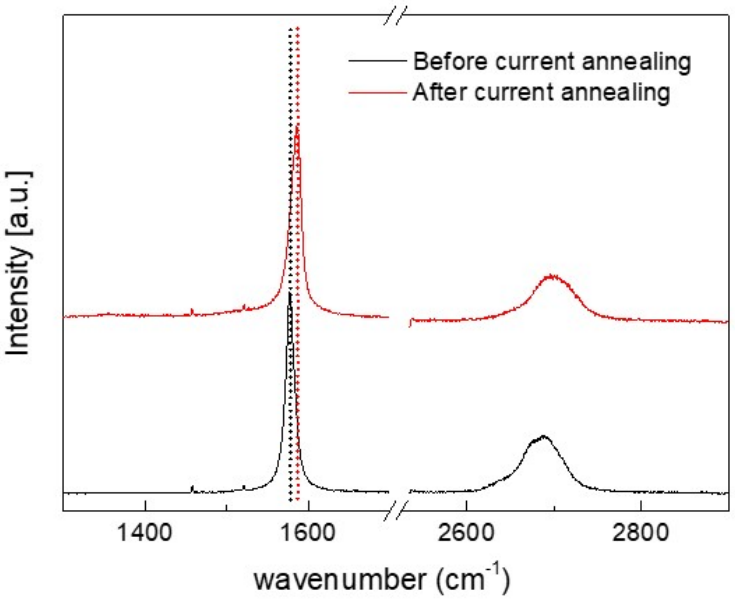

FIGURE 3.5: Raman spectra of the graphene FET shown in Fig 3.3 (b). (a) Before current annealing. (b) After current annealing.

During the experiment, we considered the possible chemical reaction between graphene and dopant atoms that may lead to the formation of C-H and C-O bonds. This can be confirmed by characterizing the D and D' band in doped graphene Ramam spectra that stemmed from lattice defects. Figure 3.5 is the Raman spectra before and after current annealing doping. Only a blue shift of G band from 1577 cm^{-1} to 1585 cm^{-1} is noted without the appearance of D or D' band, indicates the lattice structure of graphen underneath is not changed significantly. According to the Raman measurement results, we believe charge transfer doping is most likely to happen in the case of our current annealing doping technique.

3.3 Utilization of HSQ Doping in Fermi Energy Tuning

This method can be utilized to tune the Fermi energy in a bilayer graphene nanoribbon after fabrication. In comparison to monolayer graphene, bilayer graphene is of interest due to its unique band-related properties, *e.g.* parabolic band

structure,[18, 19] electric-field induced band gap,[20] multiple sub-bands transport and inter-band scattering.[21, 22] More importantly, it offers a great opportunity to investigate multiband transport phenomena (3.6). However, accessing to its higher sub-band by applying external electric field is challenging, special dielectrics or ionic liquid gate are normally required. [21, 22] So far, the tranport with localized states have only been investigated for the lowest sub-band in bilayer GNRs.[23].

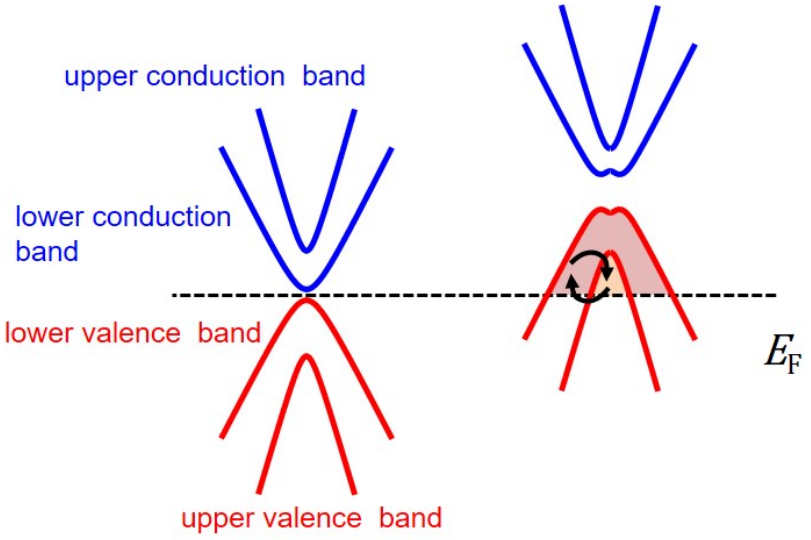

FIGURE 3.6: Schematic illustration of the bilayer graphene band structure (left) and the inter sub-band scattering (right)

In this experiment, HSQ is spun and patterned into a 50 nm-wide, 200 nm-long nanoribbon (insert of Fig.3.7(a)), using electron-beam lithography. In the end, the shape of HSQ mask is transferred into bilayer graphene by O_2 plasma etching at a relatively low power of 20 W to avoid severe edge damage. [24] After fabrication, electrical measurements are performed in vacuum ($\sim 10^{-5}$ Pa) at 5 K using p-doped Si substrate as back-gate. Besides, one $\sim$ 20 nm-wide, 100 nm-long, monolayer GNR device is also fabricated following the same procedure and characterized for comparison.

The as-fabricated GNR capped by HSQ is normally weakly p-doped due to the weakly crosslinked HSQ, [8] and has its charge neutral point within 20 V gate voltage with the 300 nm SiO_2 dielectric. In order to tune E_F into the upper sub-valence band for bilayer GNR, which locates at much higher energy from the lower sub-band, we apply current annealing to the device to introduce doping. The bias voltage is slowly ramped up to the value where current passing through the device is about $\sim 500\,\mu A/\mu m$. The bias voltage then is fixed and continuously applied

to the device until a saturation in current is observed. The joule heating can generate the temperature as high as > 1000 °C, [25] which is enough to break the Si-O bonds in HSQ [26] but leave the graphene structurally intact.[6] Consequently, it produces oxygen atoms, the heavy p-dopant to graphene, and therefore shifting the E_F towards higher energy, *i.e.* the upper sub-valence band. The annealing is repeated until the desired doping level is obtained, which is verified by measuring the field effect.

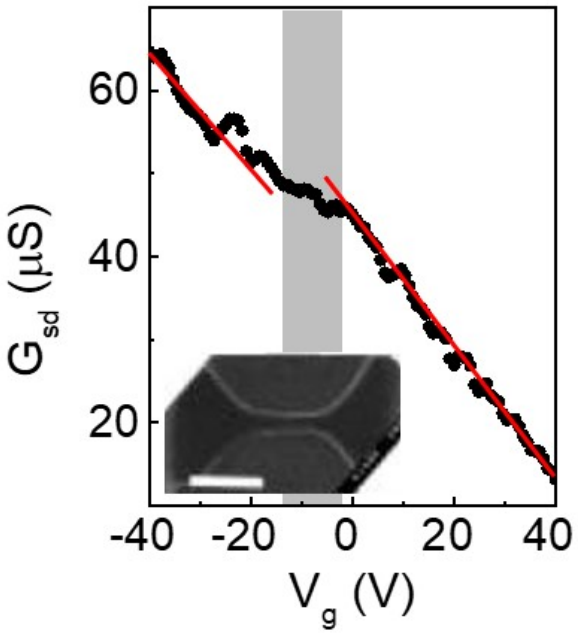

FIGURE 3.7: Gate modulation of differential conductance G_{sd} in bilayer GNR measured at 5 K with dc bias of 1 mV (black dots), The red solid lines are the eye guide. The inset shows the scanning electron microscope image of the measured device. Scale bar: 200 nm

Figure 3.7 plots the conductance G_{sd} as a function of gate voltage V_g measured in the bilayer graphene after current annealing. As V_g decreasing nagatively, G_{sd} increases with visible oscillations. Charge neutral point does not occur within 40 V, as one evidence of the heavily p-doped characteristics. More interestingly, a kink with a pronounced shift of G_{sd} by -10% is noted around -5 V. It is a signature of a different sub-band being populated, as the opening of an additional inter-band scattering causes the reduction of conductivity.[21, 22] In the case of a bilayer GNR, it suggests that Fermi energy enters a higher sub-band. As reported previously, the energy difference between upper and lower sub-valence band ΔE is about $400 \sim 600$ meV.[21] This energy can be translated into a back gate voltage V_g using the equation,[27]

$$\Delta E = \pi\hbar^2 C_g^* \left|V_g - V_{cnp}\right| / 2em^*, \tag{3.1}$$

where $m^* \approx 0.1m_e$ is the effective mass of hole with m_e being free electron mass,[28] V_{cnp} is the location of charge neutral point, C_g^* is the unified gate capacitance. Due to the small size of GNR, the fringe capacitance has to be considered when estimating C_g^*. However, it is difficult to calculate the total capacitance accurately using a simple model. Hence, we obtain the value of C_g^* by performing a finite element simulation using COMSOL Multiphysics. Considering a 300 nm-thick SiO_2 dielectric and 60 nm-thick capping HSQ, the simulation suggests a C_g^* of $3.03 \times 10^{11}\ |e|/\text{V}\cdot\text{cm}^2$ for this specific device. The doping level of $4.9 \times 10^{13}\ \text{cm}^{-2}$ can also be estimated by using $n = C_g^* \left|V_g - V_{cnp}\right| / e$, showing a good agreement with previously reported carrier concentration in the upper subband of a bilayer graphene.[21] With ΔE of 600 meV, we estimate $|V_g - V_{cnp}| \approx 165$ V, which suggests that the charge neutral point locates around 160 V. In case of a HSQ capped device without annealing, a high gate voltage of ~ -150 V is necessary to tune E_F into the upper sub-valence band, which is highly possible to damage graphene electrostatically or even breakdown SiO_2.[29]

3.4 Observation of Localization States in the Sub-Band of Heavily Doped Bilayer GNR

To understand the origin of the oscillations in Fig 3.7, $\mathrm{d}G_{sd}/\mathrm{d}V_g$ is plotted for varied gate voltage and source-drain bias, the so-called charge stability diagram. The result is plotted in Fig. 3.8(a). At gate voltage $V_g < 10$ V, highly merged Coulomb diamond-like patterns are observed with barely distinguished boundaries. At $V_g > 10$ V, the patterns start to exhibit a certain period with clearer boundaries (Fig. 3.8(b)).

Due to localized states, the energy band fluctuates spatially in GNR. A schematic energy band diagram can be illustrated as Fig. 3.9(a). When the E_F is completely in the upper sub-valence band (at very large negative gate voltage, not reached in our measurement), holes in both lower and upper sub-bands diffuse through the channel. As gate voltage increases positively (III), E_F touches the fluctuating bottom of upper sub-band, and the merged charge puddles are created. With

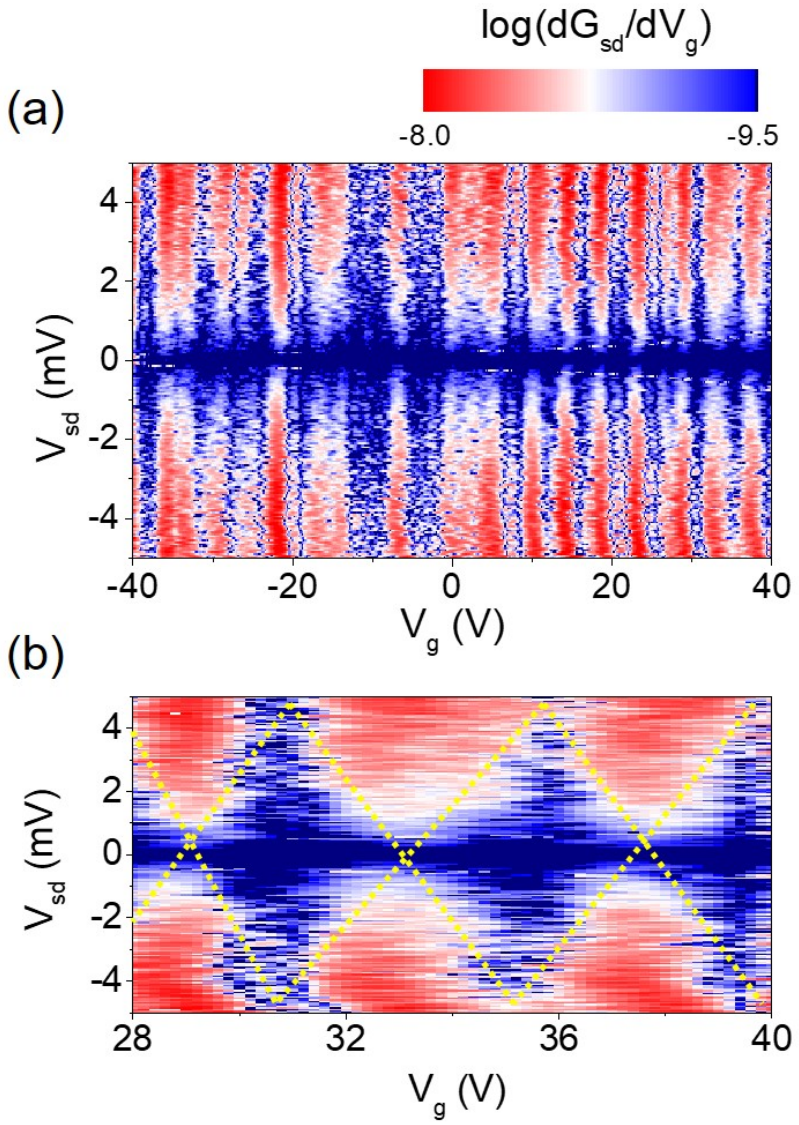

FIGURE 3.8: (a) dG_{sd}/dV_g as a function of both bias voltage V_{sd} and back-gate voltage V_g from -40 to 40 V measured in the bilayer GNR shown in 3.7. (b) The zoomed-in details of (b) between 28 to 40 V, the yellow dashes are the eye guide to the diamond-like features. (d) schematic energy band diagram of bilayer graphene with localized charge states. The illustrated three states, I, II, and III, are marked accordingly in (b).

increasing gate voltage, the merged charge puddles start to separate to act as "quantum dots" and puddle size shrinks. Under the circumstances, holes in the upper sub-band can tunnel through these "dots", resulting in the highly merged Coulomb diamond-features in the transport measurement. Noted, the transport of carriers in the lower sub-band is still diffusive. It is the reason the overall conductance of the channel is considerably high. When E_F crosses a certain nominal energy in the fluctuating bottom of upper sub-band (II), the upper sub-band is

mostly pinched off. Subsequently, the inter-band scattering closes and conductance rises, corresponding to the measured conductance kink in Fig. 3.7. With Further increased gate voltage (I), E_F is almost in the lower sub-valence band, leaving only few deepest charge puddles in the upper sub-band.

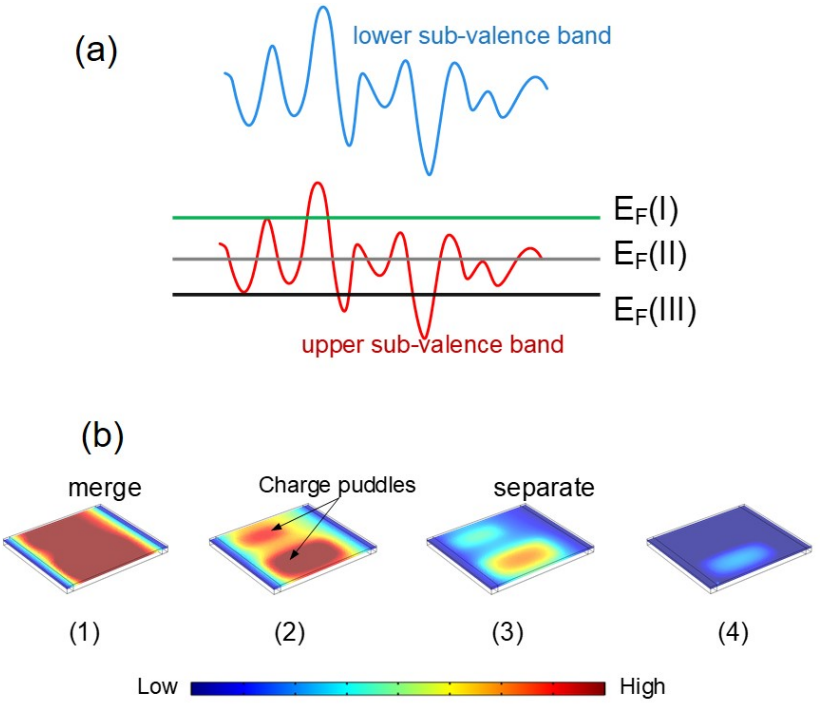

FIGURE 3.9: (a) schematic energy band diagram of bilayer graphene with localized charge states. The illustrated three states, I, II, and III, are marked accordingly in Fig 3.8(b). (b) Finite element simulation of the evolution of two charge puddles with gate voltage. Color bar denotes the hole density. From (1) to (4), the gate voltage is increased positively. (1) At very large negative gate voltage, E_F is far inside the upper sub-valence band, diffusive transport dominates. (2) two charge puddles start to separate, where the quantum-dots like transport appears. (3) they are isolated. (4) one puddle vanishes and only a single puddle remains, where the single dot dominated transport is expected.

To provide a visualized image, we simulate the evolution of charge puddles in GNR subject to the gate voltage tuning using finite element method (COMSOL Multiphysics). Two adjacent doping centers with different concentrations are induced in a thin conductor, to simulate two merged charge puddles with varied potential fluctuations in graphene. When a gate voltage is applied, the merged charge puddle separates into two isolated ones, and eventually evolves into a single puddle at higher gate voltage, as illustrated in Fig. 3.9(b).

Furthermore, with the periodic oscillations data (Fig.3.8(b)), we are able to estimate the nominal size of the charge puddles. The spacing between diamonds

is read as $\Delta V_g \sim 4.5$ V, giving an effective gate capacitance $C_g = e/\Delta V_g = 0.035$ aF.[30] Then, the nominal diameter of charge puddles is extracted as 19 nm, using the equation $d_{eff} = 2\sqrt{tC_g/\pi\varepsilon\varepsilon_0}$, with $t = 300$ nm being thickness of SiO_2, ε and ε_0 being the relative permittivity of the surrounding dielectric and vaccum permittivity, respectively. This agrees with the directly measured values by scanning tunnelling microscope.[12, 14]

3.5 Localization States Close to CNP of Weakly Doped Monolayer GNR

Lastly, we characterize a monolayer GNR device without annealing for comparison. Figure 3.10 displays the measured gate modulation of G_{sd}. At -2.5 V $< V_g <$ 25.0 V, dG_{sd} is strongly suppressed, known as the transport gap. The center of the gap is misaligned from 0 V, implying slightly p-doped graphene by the cross-linked HSQ. Inside the gap, oscillations are clearly noted.

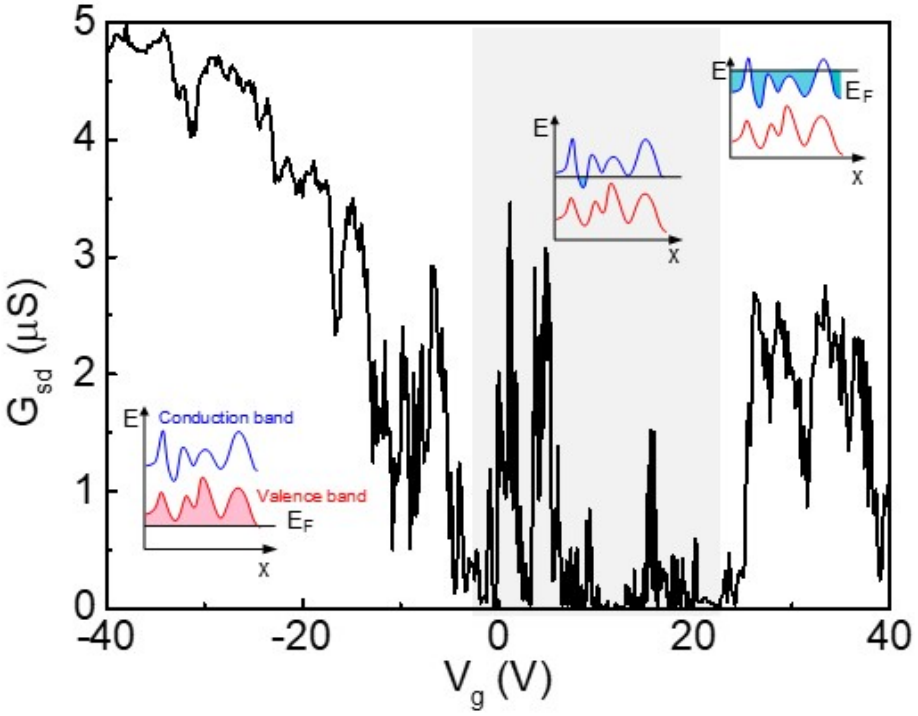

FIGURE 3.10: (a)Gate modulation measured in a monolayer GNR with 5 mV dc bias. The transport gap is shadowed. Insets are the schematic energy band diagram considering the localized charge states.

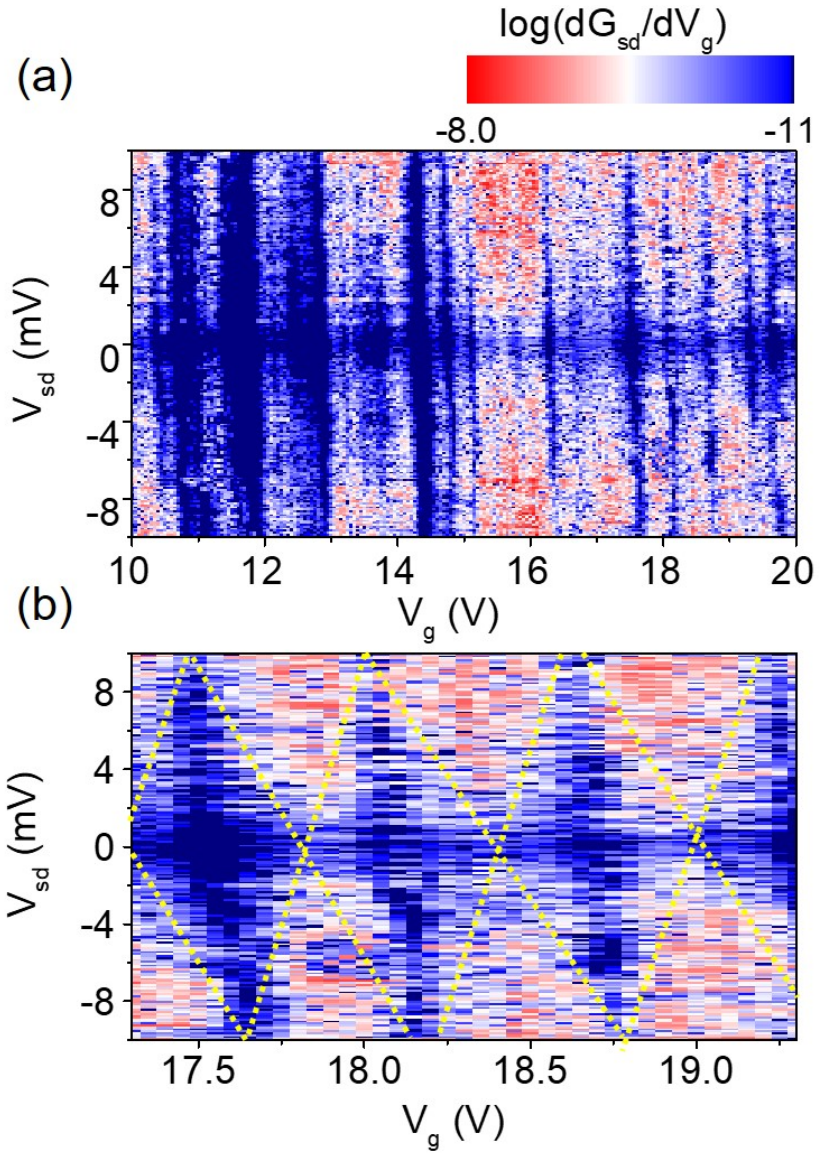

FIGURE 3.11: (a) Charge stability diagram of measured inside the transport gap. (b) The zoomed-in detail of (b) showing the periodic Coulomb diamond-like patterns. The yellow dashes are the eye guide to the perimeters of the Coulomb diamonds.

Figure 3.11(a) shows the charge stability diagram measured inside the gap from 10 V to 20 V. Similar to the bilayer GNR, at 10 V $< V_g <$ 15 V, firstly merged Coulomb diamond-patterns are observed, originated from the tunnelling via a large number of charge puddles. At V_g larger than 17.5 V, periodic Coulomb diamonds with identifiable boundaries are observed, manifesting a few "quantum dots" dominated transport. The period is found to be $\Delta V_g \sim 0.75$ V, corresponding to an effective gate capacitance $C_g = e/\Delta V_g \sim 0.2$ aF. The nominal diameter of charge puddles d_{eff} is calculated to be 45 nm, showing a good agreement with the direct

observation using scanning tunneling microscopy [12, 14] and the extracted values from the transport measurements on monolayer graphene.[14–17]

The similar phenomenon has also been reported for a bilayer graphene with the lower sub-band conduction.[23] Compared to the bilayer GNR with multiple sub-bands, the size of charged puddles in the monolayer GNR is in the same order of magnitude but slightly larger, as possibly the charged puddles induced at the interface are more screened in the higher sub-bands. Moreover, the overall conductance is much lower than that of the aforementioned bilayer GNR with multiple sub-bands conduction, as the only possible transport mechanism is the tunnelling through isolated puddles. It is also possible to have both hole and electron puddles participate the transport in monolayer GNR, resulting in the more complex transport characteristics.

3.6 Summary

In this chapter, we discussed the charge transfer doping phenomenologically. Then we demonstrated a simple current annealing approach to generate doping element from HSQ capping layer. The Raman characterization indicates the doping we observed is stemmed from hydrogen/oxygen adsorption *i.e.*, charge transfer doping. Utilizing this method, accessing of sub-band in bilayer GNR is achieved. The spatial fluctuation of the localized states in GNR is tunable by applying external electric filed. As the results, we observed few quantum dots-like transport behavior. In the future, the detailed physics of the higher sub-band tunneling and inter-band scattering is worthy of thorough investigation.

Bibliography

[1] Zhao, W.; Tan, P.; Zhang, J.; Liu, J. Charge Transfer and Optical Phonon Mixing in Few-Layer Graphene Chemically Doped with Sulfuric Acid. *Phys. Rev. B* **2010** *82*, 245423.

[2] Guo, B.; Liu, Q.; Chen, E.; Zhu, H.; Fang, L.; Gong, J.R. Controllable N-Doping of Graphene. *Nano lett.* **2010** *10*, 4975-4980.

[3] Lin, Y.C.; Lin, C.Y.; Chiu, P.W. Controllable Graphene N-doping with Ammonia Plasma. *Appl. Phys. Lett.* **2010** *96*, 133110.

[4] Liu, H.; Liu, Y.; Zhu, D. Chemical Doping of Graphene. *J. Mater. Chem* **2011** *21* 3335-3345.

[5] Jeong, H.M.; Lee, J.W.; Shin, W.H.; Choi, Y.J.; Shin, H.J.; Kang, J.K.; Choi, J.W. Nitrogen-Doped Graphene for High-Performance Ultracapacitors and the Importance of Nitrogen-Doped Sites at Basal Planes. *Nano lett.* **2011** *11*, 2472-2477.

[6] Moser, J.; Barreiro, A.; Bachtold, A. Current-Induced Cleaning of Graphene. *Appl. Phys. Lett.* **2007**, *91* 163513 (2007).

[7] Yang, C.C.; Chen, W.C. The Structures and Properties of Hydrogen Silsesquioxane (HSQ) Films Produced by Thermal Curing. *J. Mater. Chem* **2002,** *12,* 1138-1141.

[8] Brenner, K.; Murali, R. Single step, Complementary Doping of Graphene. *Appl. Phys. Lett.* **2010,** *96,* 063104.

[9] Han, M. Y.; Özyilmaz, B.; Zhang, Y.; Kim, P. Energy Band Engineering in Graphene Nanoribbon. Energy Band Engineering in Graphene Nanoribbon. *Phys. Rev. Lett.* **2007**, *98* 206805.

[10] Sols, F.; Guinea, F.; Castro Neto, A. H. Coulomb Blockade in Graphene Nanoribbons. Phys. Rev. Lett. **2007**, *99*, 166803.

[11] Xue, J.; Sanchez-Yamagishi, J.; Bulmash, D., Jacquod, P.; Deshpande, A.; Watanabe, K.; Taniguchi, T.; Jarillo-Herrero, P.; LeRoy, B. J. Scanning Tunnelling Microscopy and Spectroscopy of Ultra-Flat Graphene on Hexagonal Boron Nitride *Nat. Mater.* **2011**, *10* 282–285.

[12] Zhang, Y.; Brar, V. W.; Girit, C.; Zettl, A.; Crommie, M. F. Origin of Spatial Charge Inhomogeneity in Graphene. *Nat. Phys.* **2009**, *5* 722-726.

[13] Samaddar, S.; Yudhistira, I.; Adam, S.; Courtois, H.; Winkelmann, C.B. Charge Puddles in Graphene Near the Dirac Point. *Phys. Rev. Lett.* **2016,** *116,* 126804.

[14] Stampfer, C.; Güttinger, J.; Hellüller, S.; Molitor, F.; Ensslin, K.; Ihn, T. Energy Gaps in Etched Graphene Nanoribbons. *Phys. Rev. Lett.* **2009,** *102,* 056403.

[15] Todd, K.; Chou, H.T.; Amasha, S.; Goldhaber-Gordon, D. Quantum Dot Behavior in Graphene Nanoconstrictions. *Nano Lett.* **2009,** *9,* 416-421.

[16] Han, M.Y.; Brant, J.C.; Kim, P. Electron Transport in Disordered Graphene Nanoribbons. *Phys. Rev. Lett.* **2010,** *104,* 056801.

[17] Gallagher, P.; Todd, K.; Goldhaber-Gordon, D. Disorder-Induced Gap Behavior in Graphene Nanoribbons. *Phys. Rev. B* **2010,** *81,* 115409.

[18] McCann, E.; Abergel D. S. L.; Fal'ko, V. I. Electrons in Bilayer Graphene. *Solid State Commun.* **2007**, *143* 110-115.

[19] Ohta, T.; Bostwick, A.; Seyller, T.; Horn, K.; Rotenberg, E. Controlling the Electronic Structure of Bilayer Graphene. *Science* **2006**, *313* 5789, 951-954.

[20] Zhang, Y.; Tang, TT.; Girit, C.; Hao, Z.; Martin, MC.; Zettl, A.; Crommie, MF.; Shen, YR.; Wang, F. Direct Observation of a Widely Tunable Bandgap in Bilayer Graphene. *Nature* **2009**, *459* 820–823.

[21] Efetov, D. K.; Maher, P.; Glinskis, S.; Kim, P. Multiband Transport in Bilayer Graphene at High Carrier Densities. *Phys. Rev. B* **2011**, *84* 161412(R).

[22] Nagashio, K.; Kanayama, K.; Nishimura, T.; Toriumi, A. Carrier Response in Band Gap and Multiband Transport in Bilayer Graphene Under the Ultra-High Displacement. in *Electron Devices Meeting (IEDM), 2013 IEEE International*, IEEE, Washington, DC, USA, 9-11 December **2013**.

[23] Wang, M.; Song. EB.; Lee, S.; Tang, J.; Lang, M.; Zeng, C.; Xu, G.; Zhou, Y.; Wang, KL. Quantum Dot Behavior in Bilayer Graphene Nanoribbons. *ACS nano* **2011**, *5* 11, 8769-8773.

[24] Sun, J.; Iwasaki, T.; Muruganathan, M.; Mizuta, H. Lateral Plasma Etching Enhanced On/Off Ratio in Graphene Nanoribbon Field-Effect Transistor. *Appl. Phys. Lett.* **2015,** *106,* 033509.

[25] Barreiro, A.; Borrnert, F.; Rummeli, M. H.; Büchner, B.; Vandersypen, L. M. K. Graphene at High Bias: Cracking, Layer by Layer Sublimation, and Fusing. *Nano Lett.* **2012**, *12* 1873-1878.

[26] Murali, R. ed. *Graphene Nanoelectronics From Materials to Circuits*, (Springer Science & Business Media, LLC, 2012) p.72.

[27] Sarma, S. D.; Adam, S.; Hwang, E. H.; Rossi, E. Electronic Transport in Two-Dimensional Graphene. *Rev. Mod. Phys.* **2011**, *83* 407-470 (2011).

[28] Zou, K.; Hong, X.; Zhu, J. Effective mass of electrons and holes in bilayer graphene: Electron-hole asymmetry and electron-electron interaction. *Phys. Rev. B* **2011**, *84* 085408.

[29] Klein, N.; Gafni, N. IEEE transactions on Electron Devices **13.2**, 281-289 (1966).

[30] Ihn, T. *Semiconductor Nanostructures Quantum States and Electronic Transport*, (Oxford University Press, Oxford, 2009) p.351.

Chapter 4

Local Doping Control in HSQ Capped Graphene Nanoribbon

Graphene quantum dot(QD) is of interest to fundamental physics as well as to electronic applications. In the past decade, the electronic transport in graphene QDs, *e.g.* chaotic transport,[1] coherent electron-phonon coupling[2] and excited electronic states,[3, 4] have been widely studied. In application aspect, sensitive charge sensing by using graphene QDs [5, 6] and their room temperature operation [7] have been realized. Meanwhile, graphene is considered as a potential candidate of spin-qubit because of its low nuclear spins, which leads to a weak hyperfine coupling, and therefore a long spin coherence.[8] Recently, the observation of valley states in gate-defined bilayer graphene QDs also inspires the applications in the valley degeneracy based electronics.[9]

In contrast to the conventional semiconducting two-dimensional electron gases, monolayer graphene has no band gap making the gate defined QD impossible. Hence, to define a QD in monolayer graphene needs to firstly open an energy gap in graphene. The most straightforward approach is by patterning graphene into the desired geometry using lithography and etching techniques.[1, 2, 4–6, 10] The device structure contains a small graphene island of $< 150\,\mathrm{nm}$, where the electronic states are quantized, which is connected to the leads with the extremely narrow graphene nanoribbons (GNRs) as tunnel junctions as illustrated in chapter one. The key to guarantee the single carrier transport in such a geometry is to obtain the much larger geometrically confined energy gap ΔE_g in the GNRs,[11] compared to that of the island, which normally requires the GNRs to be narrower than

30 nm. However, the structure with such small dimensions is inevitably subjected to the disorders originated from fabrication residues, substrate defects,[12–14] and edge roughness. Subsequently, these disorders varies the spatial distribution of the chemical potential in the GNR, resulting in small unintended QDs [15–22]and parasitic charged puddles.[23] These localized states therefore smear out the anticipated single QD features.

In the graphene with opened energy gap, *e.g.* monolayer graphene nanoribbons (GNRs) with armchair edges or bilayer graphene placed in an external electrical field, QDs can be realized by electrostatic confinement with precisely defined gates.[3, 9, 24, 25] In addition to that, doping is another method to define the chemical potential landscape,[22, 26–28] which also helps to reduce the number of gates leading to a more compact and simple device structure. For graphene, doping can be introduced by chemical solutions, *e.g.* $AuCl_3$. Unfortunately this chemical process has a low spatial resolution limiting its application in defining the extremely fine structures, such as the tunnel junction of a few tens of nano-meters length. To build QD in GNR, a precisely controlled doping with good spatial resolution is required.

In this chapter, we focus on the spatial control for band structure engineering. we introduce the controllable doping to GNRs from hydrogen-silsesquioxane (HSQ) by changing its electron beam doses. Utilizing the e-beam lithography technique, $\sim$ 10 nm high spatial resolution of the doping can be easily achieved. Thanks to that, we are able to design the chemical landscape to realize single quantum dot transport in the GNR. Single dot-like transport is observed at low temperatures in the 30 nm-wide and 60 nm-long GNR with spatially controlled doping. Additionally, the geometric design rule for realizing single QD in GNR is discussed.

4.1 Introducing Doping Center to Individual Area of Graphene

Graphene devices are fabricated with monolayer graphene mechanically exfoliated on the highly doped silicon substrate covered by 300 nm-thick thermal silicon dioxide. Device fabrication follows standard nanofabrication procedure using HSQ as both etching mask and surface dopant (see Experimental section and Supporting

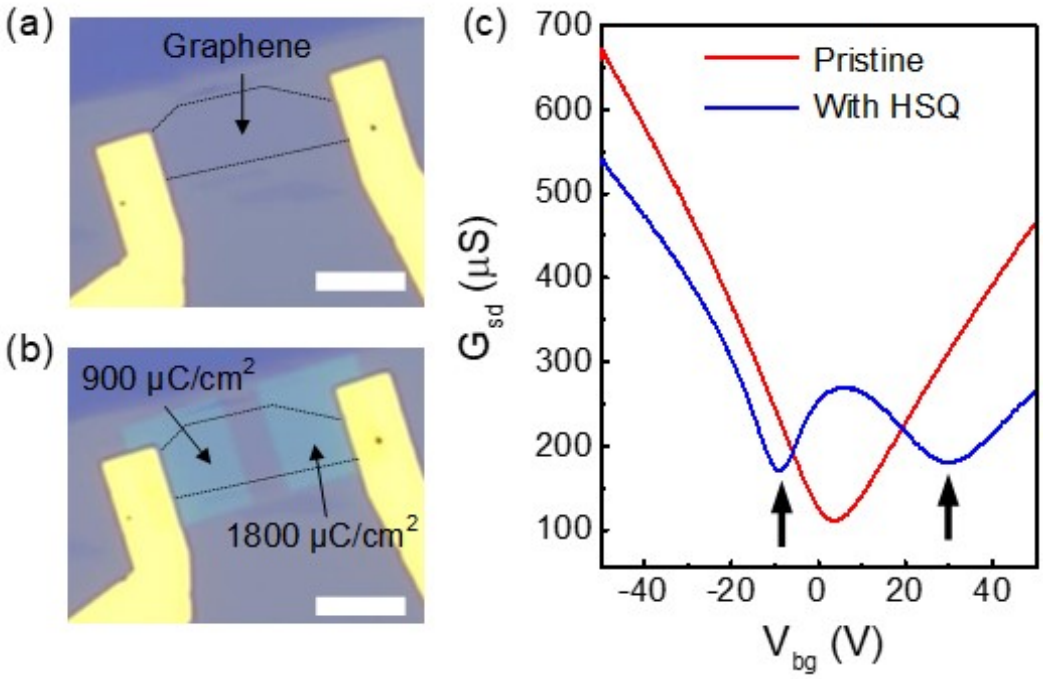

captionOptical images of a graphene device (a) without and (b) with HSQ coverage. Dashed lines are the eye guide to the edges of graphene flake. Two HSQ rectangles are patterned with different doses, which are 900 μC/cm^2 and 1800 μC/cm^2. Scale bar: 3 μm. (c) Transfer curve showing source-drain conductance G_{sd} as a function of back gate voltage V_{bg} at room temperature before and after HSQ coverage.

Information for more details). We pattern HSQ resist using electron lithography, for which a wide range of electron exposure doses from 100 μC/cm^2 to 1000 μC/cm^2 can be used. During exposure, such an aggressive electron irradiation inevitably cleaves Si-H and Si-O bonds in HSQ, resulting in hydrogen and oxygen atoms to dope the underlying graphene. To graphene, hydrogen and oxygen atoms are mild n-dopant and strong p-dopant, respectively. Moreover, it is known that the Si-H and Si-O bonds in HSQ have distinct bond strengths.[29] Hence, different doping characteristics are anticipated to be induced from HSQ under varied exposure doses.[30] In the end, the shapes of the HSQ is transferred to graphene by gentle oxygen plasma etching. The final graphene device is capped by HSQ.

Now, we demonstrate that doping can be introduced to graphene from HSQ with the well controlled doping strength by varying the electron dose. We first show a reference measurement in the graphene device without HSQ capping layer (see Fig. ??(a)). The field effect measurement shows an ambipolar transfer curve with a sole charge neutral point (CNP) at 3.5 V, indicating a slightly p-doped graphene. Then, HSQ is spun on graphene and patterned into two rectangles with two different

doses, *i.e.* 900 µC/cm^2 and 1800 µC/cm^2, as shown in Fig.??(b). According to our experiments, at a low dose of $< 1000\,\mu C/cm^2$, electron irradiation cleaves the Si-H bonds of lower bond strength without breaking Si-O bonds, leading to the *n*-type doping to graphene.[26] Increasing the dose to $> 1000\,\mu C/cm^2$, the electron irradiation is sufficient to break Si-O bonds, which generates oxygen atoms to *p*-dope graphene.[27] Subsequently, we observe two clear CNPs in the measured transfer curve at −9 V and 30 V, respectively. This feature manifests a *n*-type and a *p*-type doping centres co-existing in graphene as expected, which corresponds to the areas beneath the HSQ rectangles exposed at low and high doses, respectively. We notice that the relative shifts of CNPs are smaller at the same dose than the previously reported values, which is probably ascribed to the lower acceleration voltage and thicker HSQ layer used in our experiment.[30]

4.2 Realization of Quantum Dot-Like behaviour in GNR

Utilizing the exposure dose controlled HSQ doping, we are allowed to design a quantum dot in the selectively doped GNR. The energy band diagram is presented in Fig.4.1(a). Leads are two wide metallic graphene without transport gap opening. The quantum dot is realized with a short heavily *p*-doped GNR, in which electronic charge states are quantized due to the geometry confinement. At the ends of the GNR connecting to the leads, extremely short regions with relatively low doping compared to that in the center of GNR are designed to be the tunnel barriers. When the Fermi energy is sitting in the transport gap of the two barrier regions, the device is anticipated to behave as a quantum dot.

To realize such an energy band structure, the device as shown in Fig. 4.1 is fabricated. The fabrication process of this device can be briefly described in Fig. 4.2 The geometry is firstly defined in HSQ with varied doses and then transferred to the underlying graphene by gentle plasma etching. The GNR is defined with *p*-type doping from HSQ with a high dose of 1800 µC/cm^2. Two wide rectangles acting as source and drain leads (blue) are defined with HSQ patterned at a dose of 900 µC/cm^2. The short gaps of a few nanometers-length without direct exposure to electron beam are inserted between GNR and two leads. Nevertheless, due to the proximity effect, these two gaps can still be irradiated by electrons at a much

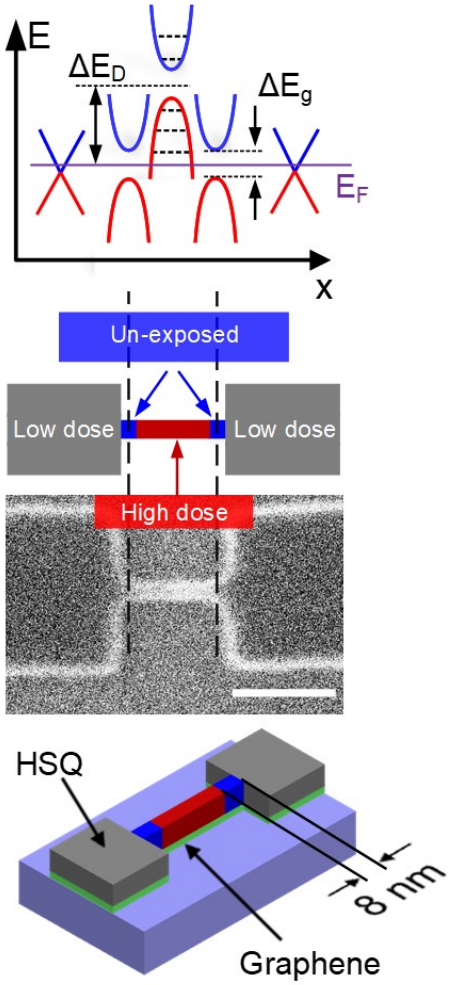

FIGURE 4.1: Schematic of the designed energy diagram of the selectively doped GNR for constructing a quantum dot. The chemical potential in the center of GNR is ΔE_{D} higher than that of the two ends connected to the leads. The middle is the illustration of geometric design of HSQ capping layer with varied doses. The wide leads (grey) are exposed with a low dose of 900 µC/cm^2, while the center of the short ribbon (red) is exposed with a high dose of 1800 µC/cm^2. Two 8 nm-long gaps (blue) inserted between leads and GNR are unexposed during lithography. The scanning electron microscopic image of the fabricated device (middle). Scale bar: 100 nm. A 3-dimensional cartoon showing the final device structure (bottom). The colors of HSQ layer indicate the exposure dose corresponding to the top panel.

lower dose than that in the center of GNR. Figure 4.1 shows a typical GNR QD device as fabricated with HSQ capped on top.

We firstly show the characterizations of a device with a 50 nm-wide and 60 nm-long GNR and 8 nm gaps (see Fig. 4.3(a)). In this device, two pronounced CNPs at the gate voltages V_{bg} of 0 V and 30 V are observed at both room temperature

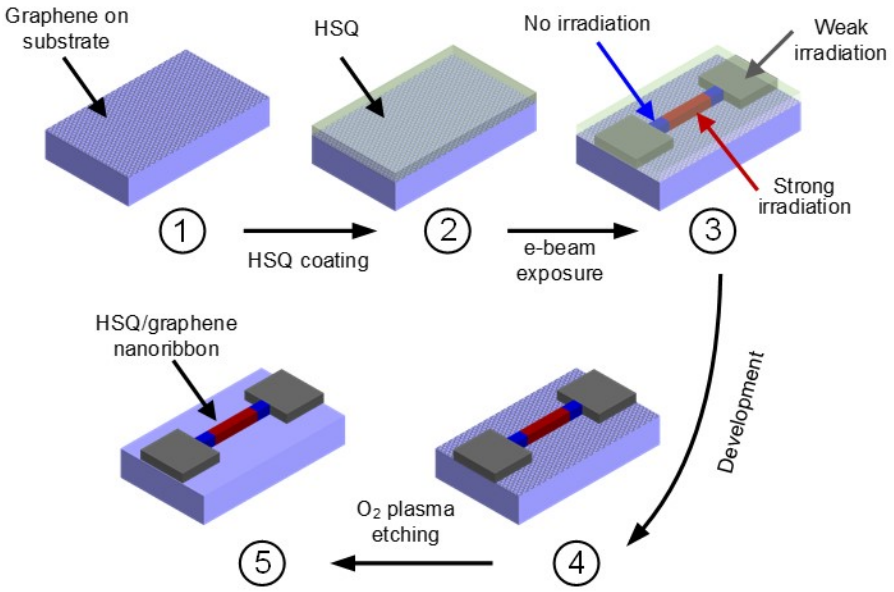

FIGURE 4.2: Schematic of the fabrication process. (1) Mechanical exfoliation of graphene onto SiO2 substrate, (2) Spin coating of HSQ layer onto graphene, (3) Exposure of HSQ by electron beam lithography with varied doses (Electron irradiation to HSQ), (4) Development of exposed HSQ layer, (5) Etching graphene using HSQ as mask in O2 plasma.

and 5 K, which manifests the existence of the local doping centers, *i.e.* the heavily p-doped GNR and weakly n-doped gap junctions. Note, as a small energy gap of ~ 10 meV is opened in the 50 nm-wide GNR, weak oscillations start to appear.

Next, we present the measurements of another device with a narrower GNR of 30 nm-width, where a larger energy gap of ~ 100 meV is expected. Figure 4.3(b) shows its gate modulation of its conductance G_{sd} at room temperature and 5 K. At room temperature multiple CNPs are noticed corresponding to the p-doped GNR and n-doped junctions. At 5 K, the strongly suppressed conductance is observed between the gate voltage V_{bg} of 0 V and 27 V, inside which clear Coulomb oscillations are observed.

To examine the formation of the QD, $\log(dI_{\mathrm{sd}}/dV_{\mathrm{sd}})$ is measured and plotted with respect to gate voltage and source-drain bias, the so-called charge stability diagram, in Fig.4.4(a). As V_{bg} is positively scanned from -10 V, the conductance reduces and eventually Coulomb diamond-like patterns appear (Region I). Most importantly, between $V_{\mathrm{bg}} \sim 0$ V to 8 V, the single QD-like transport feature, *i.e.* periodical Coulomb diamonds with clear boundaries and no overlap, are measured (Region II, see Fig. 4.4(b) for the zoomed-in details). With the further increased

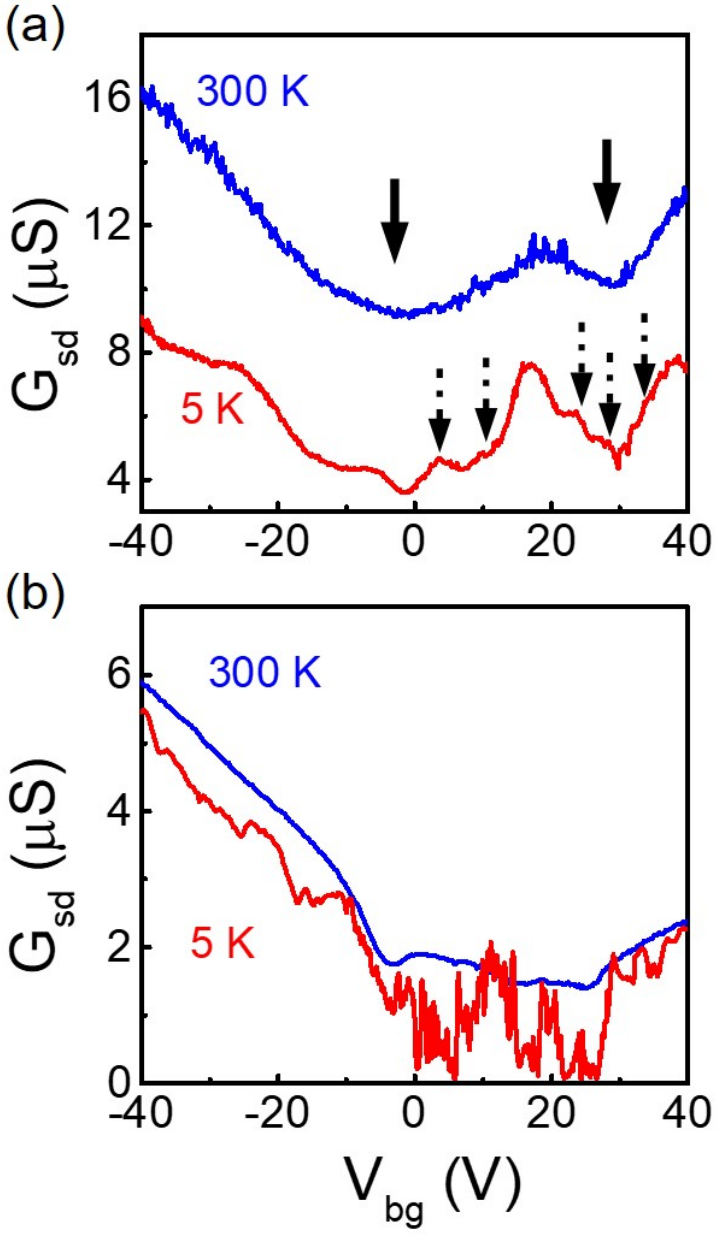

FIGURE 4.3: (a) The transfer curves measured in the device with a GNR of 50 nm wide and 60 nm long at room temperature and 5 K. Bias $V_{sd} = 1$ mV. The dark arrows indicate the locations of CNPs in the transfer curve. The thin red arrows point out these oscillation-like features. (b) The transfer curves measured in the device with a GNR of 30 nm wide and 60 nm long at room temperature and 5 K, respectively. Bias $V_{sd} = 1$ mV.

V_{bg}, conductance firstly rises (Region III), then decreases again (Region IV). Interestingly, in the Region IV, *i.e.* 14 V$< V_{bg} <$ 27 V, highly suppressed conductance is observed again. Such a phenomenon can be explained by the following scenario. A corresponding schematic energy band diagram is illustrated in Fig. 4.5. At negative gate voltages, the Fermi energy E_F is completely in the valence band

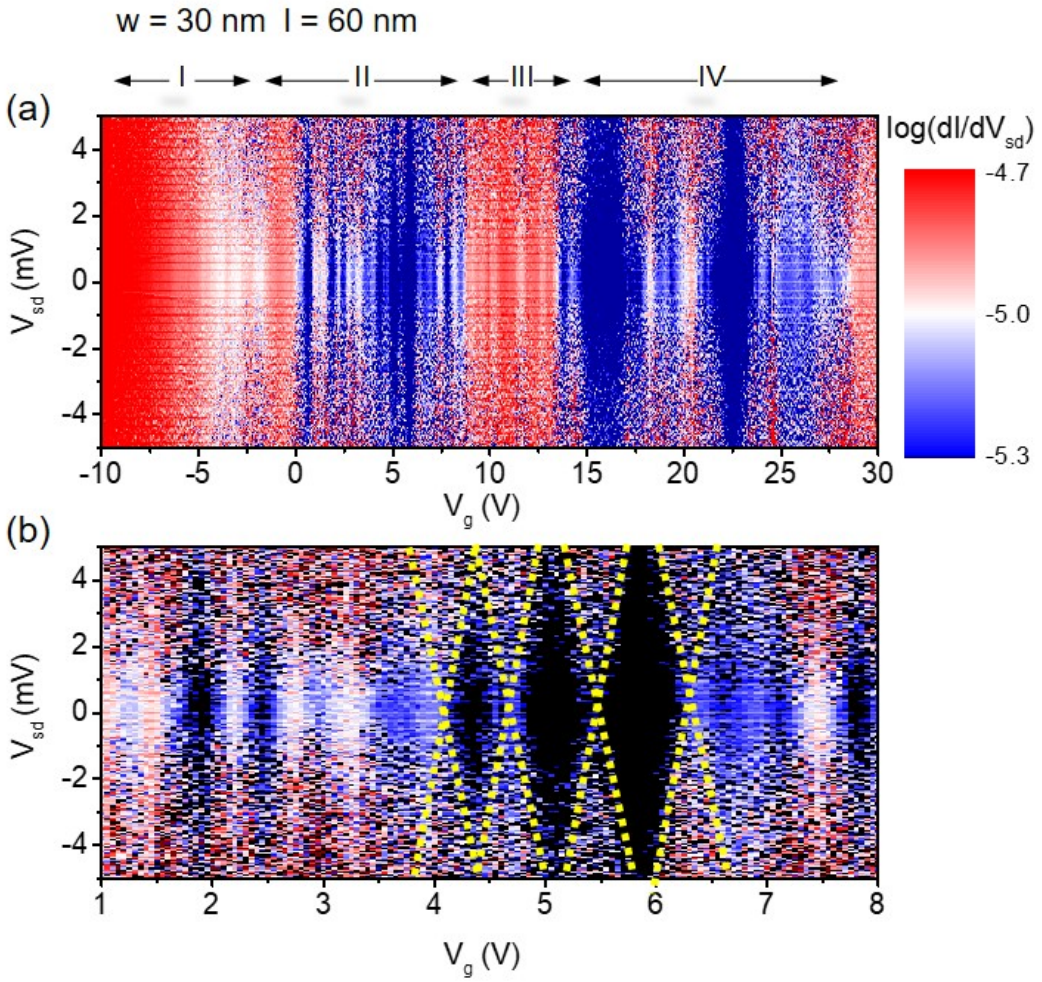

FIGURE 4.4: (a) Charge stability diagram measured in the GNR device with the width of 30 nm and length of 60 nm at 5 K. (b) Zoomed-in details of Region II in (a) showing the single quantum dot-like transport feature.

(Region I), conductance of the device is high. As V_{bg} increases positively, E_{F} is pushed into the energy gap of the "gap junctions" (Region II). Under the circumstances, two gaps act as tunnel junctions and carriers can tunnel through them between the leads and the quantized conductive GNR island, therefore resulting in the single QD transport. With increasing V_{bg}, E_{F} leaves the energy gap (Region III). The device behaves as an *n*-*p*-*n* junction, the overall conductance is enhanced compared to that of a QD. Lastly, E_{F} enters the energy gap of the p-doped GNR (Region IV), the channel is pinched off again, therefore showing the low conductance. Hence, this unique conductance fluctuation further verifies the designed band structure of the selectively doped GNR device.

Two voltage spans with low conductance, *i.e.* $-4\,\mathrm{V} \sim 8\,\mathrm{V}$ and $14\,\mathrm{V} \sim 28\,\mathrm{V}$,

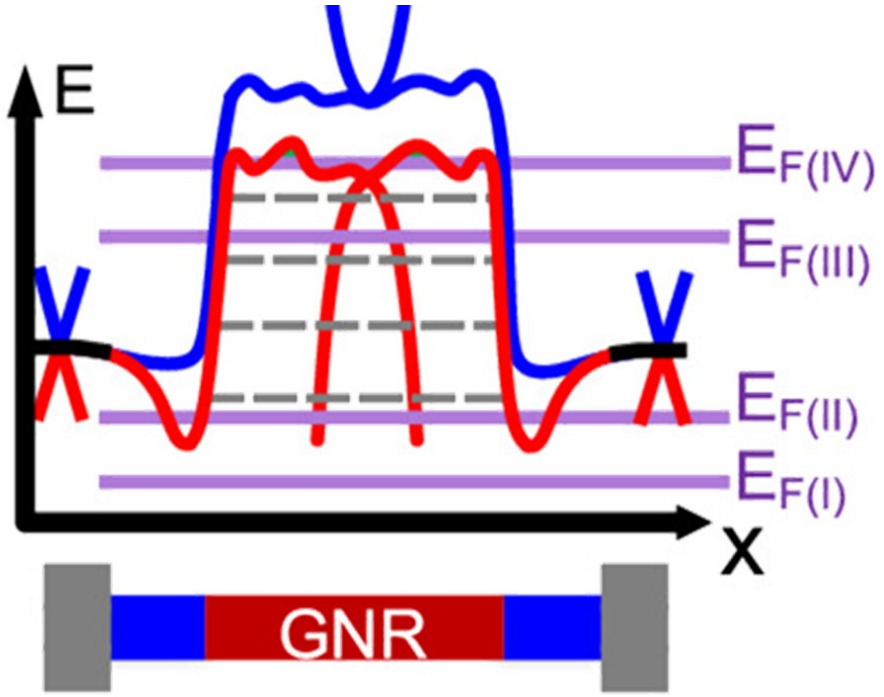

FIGURE 4.5: Schematic energy band diagram of the device. Fermi levels are marked corresponding to the four Regions, I, II, III, and IV marked in Fig. 4.4 (a)

corresponds to the energy gaps opened in the tunnel junctions and GNR, respectively. The one in the GNR is slightly larger than that in the tunnel junction. This implies that weak potential fluctuations in the GNR originated from the inevitably induced rough edges, defective substrate, and capping HSQ, which makes the actual energy gap, the so-called transport gap, larger than the confinement-induced gap ΔE_g. In the tunnel junctions, as its length is short, the spatial fluctuation is rather weak compared to that in the GNR. We convert the gate voltage span into the energy scale using the gate lever arm of 8.8 meV/V extracted from the Coulomb diamond. Hence, taking ΔV_{bg} of 12 V, the energy gap of the tunnel junction is calculated as $\Delta E_g \sim 105.6$ meV. And $\Delta V_{bg} \sim 14$ V gives the transport gap in GNR of 123.2 meV. Moreover, the potential difference ΔE_D induced by selectively doping is also estimated as 167.2meV, which corresponds to the gate voltage shift from 2 V to 21 V (Fig. 4.1 top).

More importantly, we can quantitatively extract the size of the QD from the charge stability diagram. The period of the Coulomb diamonds in the range of $V_{bg} \sim 3$ V to 7 V is measured as ~ 0.7 V which leads to an effective gate capacitance $C_g = e/\Delta V_{bg} = 0.2$ aF. Subsequently, the effective size of the QD can be calculated using the equation $A = C_g t/\varepsilon\varepsilon_0 \sim 1700\,\text{nm}^2$, where $t = 300$ nm is the thickness

of SiO_2, $\varepsilon = 3.9$ is the relative permittivity of the surrounding dielectric, and ε_0 is the vacuum permittivity, respectively. This is consistent with the designed dot size, *i.e.* the area of the GNR, $30\,\text{nm} \times 60\,\text{nm} = 1800\,\text{nm}^2$.

4.3 Geometric Design Rule for Single Dot-like Transport

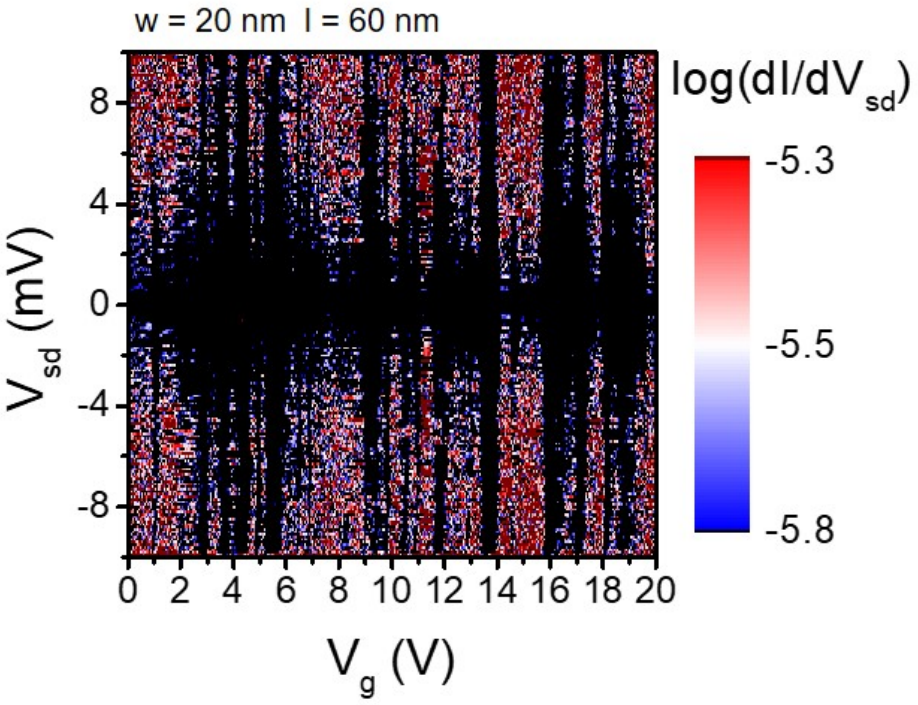

FIGURE 4.6: (Charge stability diagram measured in the GNR device with the width of 20 nm and length of 60 nm at 5 K.

Then, we discuss the geometric design rules when building the single QD with selectively doped GNR. Here two additional GNR QD devices with different dimensions are fabricated and characterized. One has a narrower GNR of 20 nm-width and 60 nm-length while another has a longer GNR of 30 nm-width and 185 nm-length, compared to the GNR of 30 nm-width and 60 nm-length showing the single QD-like transport.

Figure 4.6 presents the charge stability measured in the narrower GNR device. However, no single QD-like transport is recognized. In contrast, only the highly merged Coulomb diamond-like patterns are observed with barely distinguished boundaries, indicating the presence of multiple QDs. We know that as the GNR

becomes narrower than 30 nm, its ΔE_g increases dramatically. An empirical formula gives $\Delta E_g \sim \alpha/(w-15)$ with α being a fitting coefficient and w being the width of GNR in nanometer.[11] Taking $\Delta E_g \sim 105.6$ meV for the 30 nm-wide GNR obtained from our experiment, α is simply found as 1.58 eV·nm. Assuming a 1 nm edge roughness induced in the GNR by the plasma etching,[21] the fluctuation of ΔE_g of a 20 nm-wide GNR due to the defective edges can be roughly estimated as 131.7 meV (395 meV for the width of 19 nm and 263.3 meV for the width of 21 nm), which is one order of magnitude greater than the value of 14 meV found for a 30 nm-wide GNR (112.8 meV for the width of 29 nm and 98.8 meV for the width of 31 nm). Subsequently, it is very likely that unintended small QDs are formed in the GNR with the segments having the large energy gap as tunnel junctions, which dominates the transport.

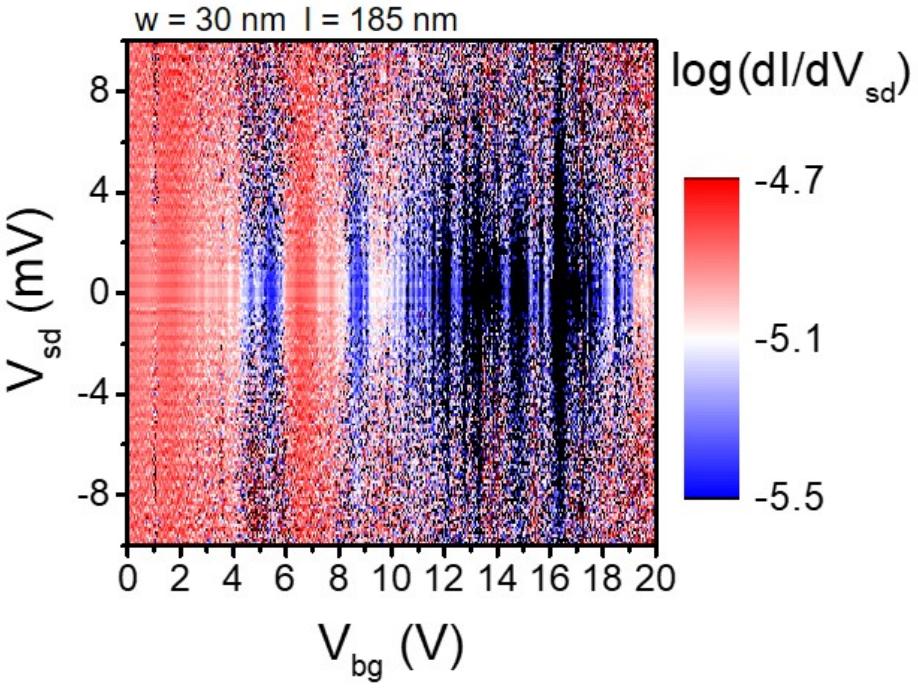

FIGURE 4.7: (Charge stability diagram measured in the GNR device with the width of 30 nm and length of 185 nm at 5 K.

In the device with the long GNR, the conductance fluctuation feature similar to that of the 60 nm-long GNR device is observed (Fig. 4.7). However, we only note the heavily overlapped Coulomb diamonds in the low conductive region. In order to realize the single QD transport, the length of the doped GNR should be less than two times of the average hopping length. When the GNR is too long, the single QD transport is unlikely, which transits into the variable range hopping (VRH) between the localized states.

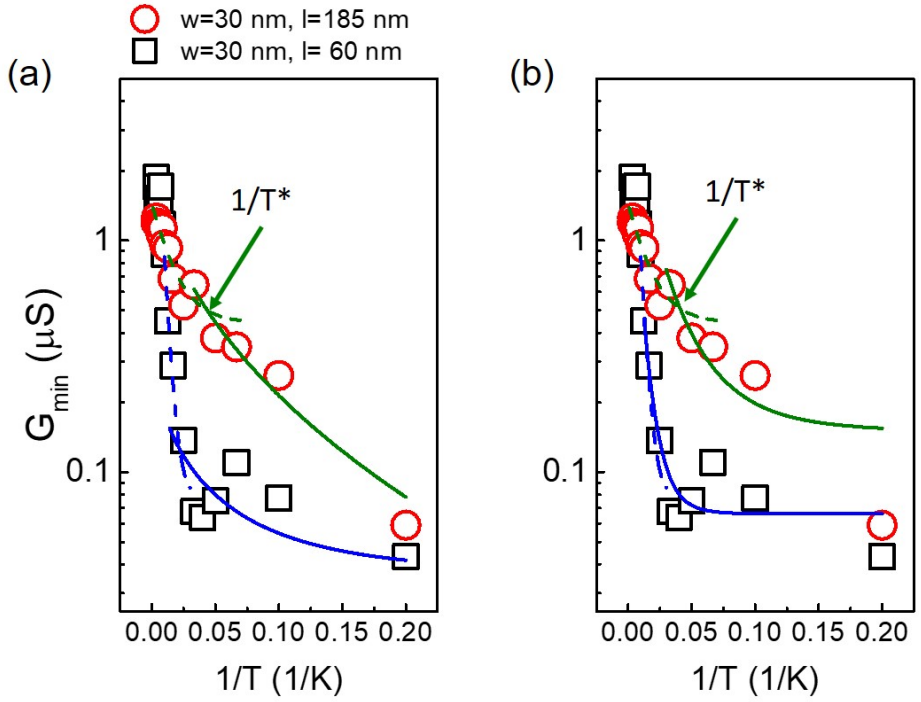

FIGURE 4.8: Comparison of T dependence of minimum conductance measured in fig. 4.4 and in fig. 4.7. The dashed lines and the solid lines are the fits to thermal activation and (a) 1-dimensional ($\gamma = 0.5$), (b) 0-dimensional ($\gamma = 1$) VRH models, respectively. The arrow denotes the inverse of the transition temperature $1/T^*$.

The average hopping length can be estimated for the GNR from the temperature dependence of the minimum conductance. Figure 4.8 plots the minimum conductance $G_{\min}$ with respect to the inverse of temperature. At the low temperature region, $G_{\min}$ increases slowly with increasing temperature. At $1/T^*$, $G_{\min}$ starts to rise rapidly. T^* is the transition temperature between thermal activation transport and VRH. We fit the data in the high temperature region to the thermal activation transport model $G_{\min} \propto \exp(-(E_a/k_{\mathrm{B}}T))$, while the low temperature data is fit to the VRH model $G_{\min} \propto \exp(-(T_0/T))^{\gamma}$, with γ ranging from 0.5 to 1 corresponding to the 1-dimensional and 0-dimensional system, respectively. The intersection of two fit lines gives the transition temperature T^* (see Fig. 4.8(c) for the fitting result with $\gamma = 0.5$, see Supporting Information for the fitting with $\gamma = 1$). The average hopping length l_{c} therefore can be calculated by using the equation $l_{\mathrm{c}} = k_{\mathrm{B}}T^*l/e\Delta V_{\mathrm{sd}}$, where l is the length of GNR and ΔV_{sd} is the bias voltage to lift the gap.[31] The average hopping length is found to be around 38 nm in both 60 nm-long and 185 nm-long GNRs using either $\gamma = 0.5$ or $\gamma = 1$, which agrees with the previous reports.[18, 31] The result suggests that the GNR should

be shorter than 75 nm in order to observe the single QD-like transport.

4.4 Local Gate Tunable Quantum Dot-Like Behaviour

In the last, we discuss the local gate tuning of the QD-like behaviour in our doped GNR. We fabricate a number of HSQ capped CVD GNRs with a local top gate on it. Initially, this gate should be < 60 nm wide and should be placed on the GNR top precisely. However, due to the misalignment in the EBL system, stage, beam, or both, we could not put gate electrodes right on the GNR top. Therefore I made a compromise, we increased the gate width to ~ 200 nm. Finally we obtained a few devices with gates. Unfortunately, these gates are still, shifted to one side of the GNR, as the simple cartoon illustration in Fig 4.9. The designed GNR width is same to the device we discussed in Fig 4.4, $w = 30$ nm, $l = 60$ nm with two ~ 8 nm-long unintentionally irradiated "gaps".

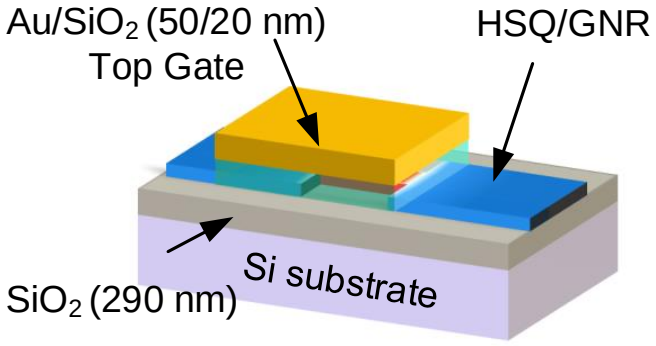

FIGURE 4.9: Schematic of the GNR devices with local top gates. Due to the misalignment, gates shifted to one side of the ribbon.

Figure 4.10 is the measured transfer curve at 5 K. Ambipolar with oscillation peaks and multiple CNPs features are noted. The CNP in the I_{sd}-V_g shifts negatively

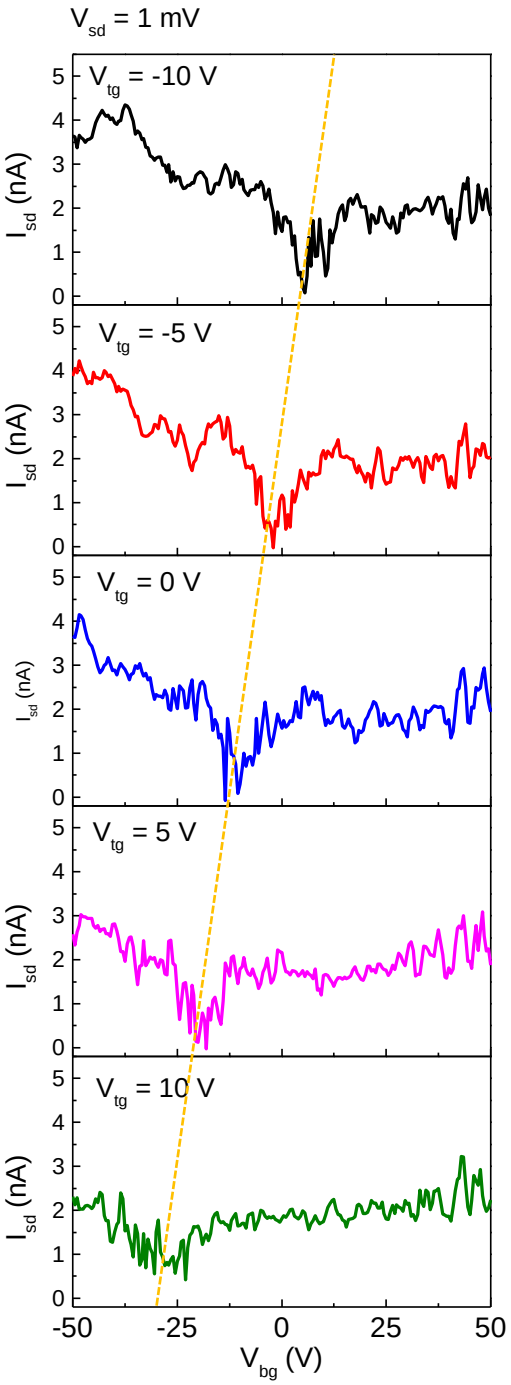

FIGURE 4.10: Gate modulated transfer curve measured in top gate biased 40 nm-wide, 60 nm-long CVD GNR device at varied top gate bias V_{tg}. The device is measured at a temperature of 5 K. The source-bias applied is 1 mV. Color dashed line is the eye guide of the CNP shifts

with increasing top gate voltage, indicating a good top gate tunability. However, the deterioration of HSQ causes GNR edges broadening, giving raise to weak quantum confinement and consequent large background current, the transport gaps are not as clear as that in the exfoliated GNRs we introduced last chapter. Fortunately, such an open quantum dot system still allows us to estimate the Coulomb blockade effect resulted QD-like features, as the dual gate sweep charge stability plot in Fig 4.11

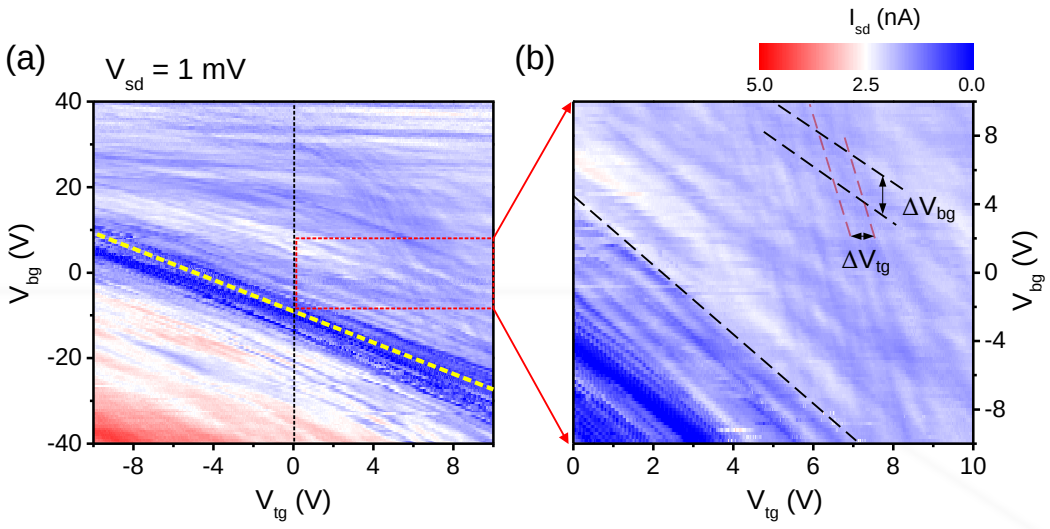

FIGURE 4.11: Dual gates stability diagram measured in device shown in Fig 4.10. (b) is the zoom up of the color rectangle region in (a).

In Fig 4.11 (a), a wide dark blue region in the stability diagram, which is the transport gap region. In the transport gap, single QD-like current peaks are read along the back gate voltage V_{bg} direction. Interestingly, with positively increasing top gate voltage, this transport gap region broadens, while the single QD-like peaks start to split, transform to a number of complex resonance. Finally, at the region $5\,\mathrm{V} < V_{\mathrm{tg}} < 10\,\mathrm{V}$, $-9\,\mathrm{V} < V_{\mathrm{bg}} < 9\,\mathrm{V}$, two shallow motions of resonance along V_{bg} and V_{tg} arise. Moreover, it seems these two resonance motions have a almost prodic peak spacing *i.e.*, $\Delta V_{\mathrm{tg}} = 0.6\,\mathrm{V}$ and $\Delta V_{bg} = 2.2\,\mathrm{V}$ suggesting the coexisting of a top gate operated QD and a back gate operated QD (see Fig 4.11). According to other reports on QDs, this is a feature of weakly coupled double QDs behaviour.[3, 4, 9, 32]

Through the periodic of current peaks along two gate voltages, we could estimated the effective size for the dots. The back gate effective capacitance $C_{\mathrm{bg}} = e/\Delta V_{\mathrm{bg}} = 0.07\,\mathrm{aF}$, corresponding to a effective dot size $A = C_{\mathrm{g}}t/\varepsilon\varepsilon_0 \sim 540\,\mathrm{nm}^2$. For top gate, the capacitance $C_{\mathrm{tg}} = 0.2\,\mathrm{aF}$, leading to $A = 240\,\mathrm{nm}$ with a

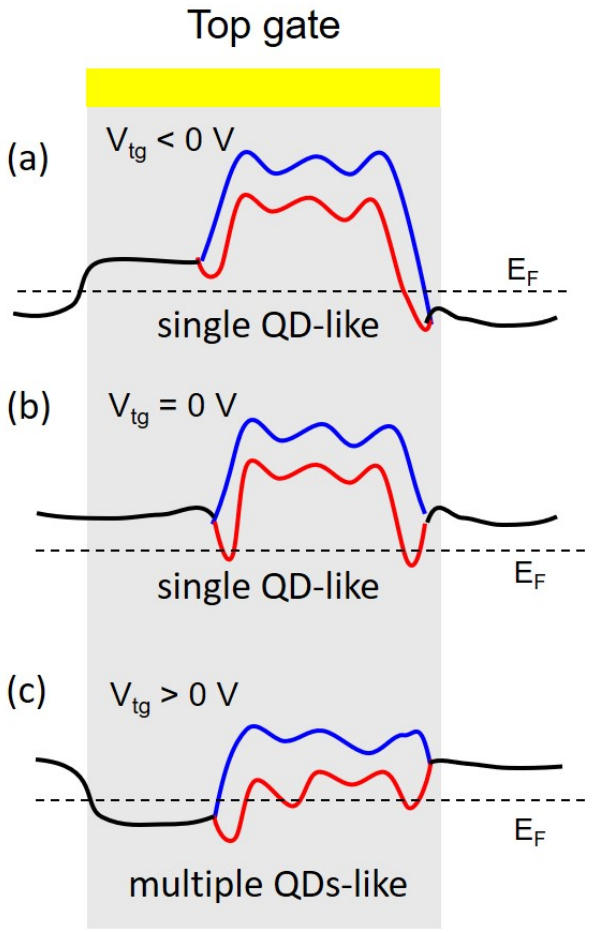

FIGURE 4.12: Schematic illustration of the band structure of the GNR at different top gate voltage region (a) $V_{\mathrm{tg}} < 0\,\mathrm{V}$, (b) $V_{\mathrm{tg}} = 0\,\mathrm{V}$ and (c) $V_{\mathrm{tg}} < 0\,\mathrm{V}$

$t = 20 + 20 = 40\,\mathrm{nm}$ being the thickness of top HSQ and e-beam evaporated SiO_2 layer. The total size of these effective areas $540 + 240 = 780\,\mathrm{nm}^2$ is smaller than the geometry of the GNR $30 \times 60 = 1800\mathrm{nm}^2$. Under this circumstance, the formation of these dots in most like stemmed from the top gate bias induced band pining impacts on the doping controlled GNR chemical landscape.

The observed transform from single QD-like to double QD-like features can be attributed to the top gate voltage bias caused band pinning as the cartoon illustrated in Fig 4.12. Because of the misalignment, top gate is not in the centere of GNR. Therefore the top gate bias affects the left tunnel barrier more. With a negative V_{tg}, the Fermi energy of the top gate effected area is shifted towards conduction band (Fig 4.12 (a)). With increasing top gate voltage to $V_{tg} = 0\,\mathrm{V}$, the band structure recovers to the condition similar to Fig4.5. In this two regions, the current oscillation is single QD-like. However, further increasing the V_{tg} pins the two doping controlled barriers to valence band, results in a shrinking of these

two barrier heights. In the meantime, the scale of the disordered centre ribbon transport gap thickness increased, subsequently, the impacts of disordered gaps on the electron confinement increased, leading to the multiple QD-like features as we observed in the stability diagram.

4.5 Summary

In summary, we demonstrate the controllable doping from HSQ to graphene realized by changing the electron beam dose. As a fine electron-beam resist, an extremely high spatial resolution of doping can be realized with HSQ. Additionally, geometric patterning and chemical doping are integrated into a single step, therefore reducing the complexity of the fabrication. Using such a method, we are able to design and achieve the single QD-like transport in the GNR. Moreover, the geometric design rule is roughly investigated, manifesting that a relatively short and wide GNR is suggested for observing the single QD-like transport. We envisage that this method can be utilized to other two-dimensional materials and in other applications, such as *pn* junctions and tunnel field-effect transistor. In the future, a local finger gate can be added in addition to the global back gate to tune the chemical potential of GNR island individually for the better control of the QD transport.

Bibliography

[1] Ponomarenko, L. A.; Schedin, F.; Katsnelson, M. I.; Yang, R.; Hill, E. W.; Novoselov, K. S.; Geim, A. K. Chaotic Dirac Billiard in Graphene Quantum Dots. *Science* **2008,** *320*, 356-358.

[2] Roulleau, P.; Baer, S.; Choi, T.; Molitor, F.; Güttinger, J.; Müller, T.; Dröscher, S.; Ensslin, K.; Ihn, T. Coherent Electron-Phonon Coupling in Tailored Quantum Systems. *Nat. Commun.* **2011,** *2,* 239.

[3] Liu, X.L.; Hug, D.; Vandersypen, L.M. Gate-Defined Graphene Double Quantum Dot and Excited State Spectroscopy. *Nano Lett.*, **2010,** *10,* 1623-1627.

[4] Volk, C.; Fringes, S.; Terrés, B.; Dauber, J.; Engels, S.; Trellenkamp, S.; Stampfer, C.; Electronic Excited States in Bilayer Graphene Double Quantum Dots. *Nano Lett.* **2011,** *11,* 3581-3586.

[5] Güttinger, J.; Stampfer, C.; Hellmüller, S.; Molitor, F.; Ihn, T.; Ensslin, K. Charge Detection in Graphene Quantum Dots. *Appl. Phys. Lett.* **2008,** *93,* 212102.

[6] Wang, L.J.; Cao, G.; Tu, T.; Li, H.O.; Zhou, C.; Hao, X.J.; Su, Z.; Guo, G.C.; Jiang, H.W.; Guo, G.P. A Graphene Quantum Dot with a Single Electron Transistor as an Integrated Charge Sensor. *Appl. Phys. Lett.* **2010,** *97,* 262113.

[7] Barreiro, A.; van der Zant, H.S.; Vandersypen, L.M. Quantum Dots at Room Temperature Carved Out from Few-Layer Graphene. *Nano Lett.* **2012,** *12,* 6096-6100.

[8] Trauzettel, B.; Bulaev, D.V.; Loss, D.; Burkard, G. Spin Qubits in Graphene Quantum Dots. *Nat. Phys.* **2007,** *3,* 192-196.

[9] Eich, M.; Pisoni, R.; Overweg, H.; Kurzmann, A.; Lee, Y.; Rickhaus, P.; Ihn, T.; Ensslin, K.; Herman, F.; Sigrist, M.; Watanabe, K. Spin and Valley States in Gate-Defined Bilayer Graphene Quantum Dots. *Phys. Rev. X* **2018,** *8,* 031023.

[10] Stampfer, C.; Schurtenberger, E.; Molitor, F.; Guttinger, J.; Ihn, T.; Ensslin, K.; Tunable Graphene Single Electron Transistor. *Nano Lett.* **2008,** *8,* 2378-2383.

[11] Han, M.Y.; Özyilmaz, B.; Zhang, Y.; Kim, P. Energy Band-Gap Engineering of Graphene Nanoribbons. *Phys. Rev. Lett.* **2007,** *98,* 206805.

[12] Zhang, Y.; Brar, V.W.; Girit, C.; Zettl, A.; Crommie, M.F. Origin of Spatial Charge Inhomogeneity in Graphene. *Nat. Phys.* **2009,** *5,* 722-726.

[13] Xue, J.; Sanchez-Yamagishi, J.; Bulmash, D.; Jacquod, P.; Deshpande, A.; Watanabe, K.; Taniguchi, T.; Jarillo-Herrero, P.; LeRoy, B.J. Scanning Tunnelling Microscopy and Spectroscopy of Ultra-flat Graphene on Hexagonal Boron Nitride. *Nat. Mater.* **2011,** *10,* 282-285.

[14] Samaddar, S.; Yudhistira, I.; Adam, S.; Courtois, H.; Winkelmann, C.B. Charge Puddles in Graphene Near the Dirac Point. *Phys. Rev. Lett.* **2016,** *116,* 126804.

[15] Todd, K.; Chou, H.T.; Amasha, S.; Goldhaber-Gordon, D. Quantum Dot Behavior in Graphene Nanoconstrictions. *Nano Lett.* **2009,** *9,* 416-421.

[16] Stampfer, C.; Güttinger, J.; Hellüller, S.; Molitor, F.; Ensslin, K.; Ihn, T. Energy Gaps in Etched Graphene Nanoribbons. *Phys. Rev. Lett.* **2009,** *102,* 056403.

[17] Gallagher, P.; Todd, K.; Goldhaber-Gordon, D. Disorder-Induced Gap Behavior in Graphene Nanoribbons. *Phys. Rev. B* **2010,** *81,* 115409.

[18] Terrés, B.; Dauber, J.; Volk, C.; Trellenkamp, S.; Wichmann, U.; Stampfer, C. Disorder Induced Coulomb Gaps in Graphene Constrictions with Different Aspect Ratios. *Appl. Phys. Lett.* **2010,** *98,* 032109.

[19] Bischoff, D.; Libisch, F.; Burgdörfer, J.; Ihn, T.; Ensslin, K. Characterizing Wave Functions in Graphene Nanodevices: Electronic Transport Through Ultrashort Graphene Constrictions on a Boron Nitride Substrate. *Phys. Rev. B* **2014,** *90,* 115405.

[20] Bischoff, D.; Varlet, A.; Simonet, P.; Eich, M.; Overweg, H.C.; Ihn, T.; Ensslin, K. Localized Charge Carriers in Graphene Nanodevices. *Appl. Phys. Rev.* **2015,** *2,* 031301.

[21] Sun, J.; Iwasaki, T.; Muruganathan, M.; Mizuta, H. Lateral Plasma Etching Enhanced On/Off Ratio in Graphene Nanoribbon Field-Effect Transistor. *Appl. Phys. Lett.* **2015,** *106,* 033509.

[22] Wang, Z.; Sun, J.; Muruganathan, M.; Mizuta, H. Electrically Tunable Localized States in Sub-Band of Bilayer Graphene Nanoribbon. *Appl. Phys. Lett.* **2018,** *113,* 133101.

[23] Wei, D.; Xie, L.; Lee, K.K.; Hu, Z.; Tan, S.; Chen, W.; Sow, C.H.; Chen, K.; Liu, Y.; Wee, A.T.S.; Controllable Unzipping for Intramolecular Junctions of Graphene Nanoribbons and Single-Walled Carbon Nanotubes. *Nat. Commun.* **2013,** *4,* 1374.

[24] Liu, X.; Oostinga, J.B.; Morpurgo, A.F.; Vandersypen, L.M. Electrostatic Confinement of Electrons in Graphene Nanoribbons. *Phys. Rev. B* **2009,** *80,* 121407.

[25] Banszerus, L.; Frohn, B.; Epping, A.; Neumaier, D.; Watanabe, K.; Taniguchi, T.; Stampfer, C. Gate-Defined Electron-Hole Double Dots in Bilayer Graphene. *Nano Lett.* **2018,** *18,* 4785-4790.

[26] Ryu, S.; Han, M.Y.; Maultzsch, J.; Heinz, T.F.; Kim, P.; Steigerwald, M.L.; Brus, L.E. Reversible Basal Plane Hydrogenation of Graphene. *Nano Lett.* **2008,** *8,* 4597-4602.

[27] Liu, L.; Ryu, S.; Tomasik, M.R.; Stolyarova, E.; Jung, N.; Hybertsen, M.S.; Steigerwald, M.L.; Brus, L.E.; Flynn, G.W. Graphene Oxidation: Thickness-Dependent Etching and Strong Chemical Doping. *Nano lett.* **2008,** *8,* 1965-1970.

[28] Muruganathan, M.; Sun, J.; Imamura, T.; Mizuta, H. Electrically Tunable van der Waals Interaction in Graphene-Molecule Complex. *Nano lett.* **2015,** *15,* 8176-8180.

[29] Yang, C.C.; Chen, W.C. The Structures and Properties of Hydrogen Silsesquioxane (HSQ) Films Produced by Thermal Curing. *J. Mater. Chem* **2002,** *12,* 1138-1141.

[30] Brenner, K.; Murali, R. Single step, Complementary Doping of Graphene. *Appl. Phys. Lett.* **2010,** *96,* 063104.

[31] Han, M.Y.; Brant, J.C.; Kim, P. Electron Transport in Disordered Graphene Nanoribbons. *Phys. Rev. Lett.* **2010,** *104,* 056801.

[32] Van der Wiel,W. G.; De Franceschi, S.;X Elzerman, S.; Fujisawa, T; Tarucha, S; Kouwenhoven L. P. Electron transport through double quantum dots. *Rev. Mod. Phys.* **2002,** *75,* 1

Chapter 5

Fabrication of Suspended Graphene Quantum Dot System

In parallel to the charge transfer doping control, I have also worked on the fabrication of suspended graphee quantum dot system. Coupling single charge transport to mechanical motion is useful for ground state cooling,[1] sensitive charge sensing,[2] and atomic scale mass detection.[3] This coupling can be realized by embedding a single electron transistor (SET) in a nanoelectromechanical resonator. In this field, carbon based materials, i.e., suspended carbon nanotubes (CNTs) and graphene nanoribbons (GNRs), are appealing due to their stiffness, widely tunable resonance frequency and exceptional transport properties.[2–4] To gain an insight view of the coupling mechanism, it is necessary to develop the single dot SET to double dots. Double quantum dots can be realized by nanopatterning graphene. However, these channels easily deform during the supporting substrate etching process. To guarantee such a fragile structure, it is better to define the dots after suspending the channel. Helium ion beam milling (HIBM) has been demonstrated as an efficient technique for shaping suspended graphene into sub-10 nm scale structures with small deformation owing to its small beam diameter, fine spatial resolution and suitable energy.[6] Therefore, well-shaped suspended graphene double quantum dot can be expected using HIBM. So far, fabrication processes for such a complex suspended structure is still under development.

In this chapter, we present our approach toward the realization suspended graphene quantum dots system. A relatively large GNR (width w=500 nm, length l=1000

nm) with seven stiff metal electrodes on its edges was pre-fabricated through conventional e-beam lithography fabrication process. Among the seven electrodes, two larger electrodes with a width of 1000 nm were defined as source and drain. The other smaller electrodes with widths of ~ 50 nm were later defined as side gates. Afterward, the substrate was etched out by using BHF. These strong electrodes pulled the GNR and kept its shape from deformation during etching. Then HIBM was carried out to pattern the GNR into single or double dots structures. Impressively, two islands with a diameter smaller than 100 nm connecting to source and drain through constrictions with a width of sub-10 nm are obtained. Although, desired characteristic are not obtained from the experiment, the success in suspended graphene double QD patterning provide useful informations for the future development of graphene nano electromechanics (NEMs) and QDs.

5.1 Helium Ion Beam Milling for Graphene Nanoribbon Patterning

Helium ion beam belongs to the focused ion beam technology family which holds the smallest beam diameter down to 0.25 nm. Compared to electron beam, helium ion beam has a shorter wavelength, leading to smaller forward scattering. The energy of Thanks to that, sub-10 nm scale patterning is expected from helium ion beam milling technology (HIBM).[5, 6]

Unlike e-beam lithography, the high energy ion beam allows us to directly mill and spatter the irradiated sample. Therefore the HIBM shaping does not require resist. The helium ions will either goes into the substrate, or be evacuated in vacuum. Thanks to that, HIBM offers a choice for cleaner graphene nano-fabrication in principle.

However, the high energy helium ion beam will spatter substrate material and incurs into it as well. Because of that, the substrate irradiated by helium ions swells like a balloon. Also the back scattering of helium ions cause additional damage to the fragile graphene lattice, leading to a massive scale of point defects. Subsequently, Anderson localization takes places resulting in poor electrical conductivity.[7–9]

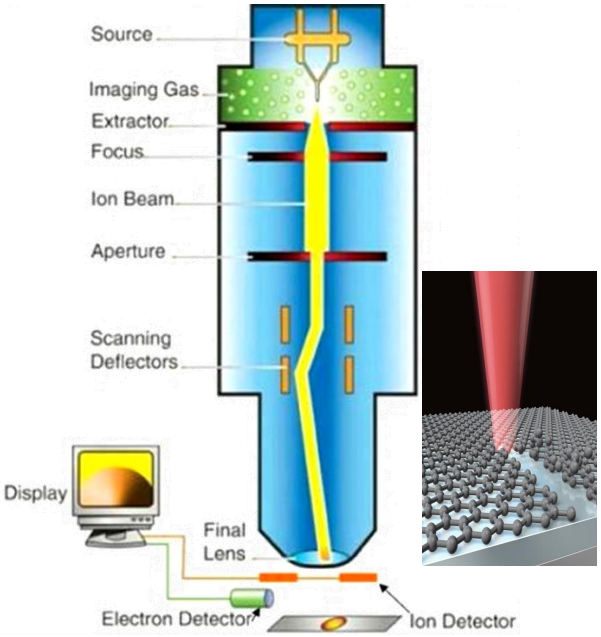

FIGURE 5.1: Schematic illustration of a helium ion beam microscope.

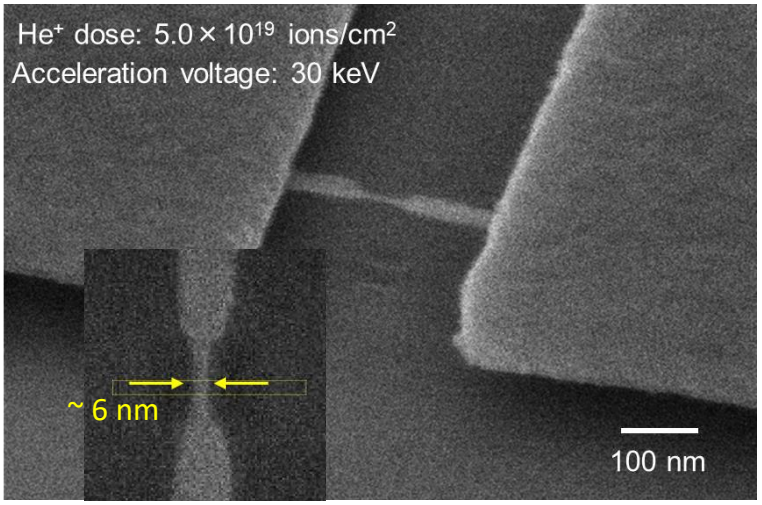

FIGURE 5.2: SEM image of a HIBM patterned graphene nanoribbon. The width of the centre GNR is $\sim 6\,\text{nm}$

Keeping the above results in mind, later we performed HIBM for suspended graphene with an 200 nm air gap. the results is shown in Fig5.2. Impressively, a width down to $\sim 6\,\text{nm}$ suspended GNR is achieved by using this technology. The I_{sd}-V_{sd} measurement results is plotted in Fig 5.3. An energy gap of $\sim 0.5\,\text{eV}$ is estimated directly from the plotting, which meets the requirements for the majority semiconductor electronics application.

The promising result encouraged the feasibility of the usage of HIBM in energy gap opened GNR patterning, we put more efforts to develop this technology as

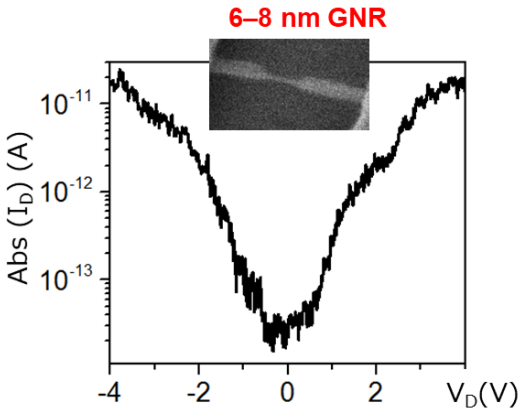

FIGURE 5.3: The I_{sd}-V_{sd} measurement for the device shown in Fig 5.2

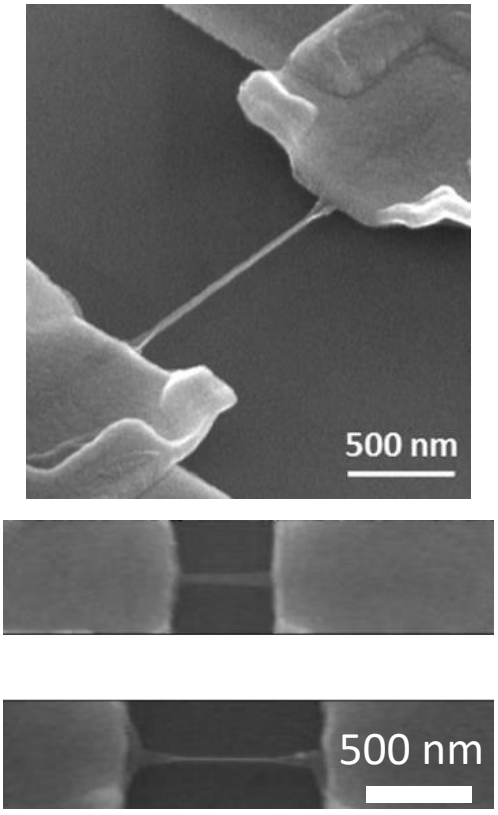

FIGURE 5.4: SEM images of the GNRs after substrate etching. The edges rolls towards to its center and GNR becomes a "carbon nano tube"

well as the related fabrication process. However, we soon met another challenge in the device fabrication. The edges of suspended GNRs have a high possibility to roll up during the substrate wet etching and super critical dry processes as we can clearly see in the SEM images (Fig 5.4).

This phenomena is stemmed from a interplay of GNR surface tension and innerstress. Although, changing the GNR aspect ratio, *i.e.*, making the width wider

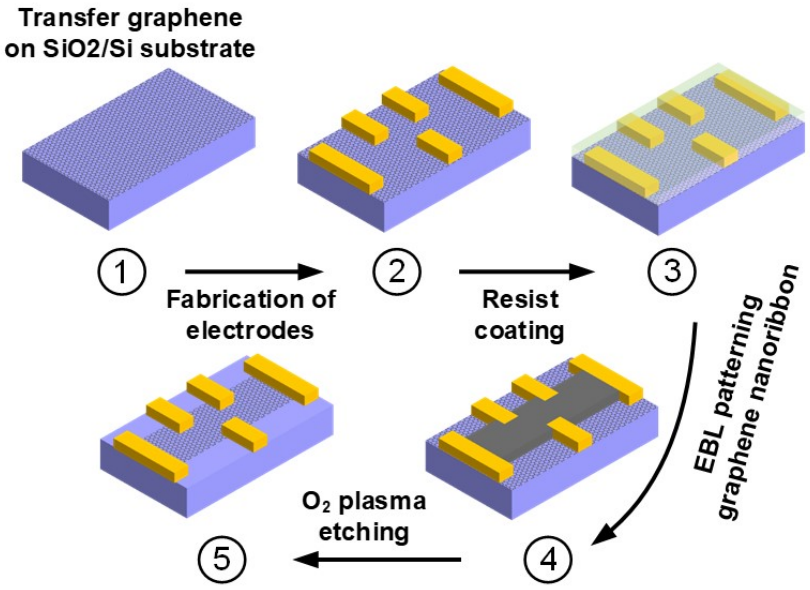

FIGURE 5.5: Schematic illustration of the fabrication process of GNRs for helium ion beam milling

while the length shorter, is a solution, which leads to a larger GNR geometry and a longer HIBM time. Moreover, it appeals that a GNR length of $1\sim 2\,\mu m$ is required to put plunger gates for the final suspended graphene QD operation. Therefore, new fabrication procedure development is required for this special device.

5.2 Fabrication of Suspended Graphene Nanoribbon for HIBM patterning

The strategy of avoiding rolling up is illustrated in Fig 5.5. A quick also efficient solution of the GNR edges rolling is adding electrodes at their edges, so this gates serve as a "bridge pier" that drag the edge and prevent it from wet etching. Later, during the HIBM patterning, we can separate the gate from GNR, so the "bridge pier" then becomes a side gates.

The suspended graphene nanoribbon fabrication starts with transferring mechanically exfoliated graphene to doped silicon substrate covered by 285 nm thermally grown oxide layer. The two large source and drain electrodes and five small gate electrodes are fabricated on graphene through conventional nano-fabrication process. The gate widths are 50 nm. Between two adjacent electrodes, a space of 100 nm is kept. Importantly, we used AR-P 6200 resist to pattern this electrodes.

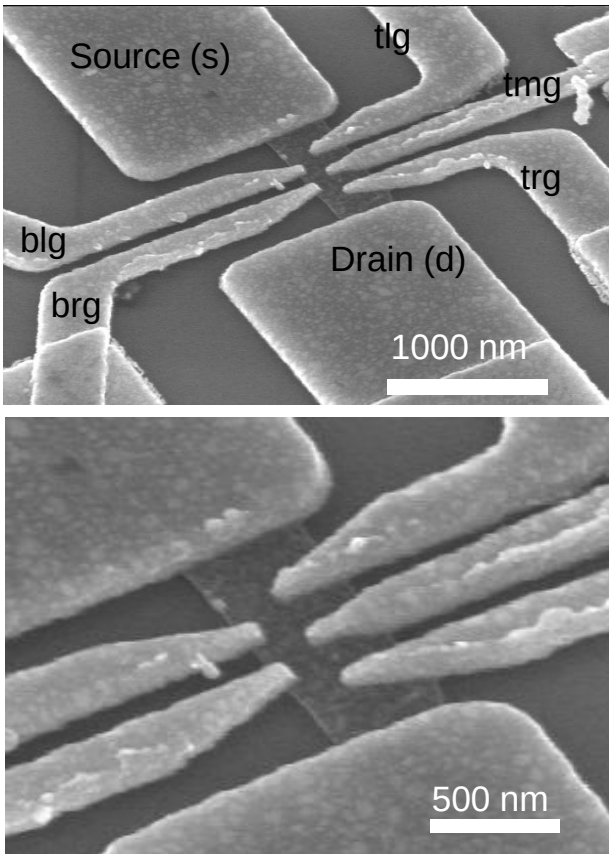

FIGURE 5.6: SEM image of a suspended graphene nanoribbon. The bottom figure is the zoom up of the top figure.

Then we patterned the graphene into a 500 nm wide, 1000 nm long nanoribbon. Thereafter the substrate is etched out via a wet etching (40 s in 46% BHF solution) followed by a critical point dry. The SEM image of fabricated device is shown in Fig 5.6 (a).

The electrical characterization is carried out as soon as we confirmed the suspension of GNR channel. The measured I-V and gate modulation transfer curve characteristics are shown in Fig 5.7. All the contacts show nice Ohmic contact features. In the gate modulation transfer curve, we see a p-doped ambipolar characteristic. The position of CNP is at $V_g > 20\,\mathrm{V}$ because the air gap of $\sim 70\,\mathrm{nm}$ between substrate and GNR. Taking the parallel-plate capacitor model, the gate capacitance reduced by a factor of 1/3

$$C = \frac{\epsilon\epsilon_0 \times A}{h}\{1 + O(\frac{\log(\frac{\sqrt{A}}{h})}{\frac{2\sqrt{A}}{h}})\} \tag{5.1}$$

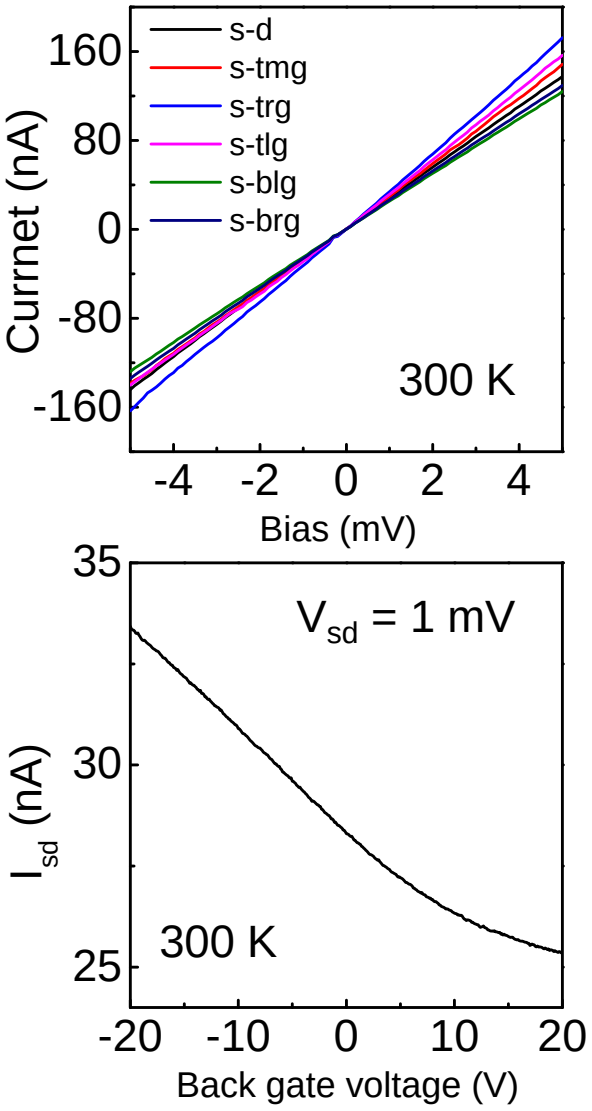

FIGURE 5.7: Electrical characterization of the device shown in Fig 5.6

with

epsilon = 1 for air, $h = 70\,\text{nm}$ being the air gap and $A = 500\,\text{nm} \times 1000\,\text{nm}$ being the nanoribbon area. Assuming the device is not suspended, the the CNP should be within $V_{\text{bg}} < 10\text{V}$. Therefore, the p-doping nature is actually not that strong. Nevertheless, through out the above preparation, the sample is ready for HIBM patterning.

5.3 HIBM Patterning

After the prefabrication, HIBM is carried out in a Zeiss Orion Plus made helium ion microscope at a pressure of $< 5 \times 10^{-5}\,\text{Pa}$. A beam current of 1 pA under a

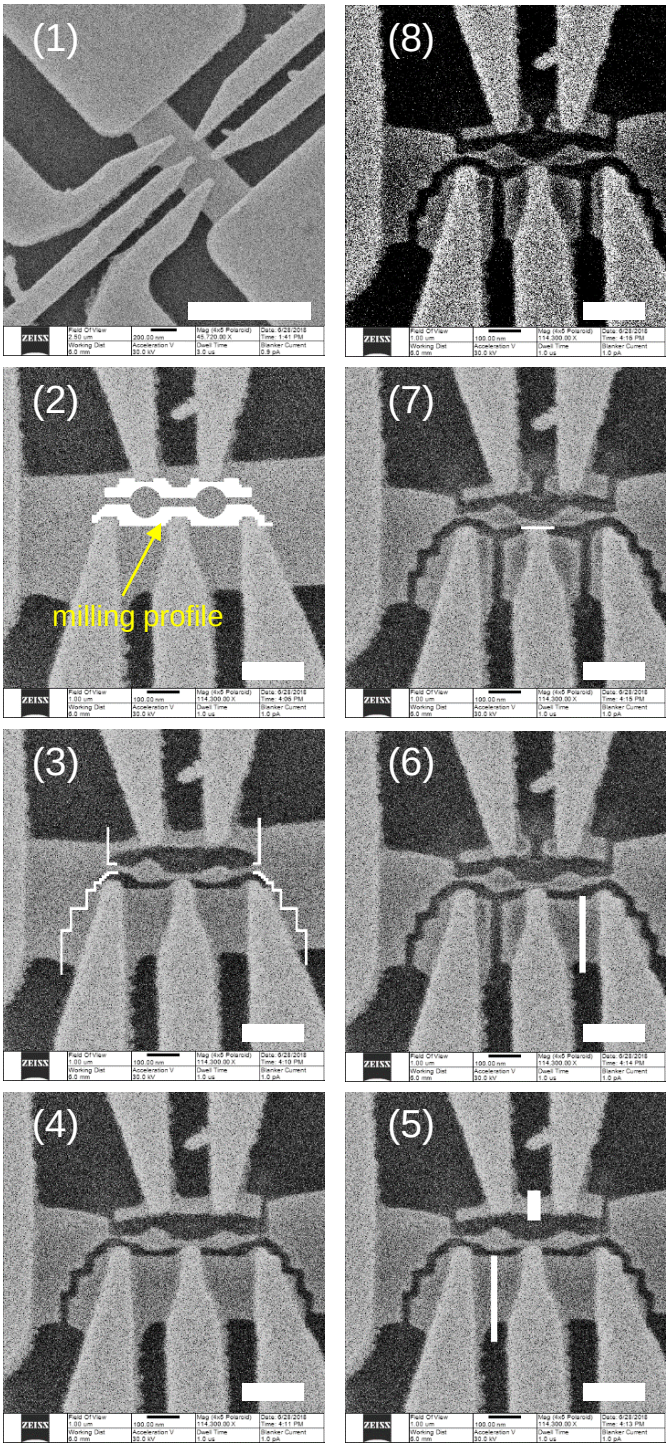

FIGURE 5.8: Helium ion beam microscopy images of Device A taken during the HIBM patterning. Numbers on the left top conner (from (1) to (8)) denote the order of the milling procedure. The scale bar is 1000 nm

acceleration voltage of 30 kV is setted. With this setting, the beam diameter is minimized to 0.25 nm. The milling dose applied for line shaping is 1×10^{18}ions/cm^2. Figure 5.8 is the helium ion beam microscopy images taken during the milling. For the convenience, we denoted this device as Device A. In the first experiment, we patterned the centre dots then milled the other parts. Impressively, the circular dot, the wings, didn't fall down during the HIBM. We achieved a tunnel junction width smaller than previous 6 nm wide-GNR, while a dot size < 70 nm. In principle, the smaller geometry leads to a stronger quantum confinement as well as a larger single particle spectrum space, which is crucial for the study and operation of single electron transport related physics. Unfortunately, it is appealing that the centre dot channel easily deform, and stacks to the close side gates. Later we found by changing the milling order, one is able to avoid such deformation issue.

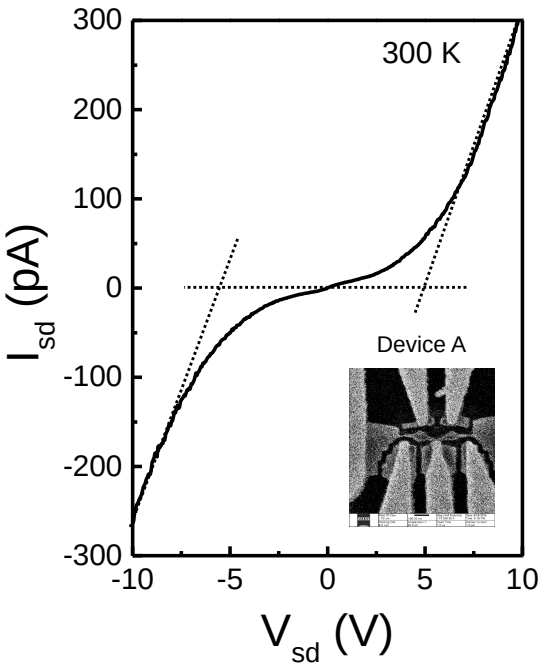

FIGURE 5.9: Measured I_{sd}-V_{sd} characteristic in Device A after HIBM patterning.

The measurement results of this device is shown in Fig 5.9. Compared to the measurement results before annealing 5.7, the I_{sd}-V_{sd} characteristic changed drastically. A non-linear region $-6\,\mathrm{V} < V_{sd} < 4\,\mathrm{V}$ is read. On both sides of this region, the current increased readily with increasing bias voltage, finally the I_{sd}-V_{sd} curve becomes linear. This is a signature of transport gap opening in V_{sd} direction due to the HIBM patterning. The measured V_{sd} gap corresponds to an energy gap ~ 5 eV, indicating the device is converted to insulator. Such HIBM irradiation

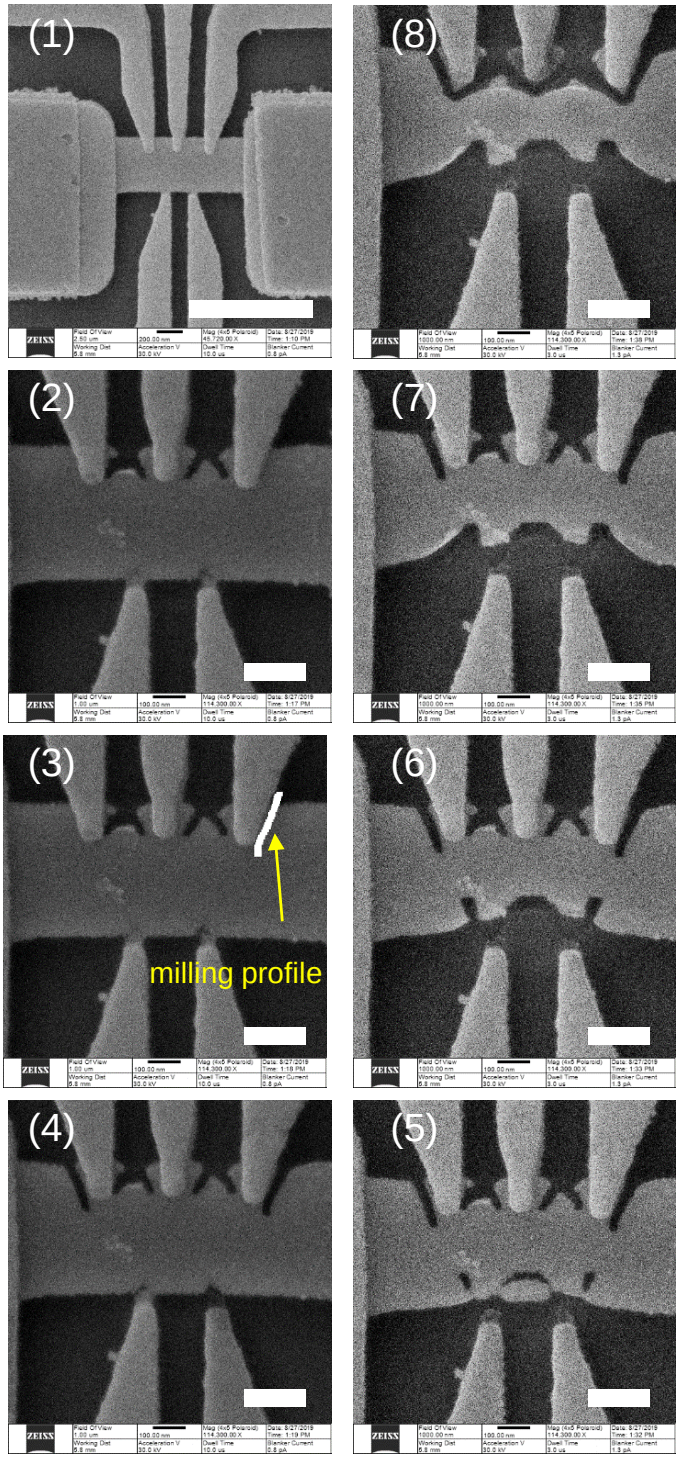

FIGURE 5.10: Helium ion beam microscopy images of Device B taken during the HIBM patterning. N The scale bar is 1000 nm

induced metal-semiconductor-insulator transition in graphene have been reported by Nakaharai *et al.* [9] In our experiment, this is due to i) the HIBM induced defects and ii) the ultra-small nano ribbon junction width.

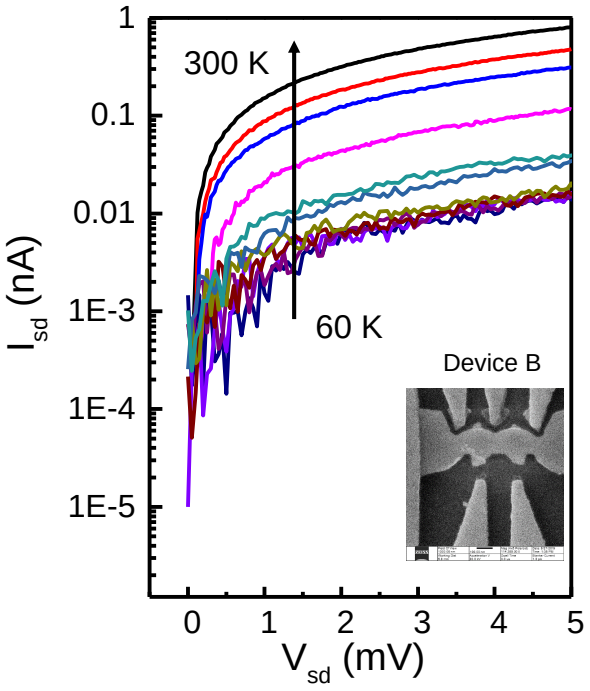

FIGURE 5.11: Measured I_{sd}-V_{sd} characteristic in Device B after HIBM patterning at varied temperature (from 300 K to 60 K).

In the second experiment, we decide to increase the device geometry to avoid the metal-insulator transition. In addition, we changed the patterning order, *i.e.*, from out side to the centre dot as shown in Fig 5.10. From the images we took during HIBM, we see also found the deformation occurs at each step. But, with this out-centre order, the graphene shirks to its centre rather than shifted to up or down. Finally, a double QD-devices with a dot diameter of 150 nm and a tunnel junction width of 80 nm is obtained. This device is denoted as Device B.

Figure5.11 plots measured I_{sd}-V_{sd} curve in a semilog scale. The device exhibit Ohmic I_{sd}-V_{sd} at room temperature with a resistance of $R = 6.2\,\mathrm{M}\Omega$, which is larger than the quantum resistance $e^2/\hbar = 2.6\mathrm{M}\Omega$, implies a possibility for room temperature SET operation. The resistance increased with decreasing temperature. At 60 K, the current barely flows because the carrier freezing. Though Device B shows a better electrical property, the side gates are not working as we expected. The stability diagram of two dot plunger gates are plotted in Fig 5.12.

The source-drain current almost independent on the gate voltages, implies a poor gate tunablility.

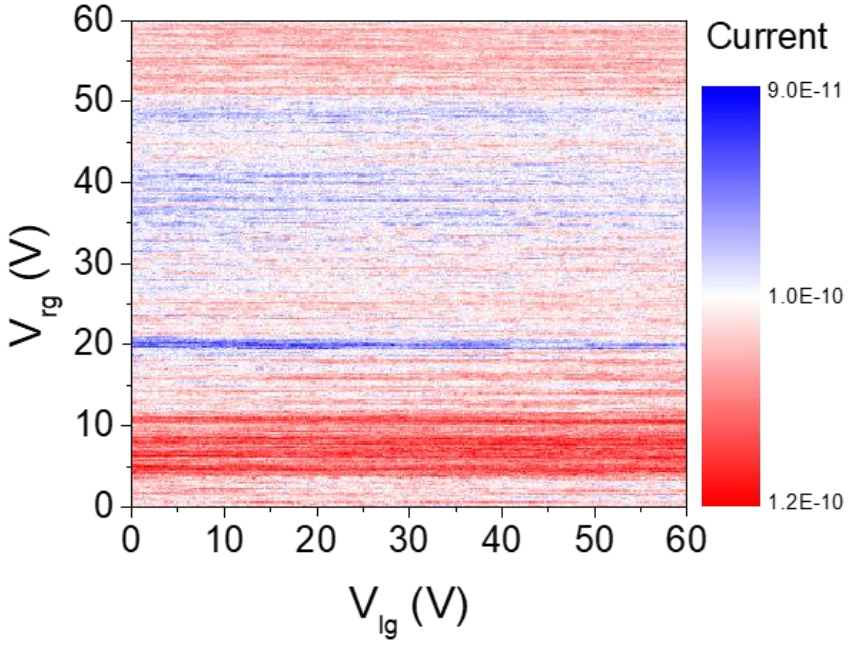

FIGURE 5.12: Stability diagram measured in Device B at room temperature with a bias voltage $V_{\mathrm{sd}} = 1\,\mathrm{V}$

The possible mechanism is the massive point defects. To pattern the device, the edges of GNR had been exposed to a large amount of helium ions. As a result, the GNR edges are heavily damaged, making the "true" conductive channel smaller and even further from the gate than what we see in the microscope.[10] In this case, we need to place the side gates to a position closer to the centre QD to realize the SET operation since the gate capacitance inversely proportional to the distance. In addition, changing the gate design is another choice. Possible candidates in this special case will be surrounding gate in carbon nanotube studies.

Another consideration is the utilization of the conductive changing property to creat the tunnel junction instead of patterning a dot island. Just before this work started, Tomizawa *et al*, used focused ion beam irradiation to control the tunnel junctions in multi-wall carbon nanotube.[11] Single QD Coulomb blockade is achieved by using this strategy. This report inspires our future experiments on HIBM and suspended graphene double QD fabrication.

5.4 Summary

In summary, we developed the fabrication process for suspended graphen double QDs system. Two large contacts on the GNR ends with five side electrodes on the GNR edges are attached to GNR. This design minimize the surface tension resulted GNR deformation, which provides a grounding for the success of HIBM patterning. After patterning, Ohmic I_{sd}-V_{sd} can be found in QDs with diameters of 150 nm and tunnel junctions of 80 nm. Smaller device (Device A) can be patterned, however it transforms to insulator because of the small device geometry and the point defects.

The last issue, the gate tunability for device operation is poor in this prototype devices, possibly due to the HIBM introduced point caused smaller effective channel width. In the future, we will continue to work on this issue, try to find a suitable geometry dimension for the device, or change the side gate to other form, *e.g.*, bottom or a cylinder-like surrounding gates.

Bibliography

[1] Zippilli, S.; Morigi, G.; Bachtold, A. Cooling Carbon Nanotubes to the Phononic Ground State with a Constant Electron Current. *Phys. Rev. Lett.* **2009** *102*, 096804.

[2] Häkkinen, P.; Isacsson, A.; Savin, A.; Sulkko, J.; Hakonen, P. Charge Sensitivity Enhancement Via Mechanical Oscillation in Suspended Carbon Nanotube Devices. *Nano Lett.* **2015** *15*, 1667-1672.

[3] Chiu, H.Y.; Hung, P.; Postma, H.W.C.; Bockrath, M. Atomic-Scale Mass Sensing Using Carbon Nanotube Resonators. *Nano Lett.* **2008** *8*, 4342-4346.

[4] Luo, G.; Zhang, Z.Z.; Deng, G.W.; Li, H.O.; Cao, G.; Xiao, M.; Guo, G.C.; Guo, G.P. Coupling Graphene Nanomechanical Motion to a Single-Electron Transistor. *Nanoscale* **2017** *9*, 5608-5614.

[5] Abbas, A. N.; Liu, G.; Liu, B.; Zhang, L.; Liu, H.; Ohlberg, D.; Wu, W.; Zhou, C. Patterning, Characterization, and Chemical Sensing Applications of Graphene Nanoribbon Arrays Down to 5 nm Using Helium Ion Beam Lithography. *ACS nano* **2014** *8*, 1538-1546.

[6] Naitou, Y.; Iijima, T.; Ogawa, S. Direct Nano-Patterning of Graphene with Helium Ion Beams. *Appl. Phys. Lett.* **2015** *106*, 033103.

[7] Naitou, Y.; Ogawa, S. Anderson Localization of Graphene by Helium Ion Irradiation. *Appl. Phys. Lett.* **2016** *108*, 171605.

[8] Naitou, Y.; Ogawa, S. Conductivity Change of Defective Graphenen by Helium Ion Beams. *AIP Advances* **2017,** *7*, 045203

[9] Nakaharai, S.; Iijima, T.; Ogawa, S.; Suzuki, S.; Li, S.L.; Tsukagoshi, K.; Sato, S.; Yokoyama, N. Conduction Tuning of Graphene Based on Defect-Induced Localization. *ACS nano* **2013** *7*, 5694-5700.

[10] Schmidt, M.E.; Iwasaki, T.; Muruganathan, M.; Haque, M., Van Ngoc, H.; Ogawa, S.; Mizuta, H. Structurally Controlled Large-Area 10 nm Pitch Graphene Nanomesh by Focused Helium Ion Beam Milling. *ACS Appl. Mater. Interfaces* **2018** *10*, 10362-10368.

[11] Tomizawa, H.; Suzuki, K.; Yamaguchi, T.; Akita, S.; Ishibashi, K. Control of Tunnel Barriers in Multi-Wall Carbon Nanotubes using Focused Ion Beam Irradiation. *Nanotechnology* **2018** *28* p.165302.

Chapter 6

Summary

During the years of my master studies, I have fabricated graphene nanoribon FET and SETs. We observed single QD-like SET features in small GNRs, which is stemmed from edge roughness and inhomogeneity doping in GNR resulted disordered transport gap. With our current technology, both effects are hardly to completely overcome. Under this circumstance, I come up with an idea to realize single QD-like band structure via transport gap engineering, *i.e.*, controllable HSQ doping.

For a long time, HSQ has been only considered as a fine resolution e-beam resist. Until Banner and Murali[30] demonstrated the utilization of HSQ for graphene doping. In my phD studies, I developed this method for different purpose. The basic concept is controllably cleaving the Si-H and Si-O bonds. Due the a mismatch of the bond strength, the Si-H are easily break when the sample is heated or exposed to high power energy irradiation such as plasma and electron beam. Subsequently, hydrogen are generated to graphene resulting in n-type doping. On the other hand, Si-O bonds are hard to break unless one increased the power of energy source or the Si-H bonds are completely broken. The generated oxygen will induce p-type doping to graphene. Due to this unique interaction between HSQ and graphene, doping control in HSQ capped GNR can be expected during and after device fabrication.

The first strategy is current annealing. Applying a massive current passing through the GNR channel will generate Joule heat that readily cleaves the chemical bonds of the HSQ molecule. Using this method we could control the overall doping level in GNR. For demonstration, experiments on HSQ capped monolayer FET

and bilayer GNR is performed. In monolayer graphene, we demonstrated the feasibility of doping level control using current annealing. In the monolayer GNR, we successfully tuned the Fermi energy to its sub-valence band region, where the interband scattering is observed. In addition, at this region, electrically tunable localization states are also studied experimentally. However, the spatial doping can not be properly controlled over using current annealing.

The secondary is using e-beam lithography system to controllably cleave the chemical bonds of HSQ molecule by changing the e-beam irradiation dose. Thanks to the fine spatial resolution of EBL technology, we could precisely control the doping level and area. Using this method, controllable doping with nanometer scale spatial resolution is demonstrated and single QD-like SET properties is observed. For the aspect of manufacture, we provide a geometry design rule to observe single QD-like properties. Unfortunately, due to the system limit, we fall to fabricate a local gate to tune the chemical potential of QD in GNR. But the doping control method we have developed offers us a new option for future graphene, and other two-dimensional nano-device fabrication.

Apart from doping, I have also worked on the development of suspended graphene QD system. Going through the previous experience, we considered using helium ion beam technology to pattern suspended GNR channel. We have designed structure and the process to avoid graphene edge rolling up, which allows the succeed in complex suspended GNR patterning. The remaining work is fining the gate tunablility. In the future, this could be expected by changing the gate structure, or the distance between gate and GNR channel.

Acknowledgements

For completing this work, a lot of people kindly helped me whenever I need. Here, I would like to express my sincere gratitude for people involved with this project.

First of all, I would like to express my special thanks of gratitude to my supervisor Prof. Hiroshi Mizuta for offering me this opportunity to study at Mizuta Laboratory.

Especially, I am grateful to Prof. Jian Sun, Senior lecture Manoharan Muruganathan for teaching and taking care of me. In addition, sincerely thank Dr. Koji Ishibashi, Dr. Russell Stewart Deacon, Dr. Rui Wang and Ms. Yuriko Asano in RIKEN for accepting my internship application. I have gained a lot of experience through from you. Your warm encouragements inspired me once, and will certainly inspire me in the future.

I would like to thank Dr. Marek E. Schmidt, Dr. Ahmed Hammam, Dr. Nikolaos Matthaiakakis, Dr. Kulothungan Jothiramalingam and Dr. Shunei Suzuki for the experiment training. When I was in trouble, they always give me their hands and share their precious experiences. Without their help, I could not even start my study. I hope you are doping a good job. Meanwhile, thank my laboratory colleges, Dr. Kareekunnan Afsal, Mr. Günter Ellrott, Miss. Haque Mayeesha Masrura, Mr. Gabriel Agbonlahor for the sharing the happiness with me.

I am grateful to Takahiro Yonezawa, Teruhisa Kanzaki, Fumihiro Seto and Daiki Kato, my colleges. It is very nice to work with them. For Kanzai kun and Kato kun, who left JAIST, I would like to give my best wishes. Wish them had a nice life after their graduation.

I would like to thank Dr. Yukinori Morita, Dr. Shinichi. Ogawa, in AIST for allowing me to perform experiments in their laboratory. I acknowledge Mr. Tomohiko. Iijima for the operation of AIST SCR helium ion microscope for the helium ion beam milling.

Finally, I would like to thank my family for the encouragement and supporting me study abroad. Also thanks to the one who I will spend my life with in the future. So far you haven't show up so I could focus on my interests.

List of Publications

Journal Publications

Wang, Z.; Yuan, Y.; Liu, X.; Sun, J.; Muruganathan, M.; Mizuta, H. Quantum Dot Formation in Controllably Doped Graphene Nanoribbon. *ACS nano* **2019**, *13*, 7502-7507

Wang, Z.; Sun, J.; Muruganathan, M.; Mizuta, H. Electrically Tunable Localized States in Sub-Band of Bilayer Graphene Nanoribbon. *Appl. Phys. Lett.* **2018,** *113,* 133101.

Iwasaki, T.; Wang, Z.; Muruganathan, M.; Mizuta, H. Formation of Quantum Dot in Graphene Single Nanoconstriction. *Appl. Phys. Exp.* **2019**, *12*, 025004

International Conferences‘

Tan, Z.; Wang, Z.; Schaal, S.; Agbonlahor, G.; Iwasaki, T.; Muruganathan, M.; Mizuta, H.; Chong, M. H. *2018 International Conference on Solid State Devices and Materials (SSDM 2018)*, PS-8-06, The university of Tokyo, Tokyo, Japan, September 2018.

Wang, Z.; Iwasaki, T.; Muruganathan, M.; Mizuta, H. Observation of Single Carrier Transport Behavior in Graphene Nano Constrictions. *43rd International Conference on Micro and Nanoengineering (MNE 2017)*, Braga, Portugal, 18-22 September, 2017

Iwasaki, T.; Wang, Z.; Muruganathan, M.; Mizuta, H. Physisorption doping induced multiple dots behavior in graphene nanoconstrictions. *Silicon Nanoelectronics Workshop*, Kyoto, Japan, 4-5 June 2017.

Domestic Conferences

Wang, Z.; Muruganathan, M.; Schmidt, M. E.; Morita, Y.; Ogawa, S., Mizuta. H. Enhanced Mechanical Stability for Suspended Graphene Devices Fabrication. *The 80th JSAP Autumn Meeting*, 21a-PB1-54, Hokkaido University Sapporo Campus, Sapporo, September 2019

Wang, Z.; Muruganathan, M.; Schmidt, M. E.; Morita, Y.; Ogawa, S., Mizuta. H. Helium Ion Beam Milling Patterned Suspended Graphene Double Quantum Dots. *The 80th JSAP Autumn Meeting*, 19p-E302-5, Hokkaido University Sapporo Campus, Sapporo, September 2019

Quantum Dot Formation in Locally Doped Graphene Nano Ribbons. *The 66th JSAP Spring Meeting*, 10a-W521-10, Tokyo Institute of Technology Ookayama Campus, Tokyo, March 2019.

Wang, Z.; Iwasaki, T.; Muruganathan, M.; Mizuta. Study of a Single Constriction in Graphene Nanoribbons for Single Carrier Transistor Operation. *The 64th JSAP Spring Meeting*, 15-aB6-2 Pacifico, Yokohama, March 2017.